LA--11767-T

DE90 011508

LA-11767-T
Thesis

UC-410
Issued: May 1990

$(\pi^{\pm}, \pi^{\pm\prime} N)$ Reactions on ^{12}C and ^{208}Pb Near the Giant Resonance Region

*Sung Hoon Yoo**

**Guest Scientist at Los Alamos. Physics Department, University of Texas, Austin, TX 78712.*

Los Alamos National Laboratory
Los Alamos, New Mexico 87545

Acknowledgements

I would like to express my formost thanks to my adviser, Professor C. Fred Moore for his brilliant guidance , and Dr. Chris Morris for showing me the conditions for being an outstanding experimental-physicist. I cannot overlook the tremendous input made by the Professor Dieter Dehnhard and Dr. Susan Seestrom in publishing two papers and shaping my dissertation. Special gratitudes go to Dr. Shaul Mordechai and my friends, Dr. Mark Jones, Allen Williams, Dr. David Oakley, Dr. Steve Sterbenz, and Dr. Ali Fazely for making this experiment possible. Mrs. Ruth Gibson and Ms. Yi-fen Yen are second to none to receive my personal appreciation. The MP10 staffs, Dr. Tanaka, Dr. Mcgill, Dr. Boudrie, Dr. Greene, Mr. Carpelli, and Dr. McClelland were so supportive in providing me what I needed in writing this dissertation. I also thank Dr. Chant and Dr. Roos for sending me the code THREEDEE, and Dr. Silbar for his helphul discussion.

$(\pi^{\pm}, \pi^{\pm\prime}\mathrm{N})$ REACTIONS ON ^{12}C AND ^{208}Pb NEAR THE GIANT RESONANCE REGION

by

Sung Hoon Yoo

ABSTRACT

Angular distributions for the $^{12}C(\pi^{\pm}, \pi^{\pm\prime}\mathrm{p})$ and $^{208}Pb(\pi^{\pm}, \pi^{\pm\prime}\mathrm{p}$ or n) reactions near the giant resonance region have been measured at $T_{\pi} = 180$ MeV, and found different between π^{+} and π^{-} data. This observation is interpreted as evidence for different excitation mechanisms dominationg the π^{-}-nucleus and π^{+}-nucleus interactions in the giant resonance region of these targets. A comparison with the single-nucleon knock-out distorted-wave impulse approximation calculations shows, even though these calculations underestimate $(\pi^{\pm}, \pi^{\pm\prime}\mathrm{N})$ data for both targets, the dominance of diect process (due to quasi-free scattering) for $(\pi^{+}, \pi^{+\prime}\mathrm{p})$ or $(\pi^{-}, \pi^{-\prime}\mathrm{n})$ in contrast to $(\pi^{-}, \pi^{-\prime}\mathrm{p})$ or $(\pi^{+}, \pi^{+\prime}\mathrm{n})$. In the $(\pi^{+}, \pi^{+\prime}\mathrm{p})$ [or $(\pi^{-}, \pi^{-\prime}\mathrm{n})$] reaction proton-proton hole states [neutron-neutron hole states] are excited directly and appear to have a large probability for direct decay with escape width, whereas in $(\pi^{-}, \pi^{-\prime}\mathrm{p})$ [or $(\pi^{+}, \pi^{+\prime}\mathrm{n})$] the preferentially excited neutron-neutron hole doorway states [proton-proton hole doorway states] couple

to resonance states and decay with spreading width. This interpretation led us to suggest that the ratio of cross-sections for inelastic scattering to the giant resonance region should be written in terms of an incoherent sum of cross-sections to neutron and proton doorway states. In a heavy nucleus such as ^{208}Pb, neutron and proton doorway states contribute incoherently because the different decay processes do not populate the same final states of the residual nucleus. A reanalysis of the previous ^{208}Pb(π,π') data extracted for the giant quadrupole resonance in ^{208}Pb, assuming an incoherent addition of cross-sections to neutron and proton doorway states gives $R = M_n/M_p = 2.1$ compared to 3.8 from the previous analysis using the coherent addition. This new result is in better agreement with the hydrodynamical model prediction R=1.54.

Contents

List of Figures

List of Tables

Chapter 1. Introduction

This dissertation describes measurement made of the reaction $(\pi^{\pm}, \pi^{\pm\prime}\mathrm{N})$ on ^{12}C and ^{208}Pb. In this chapter, firstly, the physical properties of the pion and the well known phenomenon observed in pion-nucleon scattering at incident pion energies near 180 MeV will be introduced. Then, since the data show features of both collective nuclear phenomena and nuclear independent particle motion, a brief discussion of these models of nuclear structure will be presented. Models that describe the nuclear reaction dynamics will be also discussed in the subsequent section. These discussions will lay the groundwork necessary for a detailed understanding of the experimental results presented later in this thesis. Finally, the motivation of this $(\pi^{\pm}, \pi^{\pm\prime}\mathrm{N})$ coincidence experiment is discussed.

1.1 The Pion

The pion is the lightest meson that can play a role of the mediator in the nucleon–nucleon interaction. Because of its small mass, the pion is the longest-range carrier of the nuclear force [Ei-80]. With the isospin T = 1, the pion has three charge states, π^+, π^0 and π^-. The intrinsic spin and parity of each type of pion is same, $J^{\pi} = 0^-$. Thus, the pion is a boson, a pseudoscalar and isovector particle with no magnetic moment. The mass of the charged pions (which are anti-particles of each other) is 139.6 MeV and that of the neutral pion (which is its own anti-particle i.e., self-conjugate particle) is 135.0 MeV. The life time of the charged pions is about 26ns in its rest frame, with the dominant decay mode being, $\pi^{\pm} \rightarrow \mu^{\pm} + \nu_{\mu}$ (~100%); the life time of the π^0 is about 0.89×10^{-16}sec

with $\pi^0 \rightarrow 2\gamma$ (98.8%) being the primary decay. The pion has a radius of about 0.8fm [Lo-70]. Using the quark notation, the quark composition of each pion can be expressed as

$$\begin{aligned} \pi^+ &= \bar{d}u \\ \pi^- &= \bar{u}d \\ \pi^0 &= \frac{\bar{u}u - \bar{d}d}{\sqrt{2}} \end{aligned} \tag{1}$$

where u and d stand for (isotopic spin) up and down quarks with the charge of $+\frac{2}{3}$e and $-\frac{1}{3}$e, respectively.

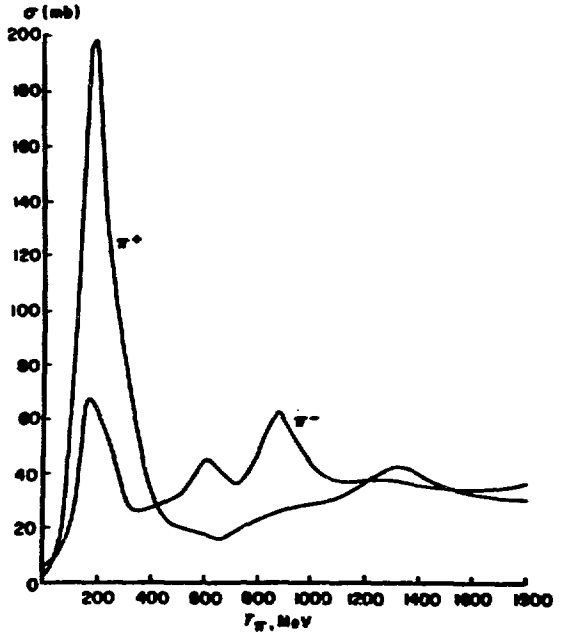

Fig. 1–1:Total cross section for π^+ and π^- scattering from protons from 0- to 1800-MeV pion kinetic energy [Pr-75].

Figure 1–1 shows the cross-sections for free π–nucleon elastic scattering for incident pion kinetic energies from 0 to 1.8 GeV. A large resonance can clearly be observed at an incident pion kinetic energy of about 180 MeV. The resonance appears at a total energy of 1232 MeV in the center of mass (CM) system of the π–nucleon with a width of approximately 110 MeV. The quantum numbers associated with the resonance are assigned as $T = \frac{3}{2}$ and $J = \frac{3}{2}$, and it is often called the $\Delta_{3,3}$ (in the notation $\Delta_{2J,2T}$) resonance. Considering the isospin of nucleon ($T = 1/2$) and that of pion ($T=1$), we expect the isospin of the Δ either $T = \frac{1}{2}$ or $\frac{3}{2}$. However, the $\pi^+ + p$ system is purely $T = \frac{3}{2}$ and since the Δ is seen strongly in the $\pi^+ + p \rightarrow \pi^+ + p$ channel it must have $T = \frac{3}{2}$. The Gell-Mann–Nishijima formula [Se-77], $Q(\text{charge}) = T_3 + \frac{B+S}{2}$, predicts four charge states, Δ^{++}, Δ^{+}, Δ^{0} and Δ^{-}, since Δ has the baryon number $B = 1$ and strangeness $S = 0$ ($S = 0$ and $B = 1$ for nucleon; $S = 0$ and $B = 0$ for pion). The evidence of $J = \frac{3}{2}$ for the resonance can be seen in the formula for the unitary limit of cross-section for the scattering of unpolarized particles,

$$\sigma_{max} = \frac{\lambda^2}{\pi} \frac{2J+1}{(2J_\pi+1)(2J_N+1)} = \frac{\lambda^2}{\pi}\left(J+\frac{1}{2}\right) \qquad (2)$$

where λ is the de Broglie wavelength of the pion in the center of mass system, $J_\pi = 0$, and $J_N = \frac{1}{2}$. As seen in Fig. 1–1, the maximum experimental cross-section, σ_{max}, at $T_\pi = 180$ MeV is about 200 mb, and the calculated value $\left.\frac{\lambda^2}{\pi}\right|_{T_\pi=180MeV}$ is approximately 100 mb. Thus, Eq. (2) results in $J = \frac{3}{2}$. Futher evidence comes from the angular distribution, $\sigma(\theta_{CM})$, in π^+–p elastic scattering, which is proportional to $1 + 3\cos^2\theta_{CM}$ near the resonance peak. This proportionality

shows that the scattering occurs in a $J = \frac{3}{2}$ state [Se-77]. Phase shift analysis of the scattered partial waves of the π–N interaction further confirms the dominance of the p wave, i.e., $p_{3,3}$ (in the notation $p_{2T,2J}$) channel (see table 1-1). Hence, the Δ resonance has the quantum number of $T = 3/2$, $\ell = 1$, and $J = 3/2$. The assumption of parity conservation in the strong π–N interaction gives the resonance positive parity, i.e., $\left[J = \left(\frac{3}{2}\right)^{+}\right]$.

Table 1–1: Low Energy Pion-Nuceon Phase Shifts [Ei-80,Ro-65].

T_π(MeV)	S_{11}	S_{31}	P_{11}	P_{31}	P_{13}	P_{33}
20	4.4	−2.2	−0.43	−0.25	−0.10	1.45
58	6.8	−4.8	−1.5	−1.08	−0.46	8.0
120	8.9	−8.8	−2.2	−2.9	−1.17	32.4
170	10.0	−12.1	−0.32	−4.6	−1.74	72.4
220	11.1	−15.1	4.68	−6.5	−2.23	109.5
310	12.9	−21.8	22.7	−10.8	−2.84	136.8

A test of charge independence (or total isospin conservation) of the pion–nucleon force is provided by examining the four different charge states of π–N scattering. If we denote the each charge state of the $\Delta_{3,3}$ resonance by the total isospin and isospin projection $|T, T_3)$, then the Clebsh–Gordan method establishes the following relations:

$$
\begin{aligned}
\left|\frac{3}{2},\frac{3}{2}\right\rangle &= |\Delta^{++}\rangle &&= |\pi^+ p\rangle \\
\left|\frac{3}{2},\frac{1}{2}\right\rangle &= |\Delta^{+}\rangle &&= \sqrt{\frac{1}{3}}\,|\pi^+ n\rangle + \sqrt{\frac{2}{3}}\,|\pi^0 p\rangle \\
\left|\frac{3}{2},-\frac{1}{2}\right\rangle &= |\Delta^{0}\rangle &&= \sqrt{\frac{2}{3}}\,|\pi^0 n\rangle + \sqrt{\frac{1}{3}}\,|\pi^- p\rangle \\
\left|\frac{3}{2},-\frac{3}{2}\right\rangle &= |\Delta^{-}\rangle &&= |\pi^- n\rangle\,.
\end{aligned}
\tag{3}
$$

In terms of quark notation, the four charge states of the $\Delta_{3,3}$ resonance can be expressed as

$$
\begin{aligned}
\Delta^{++} &= uuu \\
\Delta^{+} &= duu \\
\Delta^{0} &= ddu \\
\Delta^{-} &= ddd.
\end{aligned}
\tag{4}
$$

Using the orthogonality of the wave functions in Eq. (3), we can obtain the following ratio of cross-sections near $T_\pi = 180$ MeV,

$$
\begin{aligned}
&\sigma(\pi^+ p \to \pi^+ p) : \sigma(\pi^+ n \to \pi^+ n) : \sigma(\pi^+ n \to \pi^0 p) \\
&= (<\pi^+ p|\Delta^{++}><\Delta^{++}|\pi^+ p>)^2 : (<\pi^+ n|\Delta^{+}><\Delta^{+}|\pi^+ n>)^2 \\
&\quad : (<\pi^+ n|\Delta^{+}><\Delta^{+}|\pi^0 p>)^2 \\
&= 1 : 1/9 : 2/9 \;=\; 9 : 1 : 2\,.
\end{aligned}
\tag{5}
$$

These relations have been confirmed by π–nucleon scattering experiments [Ba-68]. (See figure 1–1, showing 3:1 ratio of π^+ to π^-, which also includes the charge exchange reaction in π^- + p channel). These ratios indicate that $\pi^+(\pi^-)$ is more prone to interact with a proton (neutron) than a neutron (proton). The π–nucleus interaction is intimately related to π–nucleon interaction. If a fast reaction time is assumed, the π-nucleus interaction potential can be based on π-nucleon scattering amplitudes (the impulse approximation). Thus, the formation of a $\Delta_{3,3}$ resonance

is expected to be a very important phenomenon in π–nucleus scattering. If the impulse approximation holds, then the free π-nucleon scattering ratio 9:1 should be also observed in pion–nucleus inelastic scattering. A measurement of cross-sections [Se-81] from the reaction $^{13}C(\pi^{\pm},\pi^{\pm\prime})$ shows that for the transition from the ground state to the $\frac{9^+}{2}$ state at 9.5 MeV in ^{13}C, the ratios of $\sigma(\pi^-)$ to $\sigma(\pi^+)$ is exactly 9 to 1 within errors. This transition is expected to be dominated by a $p_{3/2}^{(-1)}$-$d_{5/2}$ neutron excitation in both simple schematic shell model and also in more sophiscated Millener-Kurath shell model [Mi-75] bases.

1.2 Nuclear Structure

The spectrum shown in the upper part of Fig. 1–2 is typically observed in inelastic scattering reactions with fundamental pobes such as (e,e′), (p,p′) and (π,π′). The spectrum exhibits an elastic peak (ground state), inelastic peaks (discrete bound states) and nuclear continuum. The differences between this spectrum and the one shown in the lower part of the figure for scattering from a nucleon provide rich information about the structures of the nucleus. For the study of such nuclear structure the shell model and the collective model are the two major models used [Sa-80].

In the nuclear shell model moves each nucleon independently, in first approximation, in individual orbits. This independence of motion could be explained by the weakness of the long-range nuclear force and the Paulie exclusion principle [Br-77]. However, the difference between the atomic and nuclear shell model is that the nuclear shell model has the strong spin-orbit interaction term, and treats protons and neutrons independently, and there is no heavy center of

force, i.e., each nucleon behaves under the influence of spherically fixed potential of a nucleus. With these assumptions, the shell model has been successful in explaining the magic numbers—the numbers of protons or neutrons that give nuclei very stable configurations—and the properties of many excited states in nuclei with a closed shell (spherical symmetry) plus one or few additional valence nucleons or holes (small deformation). Nevertheless, the assumptions of independence and sphericity are oversimplified. Inability to account for the magnitude of quadrupole moments of many deformed nuclei is one example of the failures of the shell model.

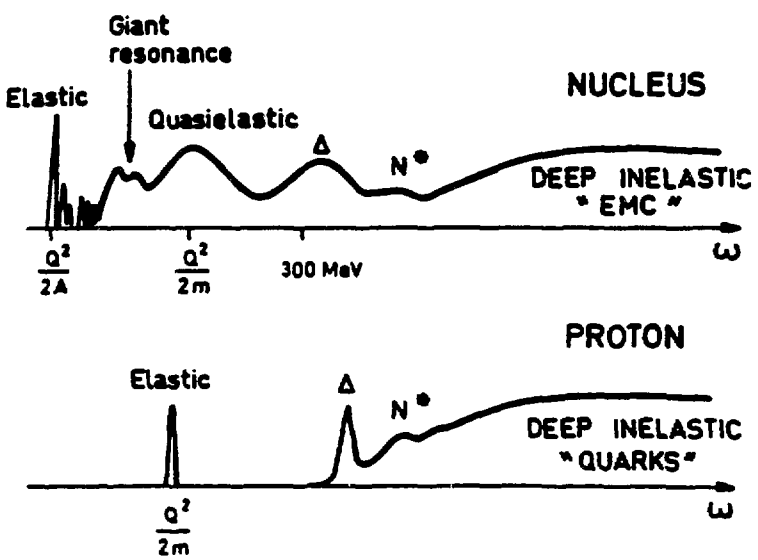

Fig. 1–2: Schematic shape of electron-nucleus (up) and electron-nucleon cross sections (bottom) as a function of the energy transfer ω [Fr-87].

The collective model views the nucleus as a liquid drop, that is, as a continuous distribution of nucleons. This allows that individual nucleons execute highly correlated motions. Thus, individuality is considered to be relatively unimportant. Evidences of such coherently collective motion of nucleons can be observed from (1) the surface vibrations (fig 1–3), (2) the surface rotations of deformed nuclei (figure 1–4), (3) the process of nuclear fission which occurs both naturally and in heavy ion scatterings (figure1–5), and (4) the giant resonance excitations (figure 1–6). The processes, (1), (2) and (3), occur near the surface of a nucleus. As a result, the vibrational and rotational transitions lie at low excitation energy. On the other hand, the giant resonances involve collective behavior of the bulk of the nuclear and consequently lie at higher excitation energy [Ei-75].

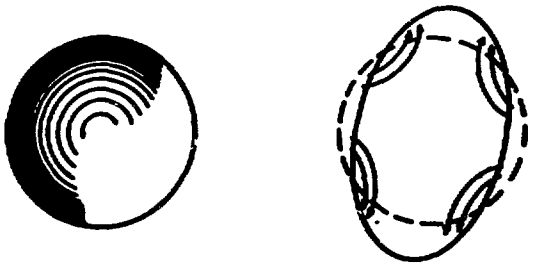

Fig. 1–3a: Schematic presentation of surfcace vibrations. The arrows indicate a possible flux (stream) lines of nucleons. The left-hand figure is for the spherical nucleus. The right-hand figure is for the distorted sphere [Ei-75].

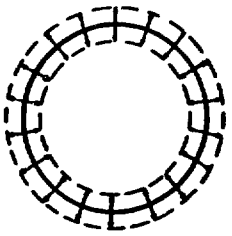

Fig. 1–3b: Schematic figure of compression mode. In contrast to the motion shown in Fig. 1–3a, the radial oscillations of the surface lead to density vibrations [Ei-75].

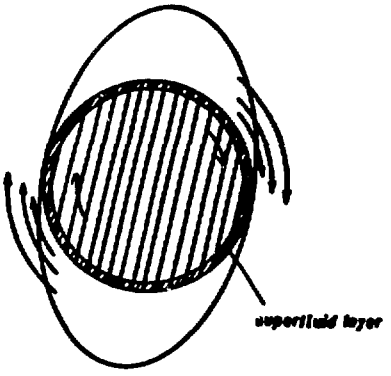

Fig. 1–4: Schematic presentation of the rotation of a deformed nucleus. The tidal wave is rotating around the nuclear core. The nuclear core also rotate with a smaller angular velocity. The existence of a superfluid layer can make the rotation of the nuclear core possible [Ei-75].

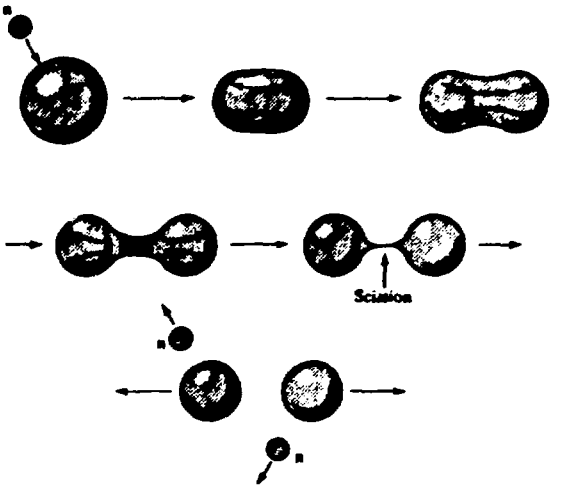

Fig. 1–5: Schematic figure of nuclear fission. The arrows indicate the flow of nucleons. The various possible stages of the separation of the nucleus into two pieces are indicated [Fr-74].

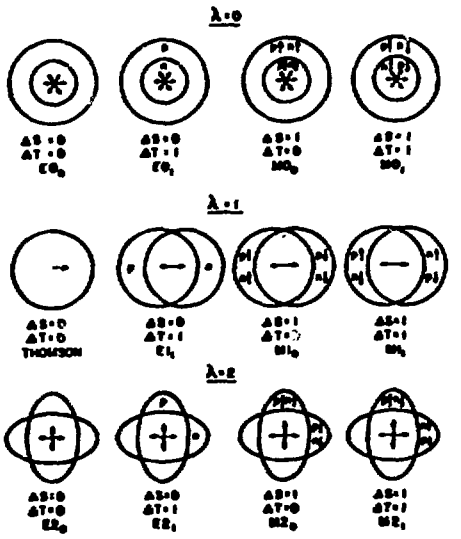

Fig. 1–6: The giant oscillations of a nucleus. Electric multipole transitions occur without spin flip, $\Delta S = 0$. Magnetic multipole transitions occur with spin flip, $\Delta S = 1$. $\Delta T = 0$ and $\Delta T = 1$ are for isoscalar and isovector transitions, respectively. λ is the orbital angular momentum transferred [Ha-79].

The two alternative pictures, the shell model and the collective model, are not totally independent. Actually both types of motion are always presented in a nucleus. Therefore, sepapration of the true character (individuality or collectivity) of a nuclear state remains as one of the important tasks to solve in the study of nuclear structures [Ei-75].

1.3 Nuclear Reaction Dynamics in Continuum

Two extreme reaction cases are usually considered in dealing with nuclear reaction dynamics. They are direct interaction, and compound nuclear formation/decay. Direct reaction can be understood as one step scattering (one-to-one reaction) since its reaction time ($\tau \ll 10^{-22}$ sec) is fast enough to avoid successive scatterings. (Note 10^{-22}sec is a typical nucleon orbital period with $\approx$ 20 MeV kinetic energy.) The speed indicates the direct dependence between entrance channel (initial state) and exit channel (final state) because of no intermediate state formation [Sa-80]. The types of direct interactions are:

(1) elastic and inelastic scattering

(2) transfer reactions such as stripping or pick-upreactions

(3) knock-out reactions (= quasi-free scattering = quasi-elastic scattering) [Sa-80].

For the description of the direct reactions the shell model is better suited and, especially, knock-out reaction can provide the validity of the model [Übb-79, Am-64]. Compound reactions can be understood by multistep scatterings. This process requires longer reaction time ($\tau \gg 10^{-22}$sec). Due to long interaction time, the

compound system loses its memory how it was formed except conservation of quantum numbers such as angular momentum [Sa-80]. Thus, there is independence between entrance channel and each decay channel. For the description of this compound reaction the liquid model is more suitable. Figure 1–7 illustrates the direct reaction and compound reaction mechanisms. The (π,π') reaction, which is direct, could result in either direct knock-out or formation of compound nucleus in the nuclear continuum. Thus, the emitted nucleon from the $(\pi^{\pm}, \pi^{\pm\prime}N)$ reaction are the results from both processes.

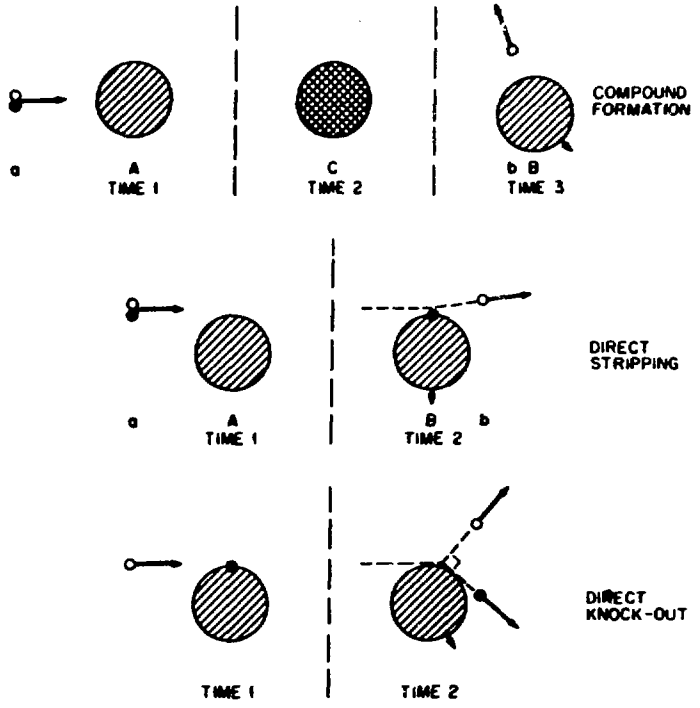

Fig. 1–7 Schematical illustration of the two limiting kinds of nuclear reaction, compound nucleus formation and decay, and direct reactions [Sa-80].

The nuclear continuum that is above nucleon break-up threshold comprises giant resonance and the quasi-elastic region as shown in figure 1–2. In the quasi-elastic region, quasi-elastic (quasi-free) scattering is considered as the dominant reaction. In the lower region of the continuum, however, transitions to the giant resonance states can proceed in competition with the quasi-elastic scattering process. Thus, a detailed understanding of the reaction mechanism is needed in order to unravel the structure of the continuum. For example, the extent to which isospin is a good quantum number for the giant resonances is of great importance in the study of nuclear structure. As an attempt to understand the reaction mechanisms in the nuclear continuum, the direct–semi direct (DSD) [Cl-65, Br-64, Lu-65] or the doorway-state (DS) [Fe-67] models are widely used.

In the DS model, as many authors described [Ok-82, Ey-84, Di-86], the incoming projectile first excites 1 particle-1 hole states. Then, these states can proceed to direct decay (escape width, $\Gamma^{\uparrow}$) by a particle emission, or successive inter-nucleon collisions leading to m particle–m hole states (m = 1,2,3, $\cdots$). At any stage, these m particle–m hole states can decay by emission of a particle. It is the spreading width, $\Gamma^{\downarrow}$ if m particle–m hole state is at an equilibrium of compound nuclear states which will later decay via thermal evaporation. Otherwise, it is the preequilibrium width, $\Gamma^{\uparrow\downarrow}$. In a light nuclei, ($A \leq 40$), decay is nearly 100% non-statistical, whereas in a heavy nuclei only about 15% is non-statistical [Ha-79]. Thus, in light nuclei, the giant resonance width can be expressed as

$$\Gamma_{tot} = \Gamma^{\uparrow} + \Gamma^{\uparrow\downarrow},$$

and, in heavy nuclei,

$$\Gamma_{tot} = \Gamma^{\uparrow} + \Gamma^{\uparrow\downarrow} + \Gamma^{\downarrow}.$$

Figure 1–8 represents schematically the DS and DSD models using the inverse capture process such as (N,γ) where N = p or n.

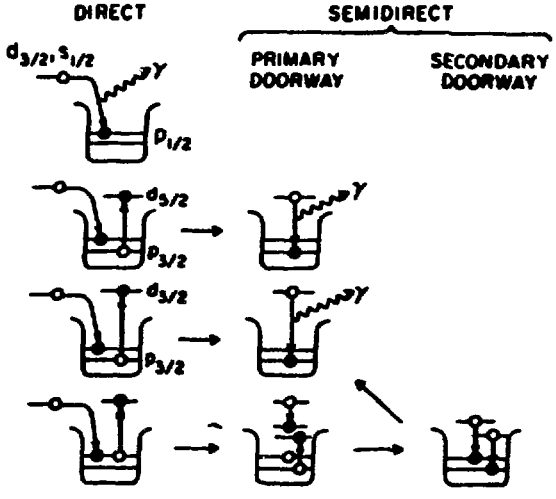

Fig. 1–8: Schematic Representation of the doorway-state model and its relation to the direct-semidirect model [Ha-79].

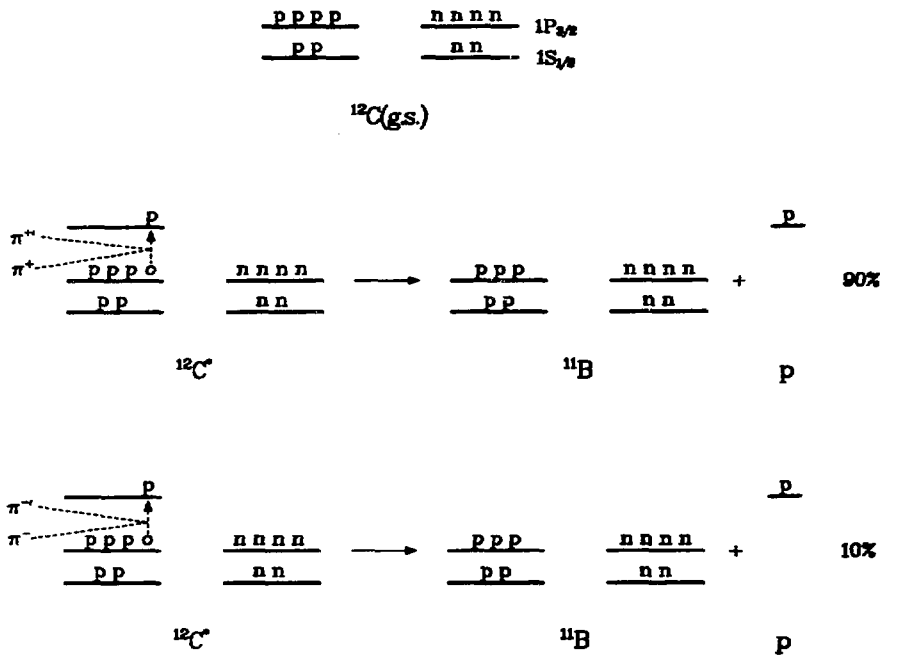

Fig. 1–9: Schematic picture of π-induced direct single-nucleon knock-out process analogous to Fig. 1–8. The diagram in the top portion represents the ground state of the ^{12}C.

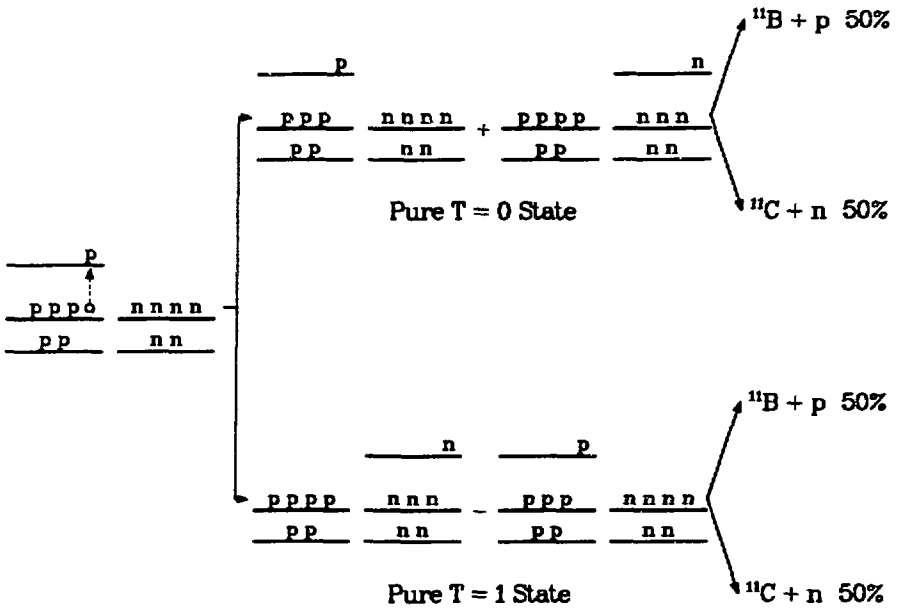

Fig. 1–10: Schematic representation of the doorway-state process induced by π. The incident pion excites the part of the giant resonance state (left), which leads to form either pure T = 0 or T = 1 state (middle). Then, it decays with the branch ratio by emitting a particle (right).

Similarly, we can also utilize the DS or DSD model to study the dynamic and microscopic picture of excitation and decay modes of the continuum induced by the $(\pi, \pi' N)$ reactions. As described earlier, in the lower part of the continuum (i.e., giant resonance region) where our interest lies, we expect the competition between the quasi-free scattering and the inelastic scattering that may excite the giant resonance of the target nucleus en route to the compound nucleus. In the quasi-free case, near $\Delta_{3,3}$ resonance, the incoming $\pi^+(\pi^-)$ excites proton (neutron) approximately nine times favorably than the incoming $\pi^-(\pi^+)$. Thus, as illustrated in figure 1–9, the branching ratio of 9:1 is expected between $\pi^+ + {}^{12}C \rightarrow \pi^{+\prime} + {}^{11}B + p$ and $\pi^- + {}^{12}C \rightarrow \pi^{-\prime} + {}^{11}B + p$. However, in the resonant inelastic scattering case, the ratio π^+/π^- is expected 1:1, if the isospin of the excited states is good, because the expectation of the doorway state (virtual state) of pure T = 0 or T = 1 will be independent of the charge state of the incoming pion (figure 1–10).

1.4 Coincidence Experiment using Pion as a Probe

As a method for the study of the GR and the quasi-elastic region of the nuclear continuum, inclusive inelastic experiments have been used extensively [Be-76]. One drawback of inclusive (single arm) experiments is the lack of a reliable theory to describe the background underlying the GR. Typically, arbitrary background shape (assuming no interference between the GR and the continuum) are subtracted from the experimental spectra [Ch-79]. Also, inclusive inelastic scattering studies of the GR do not reveal the decay process which contain much relavant information on the structure and dynamics of these collective modes of nuclear

excitation [Kn-88]. Experiments in which deexciting particles are detected in coincidence with inelastically scattered particles can provide a powerful tool in the investigation of the interplay between the decay mechanisms of the GR and those in the nuclear continuum.

Coincidence experiments, using pion as a probe, can provide an advantage over other projectiles in discerning the different decay modes of the GR—the direct decay via escape width ($\Gamma^{\uparrow}$) from the decay mode through spreading width ($\Gamma^{\downarrow}$)—by using the angular distributions of the decay particles, coupled with the selectivity of π^+'s (π^-'s) excitation of proton-proton hole doorway (neutron-neutron hole doorway) states. Recent data from the $(\pi^{\pm}, \pi^{\pm\prime}\mathrm{p})$ reactions on ^{4}He [Jo-89] and the data from this dissertation on ^{12}C target near the giant dipole resonance (GDR) of these nuclei have revealed that angular distribution of the recoiling proton are different for π^+ and π^-.

Another advantage of pion can be found in concerning energy weight sum rule (EWSR) values. To check the reliablity of each experiment, there has been a tendency to compare EWSR values obtained from hadronic probes with those from electromagnetic probes. Since hadronic interaction is made mostly near the nuclear surface while electromagnetic probes can penetrate the entire nuclear volume [Ko-86], comparison of hadronic and electromagnetic results seems to be irrelevant [Mo-88a]. Also the treatment of background is important for the comparison of EWSR values, especially between different probes where the background processes are expected to be different. For an example, (e,e'x) experiments [Bo-88] are claimed to be background-free, which assumes all the co-

incidence cross-sections are due to the GR excitation. However, this assumption of no contribution from continuum excitation is inconsistent with analysis of all inelastic scattering data in which large backgrounds are observed and subtracted [Se-86]. Thus, $\pi^{\pm}$-scattering is likely to provide a more reliable comparison of EWSR between $(\pi^{\pm},\pi^{\pm\prime})$ and $(\pi^{\pm},\pi^{\pm\prime}N)$ data, since both cases have similar background and distortion effects.

Coincidence experiments that have used pions as a probe can be largely divided into two groups: coincidences in quasi-elastic scattering ($E_x \geq 40$ MeV and backward angles) [Zi-79, Zi-81, Pi-81, Pi-82, Hu-87, Ky-84] and giant resonance scattering ($E_x \leq 40$ MeV and forward angles) [Jo-89]. In the first region, the dominance of the direct single-nucleon knock-out process is expected. Indeed, Chant et al. [Ch-82] have shown that single-nucleon knock-out calculations, carried out with the code THREEDEE [Ch-82b] are in good agreement with the measured $^{12}C(\pi^{+},\pi^{+\prime}p)^{11}B$(g. s) cross-sections of Ziock et al. [Zi-81] (Figure 1–11). These calculations are based on a factorized form of distorted-wave impulse approximation (DWIA), which includes distortion effects on the incident and scattered pion as well as the knocked-out proton. The processes that contribute to lower excitation energy region of the continuum, however, can be more complicated. It has been suggested that, in this GR region, direct decay (due to quasi-free-knock-out scattering) and semi-direct decay (due to resonant inelastic scattering to states of good isospin) compete with each other in a coherent way [Ũb-79].

The main motivation of this thesis experiment has its origin in the very complexity of the reaction process and the necessity for more information in the

giant resonance region. In this dissertation, the importance of knock-out scattering in the excitation region near the giant dipole resonance of ^{12}C (a self-conjugate nucleus) is evaluated by comparing data for the $^{12}C(\pi^{\pm}, \pi^{\pm\prime}p)^{11}B$ reactions with DWIA calculations performed with the code THREEDEE. Measurements of angular distributions of decay neutrons for the $(\pi^{\pm}, \pi^{\pm\prime}n)$ reactions near the giant resonance region of ^{208}Pb, which suggest a reanalysis of a DWIA analysis of the data obtained from previous inclusive experiment on ^{208}Pb, are also reported. The proton and neutron matrix element for the giant quadrupole resonance (GQR) are, then, extracted.

This dissertation is organized in five chapters. Experimental details are described in chapter 2; data reduction, calibration and results are discussed in chapter3; comparison of data with theoretical predictions is made in chapter 4; and a summary is presented in chapter 5.

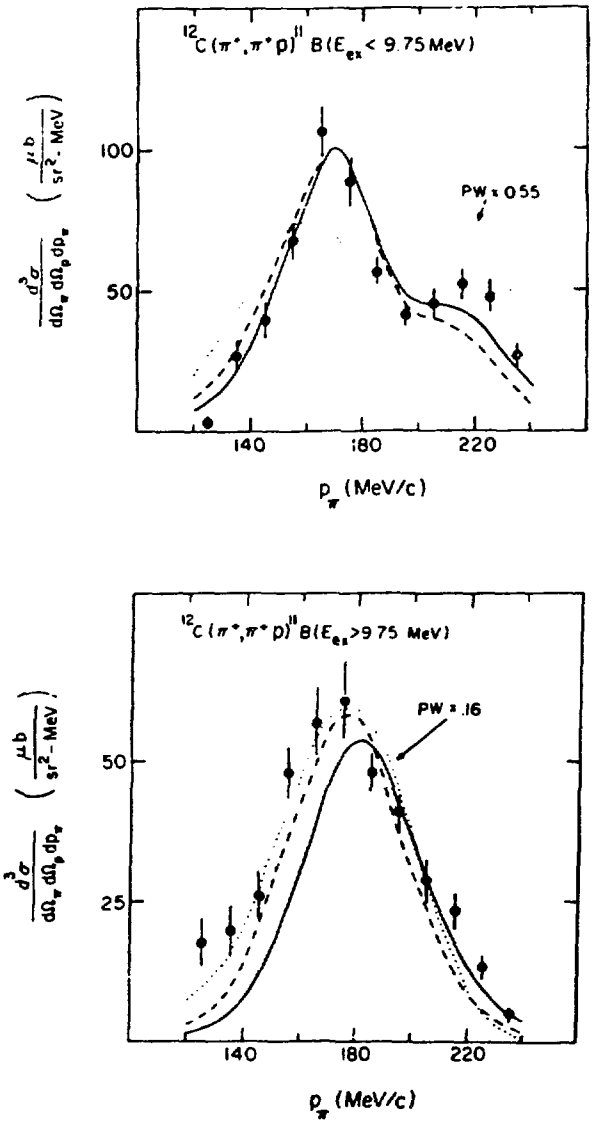

Fig. 1–11: Energy-sharing cross-sections for $1p_{3/2}$ knock-out T_π = 199 MeV, θ_π = −117.5°, and θ_p = 30.0°. The data are from Ziock et al. [Zi-81]. The dotted curve is a plane wave impulse approximation calculation using the final-energy prescription (FEP) for $[d\sigma/d\Omega]_{\pi^+-p}$. The full (dashed) curve is a DWIA calculation using the FEP (IEP: Initial-Energy Prescription) normalized by the spectroscopic factor 2.9 (3.6). [down] for $1s_{1/2}$ with the spectroscopic factor 1.8 (3.2) [Ch-82].

Chapter 2. Experiment

The $(\pi^{\pm}, \pi^{\pm\prime}N)$ reactions reported here were measured using the Energetic Pion Channel and Spectrometer (EPICS) at the Clinton P. Anderson Meson Physics Facility (LAMPF). An expatiation upon the experimental details involved in the coincidence experiment is presented in this chapter.

2.1 Accelerator and Beam lines

Figure 2–1 shows an overview of LAMPF featuring the half-mile-long proton linear accelerator (LINAC). The proton LINAC is divided into three major sections: the injectors, Alvarez-type drift tube LINAC, and the side-coupled resonant cavity linear accelerator [La-87]. The first stage of the acceleration begins at one of three injectors. Each injector has an ion source to produce the primary beam and a 750 KeV Cockcroft-Walton high voltage generator. This voltage generator pre-accelerates the primary beam produced by each ion source, the proton beam (H^+), negative hydrogen beam (H^-), and the polarized negative hydrogen beam (p^-), respectively. The next stage of the acceleration is made with an Alvarez-type drift tube LINAC, which is composed of four cylindrical vacuum tanks. Inside the tanks, drift-tubes of increasing length are suspended. An alternating electric field is kept at a radio frequency of 201.25 MHz in each tank. As shown in Fig. 2–2, both negative hydrogen and proton beams are accelerated simultaneously by alternating the electric field in such a way that the phase of H^- or p^- beam becomes opposite to that of H^+ beam during the rf cycle. After proceeding through 165 steps of this alternation, the beams reach an energy of

100 MeV. Then, they are accelerated to their final energy, 800 MeV, in the side-coupled-cavity LINAC. At its best condition which seldom occurs, the LAMPF proton LINAC produces a 800 MeV pulsed proton beam with an average beam current of 1 mA at a duty factor of 9 $\sim$ 10.5% and repetition rate of 120 Hz. The average primary beam current during this experiment was about 950 μA.

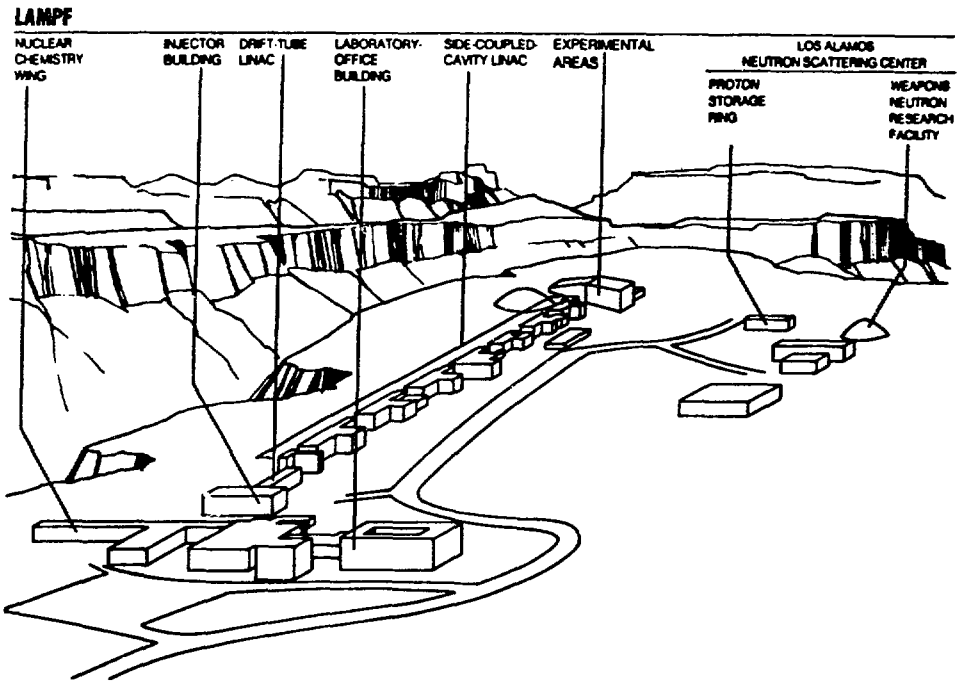

Fig. 2–1: An overview of LAMPF.

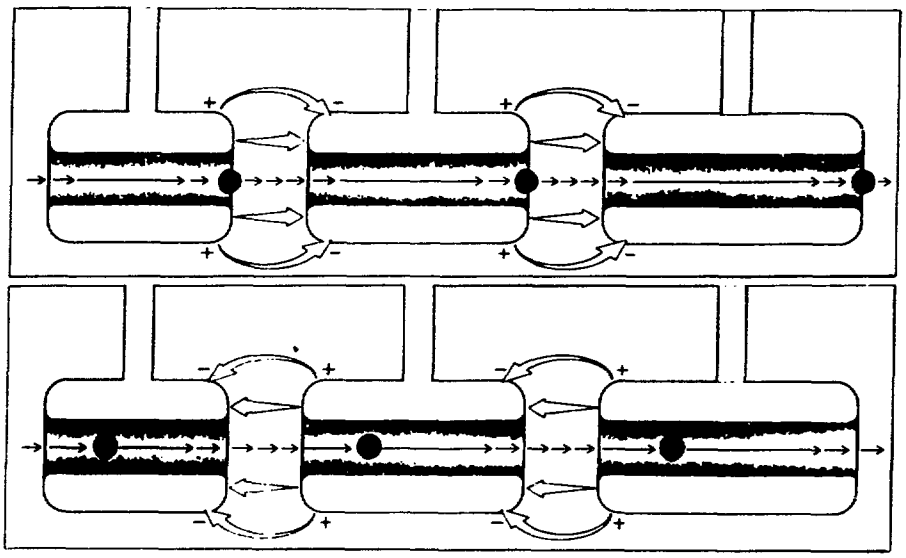

Fig. 2–2: (Top): The positively charged protons are in the gaps between drift tubes. They are propelled forward by the electric field during the first half of the cycle. (Bottom): In the second half of the cycle, the protons are inside the drift tubes and move forward due to the reversed electric field. The particles with positive charges and negative charges are accelerated simultaneously in such a way that the positive ones are in the gaps while the negative ones inside the drift tubes [La-87].

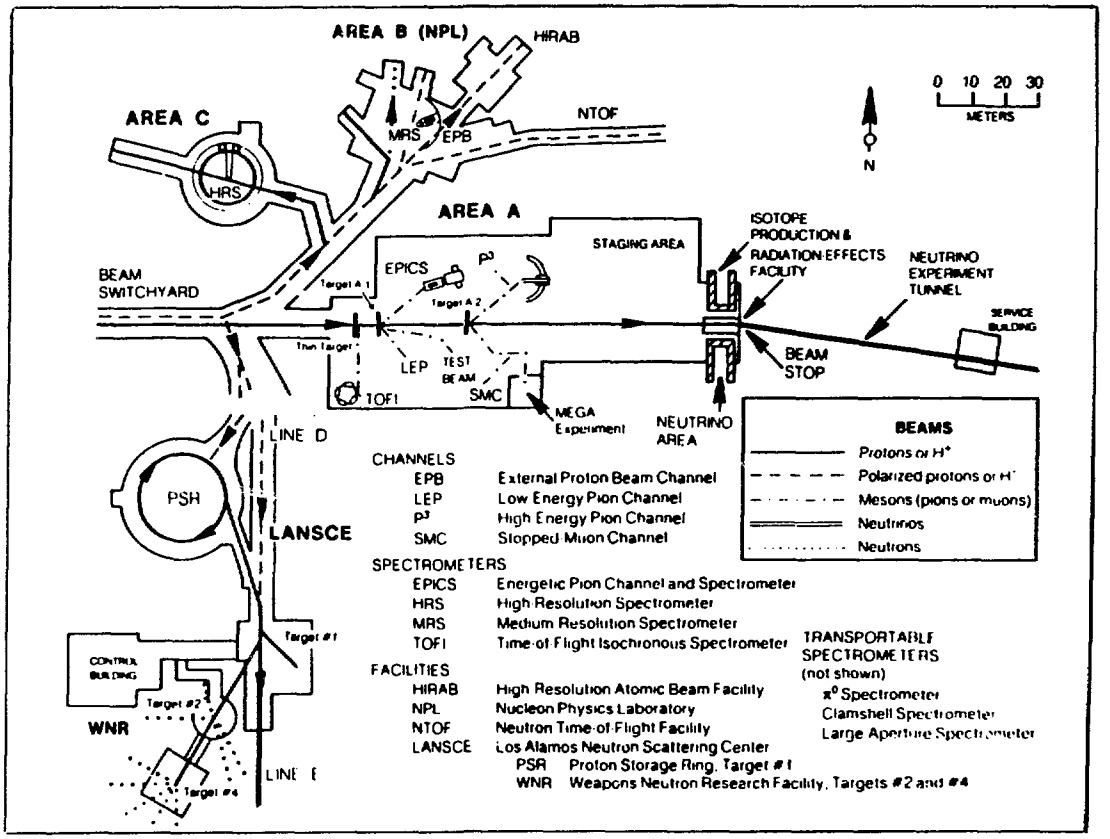

Fig. 2–3: Layout of the LAMPF experimental areas.

After the final acceleration, the H^+ and H^- beams arrive at the beam switchyard (Fig. 2–3). From there the H^- beam is sent to either the Los Alamos Neutron Scattering Center (LANCE/WNR), the experimental area B, or experimental area C, whereas the H^+ beam goes to beam area A. Upon the incidence of the primary H^+ beam on the A-1 or A-2 target, the secondary beams of the pion and other particles are produced and delivered to different channels in the beam area A. The A-1 secondary beam production target, the source of beam supply for the EPICS channel, is a graphite with areal density of 5 gr/cm^2, which rotates in the 800-MeV proton beam to abate the heat problem generated from the input power of the beam. The thermal characteristics and low density of carbon alleviate the cooling problem while its relatively low Z and low density mitigate the multiple scattering of the proton beam [Th-70].

2.2 Epics

The EPICS system consists of a high resolution channel that delivers the secondary beams on a target inside a scattering chamber, and a high resolution spectrometer that analyzes the momentum of the outgoing particles [Th-77]. An lateral view of the system is shown in Fig 2-4.

2.2.1 Channel

The 15.24-m-long EPICS channel, which views the A-1 target at 35° relative to the primary proton beam line, is schematically presented in Fig. 2–5. The EPICS channel is composed of four dipole magnets (BM01-04), three multipole trim

magnets (FM01-03), four sets of collimating jaws (FJ01-04), a proton degrader, and four nuclear-magnetic-resonance probes (NMR1-4).

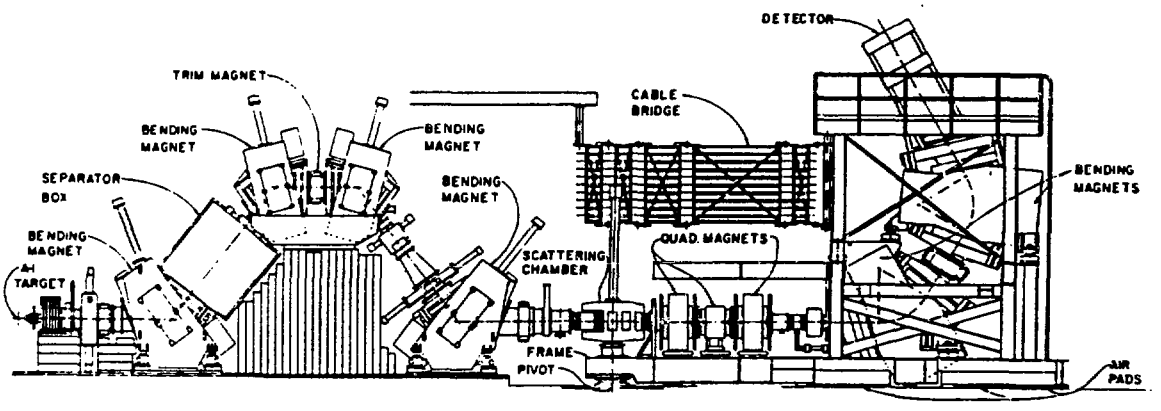

Fig. 2–4: An lateral view of the EPICS channel and spectrometer system. The channel is before the scattering chamber.

The dipole magnets (BM01-04) and the trim magnets (FM01-03) are the components that determine the beam optics of the channel. BM01-04 bend the particle from the A-1 target in a vertical plane, produce the dispersed beam, and select its momentum and charge (π^+ or π^-). In this dispersed beam, momentum of each particle is correlated with its vertical position ($\pm x$) [Th-70]. The advantage of the momentum-dispersed beam technique is that it provides more pion flux without a loss of resolution because of a much larger phase space than a monochromatic beam of the same solid angle [Se-81]. The dispersed π beam has a 2% (Full Width) momentum spread and a 2.0×10^{-4} (FWHM) final momentum resolution. Thus, a beam intensity 200 times larger than the equivalent monochromatic beam of the same resolution is obtained [Th-70]. Using this method, the EPICS-channel bending magnets, BM01-04, deliver a momentum-dispersed π^+ or π^- beam of $T_\pi \leq 300$ MeV on the scattering target with optical focusing of the point-to-point in the vertical plane and point-to-parallel in the horizontal plane, as seen in Fig. 2–6. The function of the focussing magnets (FM01-03) is to correct the effective field boundary of this dipole magnets through quadrupole, sextupole, and octupole fields [Se-85]. FM01-03 are set according to the predetermined optimized-values to provide the maximum energy resolution.

The collimating jaws (FJ01-04) are the components that control the flux and shape of the channel beams. An adjustable vertical jaw, FJ01, at the channel entrance determines the angular acceptance of the channel. FJ02-04 are three additional collimators with two movable pairs of jaws, one horizontal (y axis) and one vertical direction (x axis). The direction of the particle's trajectory is chosen

as z axis. Throughout the experiment FJ02 was not used. Among these jaws, FJ04 is the most important since it determines the vertical size (FJ04X) and horizontal divergence (FJ04Y) of the beam on the target. For this coincidence experiment, it was necessary to avoid the saturation of the detectors due to decay particles from high incident beam flux [Jo-89]. As shown in Table 2–1, when all four jaws are fully open, the incident π^- flux from the A-1 target is about a factor of 5 lower than the π^+ flux at all energies. Thus, the flux of the incoming pion was adjusted to be below the limit at which the counter was saturated. To maintain similar flux for both π^+ and π^- beams, FJ04Y was varied between π^+ and π^- runs. Since FJ04X affects the spectrometer acceptance, it was not varied to control the flux.

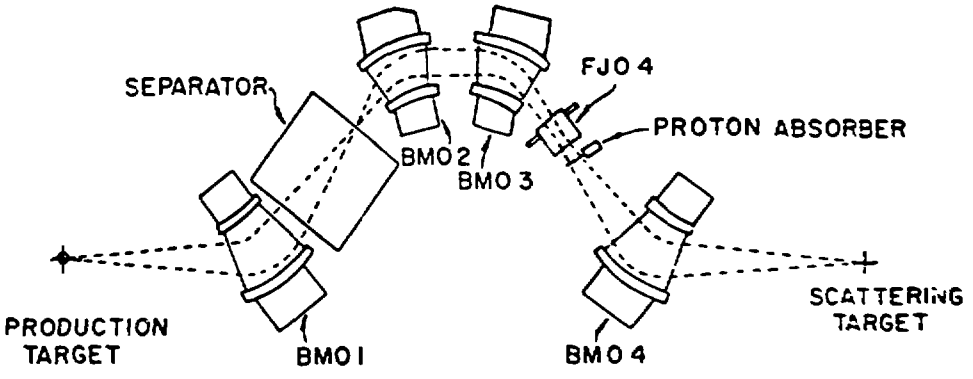

Fig. 2–5: Lateral view of the EPICS channel.

Table 2–1: Pion flux and beam composition in the EPICS channel [LA-80].

T_π (MeV)	Pion Flux[a] $(\times 10^7)\pi$/sec		Beam Content[b]			
	π^+	π^-	π	p	μ	e
100	6.7	1.8	100	~35	15	50
200	22.0	4.7	100	~400	5	8
300	26.0	4.5	100	~650	2	2

[a] Normalized to a primary proton beam average current of 1 mA.
[b] The relative beam contaminant numbers are normalized to the pion numbers.

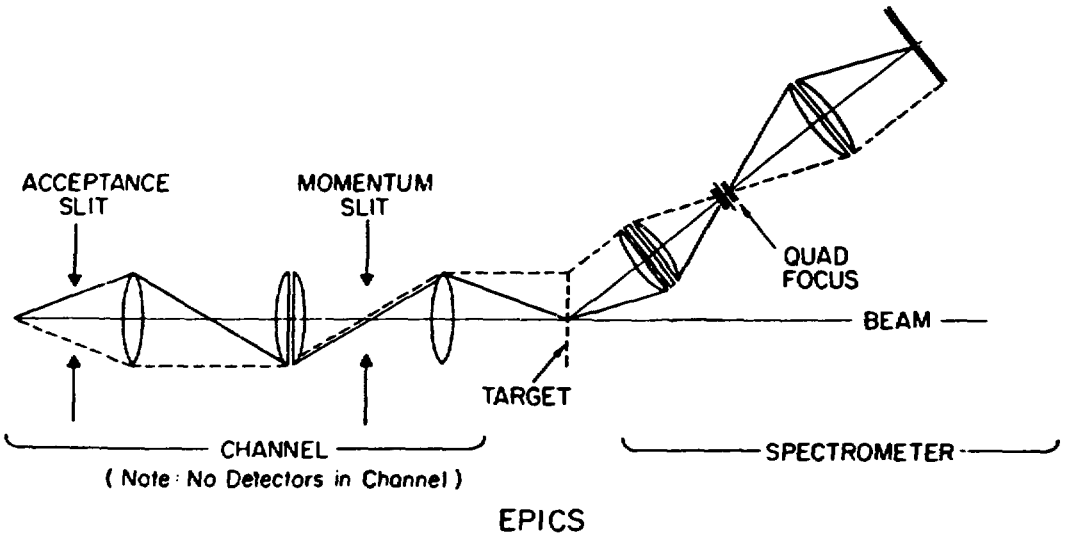

Fig. 2–6: Beam optics of the EPICS channel and spectrometer. Dashed line is for horizontal direction, and solid for vertical.

As Table 2–1 indicates, the proton contamination in the incoming π^+ beam is a serious problem. Protons were removed from the beam using a proton absorber (Fig. 2–5), a beryllium sheet, which takes advantage of the difference between the energy loss for the same momentum of pion and proton. Thus, the magnetic fields of BM01-03 were set so that the BM04 could select the desired pion momentum after the energy loss due to the absorber. Since the momentum of the proton is less than that of π after the absorber due to proton's larger energy loss, the protons are swept out of the pion beam. Finally, the remaining components of the channel, NMR1-4, are for reading magnetic field of each bending dipoles.

2.2.2 Spectrometer

A. Scattering Chamber and Target

A scattering chamber is coupled to the channel with a bellows and mounted on the frame for the EPICS spectrometer (Fig. 2–4). Inside the chamber the scattering target is positioned at the focal plane of the channel. For $\frac{\Delta P_c}{P_c} = 2\%$ (where P_c is the central momentum of the channel defined by the fields in the channel dipoles, P_π is the momentum of the incoming pion, and $\Delta P_c = P_\pi - P_c$), a beam spot size of 20 cm (vertical) × 8 cm (horizontal) is made on the target when the four collimators in the channel are fully open. In this experiment, the beam size of (± 1.5 cm) × (± 4 cm) was made at the target plane. For the $^{12}C(\pi^{\pm}, \pi^{\pm\prime}p)$ reaction a carbon foil of natural isotopic composition and of areal density 91 mg/cm^2 was used. The target for the $^{208}Pb(\pi^{\pm}, \pi^{\pm\prime}N)$ reaction was isotopically

enriched ^{208}Pb with an areal density of 150 mg/cm^2. For the normalization of the cross section, a CH_2 target with an areal density of 73 mg/cm^2 was used, and CH_2 with 70 mg/cm^2 was employed for the calibration of the decay particle detectors. The target angle for ^{12}C and ^{208}Pb was 60° with respect to the norm of the beam direction. The target angle for the calibration was set at −50° (refer to Chapter 3.). Around the target five bismuth-germanate phoswich detectors were installed at angles, −120°, −90°, −60°, 60° and 90° as shown in Fig. 2–7. The distance from the center of the target to each phoswich detectors was 24.13 cm. More details about the detectors will be presented in section 2.2.3. The scattering chamber is also maintained in the vacuum of $\approx 10^{-5}$ torr to reduce multiple scattering in the air for better resolution. For the current experiment a lead collimator was installed upstream of the scattering chamber in order to reduce the decay muon background in the coincidence counters. A thin (250 μm) stainless steel was additionally installed downstream from the scattering chamber to minimize the background flux of scattered particles.

B. Spectrometer

The EPICS spectrometer includes three quadrupole magnets (QM01–03) and two dipole magnets (BM05–06) in addition to various types of scattered particle detectors (Fig. 2–4 and –8). With a modified scattering chamber [Bu-86], this spectrometer can rotate to any angle for a full 180° scattering detection. In this experiment, using the regular chamber, the scattering angle was set at 20° for the $(\pi^{\pm}, \pi^{\pm\prime}\mathrm{N})$ reactions, 40° for normalization runs, and 70° for the decay particle detector calibration runs.

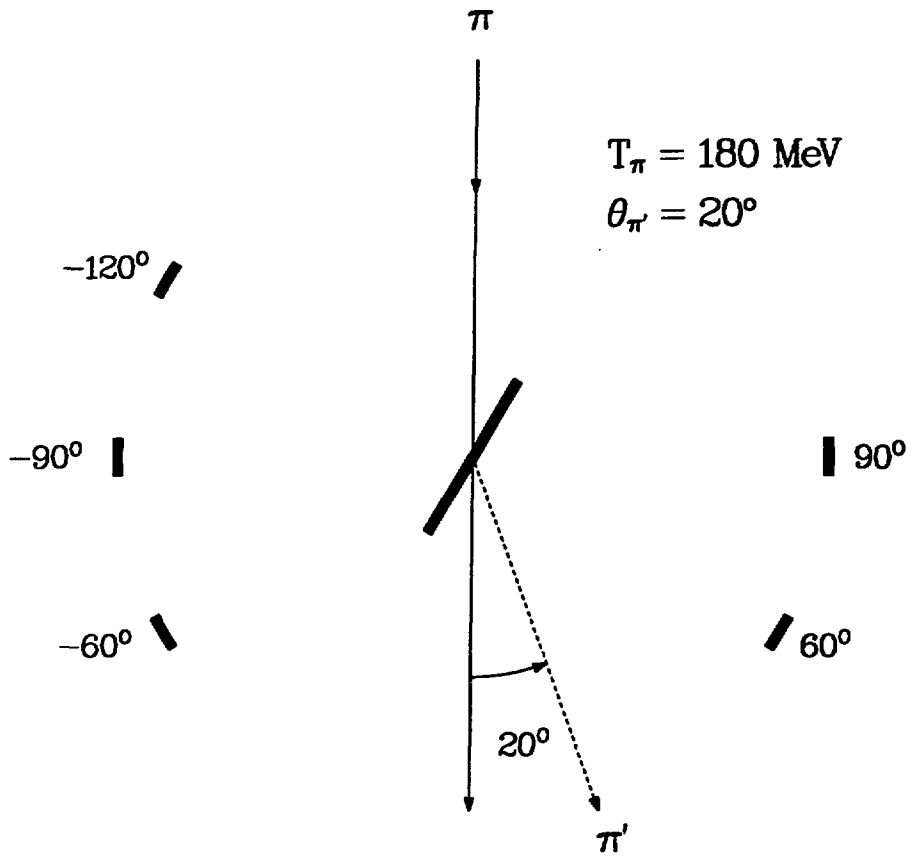

Fig. 2–7: Geometry of the incident beam, target angle, scattering angle, and decay/knocked-out particle detectors. Target angle is positive in counterclockwise direction.

The quadrupole triplet focuses the scattered particles to form an inverted image of the target with a magnification, M = -1, on the front focal plane before the BM05. The beam optics from the target to the front focus through this triplet is point-to-point in the vertical $(x - y)$ plane and parallel-to-point in the horizontal $(y - z)$ plane (Fig. 2–6). With the aid of multiwire chambers that determine the coordinate of each passing particle, the momentum of the incident and scattered particle can be measured accurately by tracing back the particle trajectories. Tracing from the front focus to the target determines the incident momentum, and tracing from the front focus to the rear focal plane of the two 120° bending dipole magnets determines the scattered momentum, in combination with the use of $\delta_{sp} = \frac{P_{\pi'} - P_s}{P_s}$, where P_s is the momentum corresponding to the central ray of the spectrometer and $P_{\pi'}$ is for the scattered pion. Thus, the EPICS channel and spectrometer have VHV configuration i.e., Vertical analysis/Horizontal scattering/Vertical analysis. The EPICS spectrometer has a momentum acceptance of ± 8%, and the two bending dipole magnets (BM05-06) yields a vertical dispersion of 4 cm/%. Shown in Table 2–2 is the specifications for the EPICS channel and spectrometer. The other parts of the spectrometer, the multiwire chambers and scintillators, will be discussed in next subsection, 2. 2. 3.

For the $^{12}C(\pi^{\pm}, \pi^{\pm\prime}p)$ experiment, two spectrometer fields were used in order to obtain a broad range of the momentum analysis from the giant resonance to higher excitation region, due to the limit in acceptance of the EPICS spectrometer. The 20 MeV excitation region above particle emission threshold

was set to be in the center of the focal plane for the first spectrometer energy bite and the 52 MeV region for the second bite. For the $^{208}Pb(\pi^{\pm}, \pi^{\pm\prime}N)$ reaction, the spectrometer field that makes the 15 MeV excitation energy appear at $\delta_{sp} =$ 2% was selected.

Table 2–2: EPICS channel and spectrometer specifications [La-80].

Channel		Spectrometer	
energy range	80 to 310 MeV	momentum range	100 to 750 MeV/c
$\Delta P/P$	2% FWHM		
solid angle	3.4 msr	solid angle	$\approx$ 10 msr
beam size (H×V)	8×20 cm^2	dispersion	4 cm / %
beam divergence (H)	< 10 mrad	$\Delta P/P$	$\pm$6%[a]
beam divergence (V)	100 mrad	flight path	$\approx$ 12.5 m[b]

[a] 90-cm focal plane, useful acceptance.
[b] target to rear focal plane.

2.2.3 Detectors

The particle detection system used for this experiment at EPICS can be divided into three groups: the decay/knocked-out particle, the scattered particle detection, and beam monitoring systems. A lateral view of this detection system is shown in figure 2–8.

A. Knocked-out/Decay Particle Detection System

Decay/knocked-out particles were detected in coincidence with the scattered pions (particles) using five plastic-BGO (bismuth-germanate, $Bi_4Ge_3O_{12}$) detectors mounted in the vacuum scattering chamber as already illustrated in Fig. 2–7.

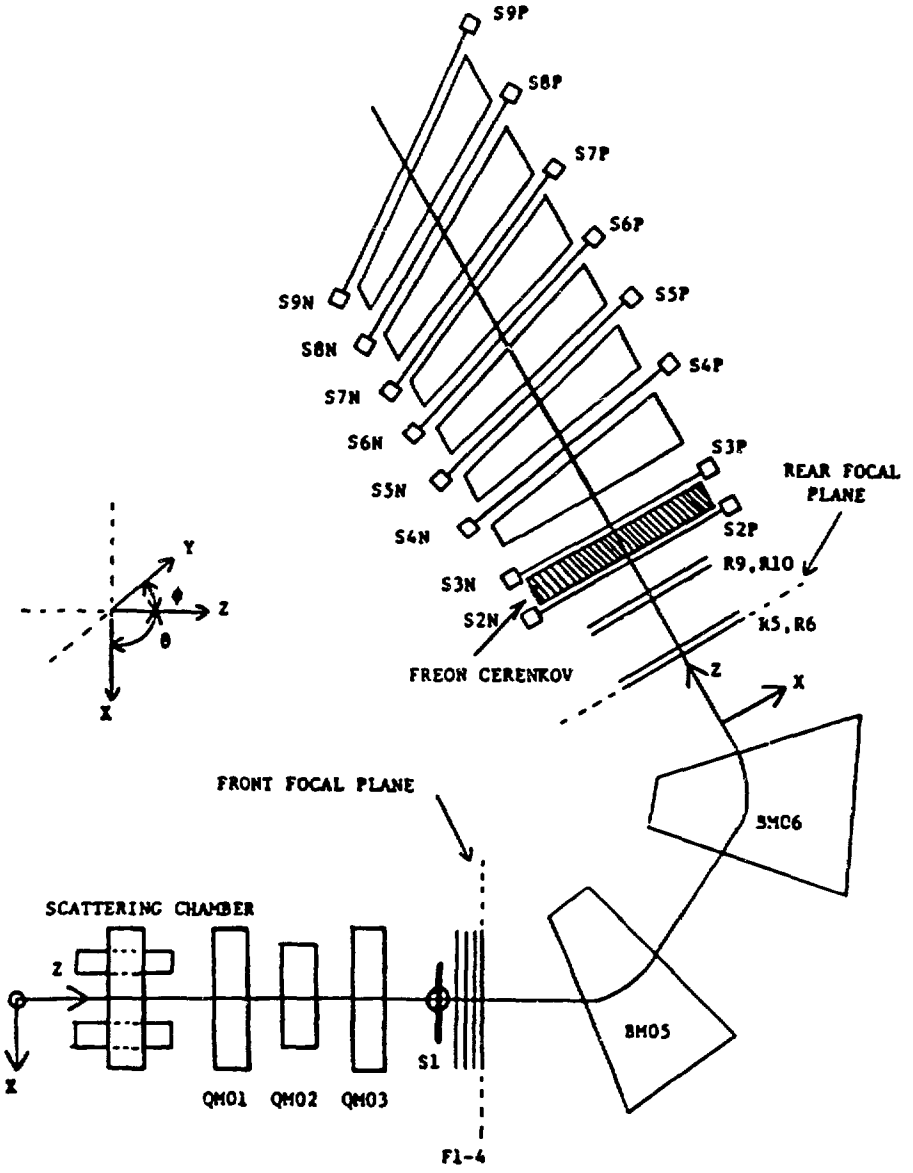

Fig. 2–8: Schematic presentation of the EPICS spectrometer detection system.

Each "phoswich" detector was made up of a light tight 0.013-mm thick aluminum cover, 3-mm thick CH_2 plastic scintillator disc, 5.08-cm long and 10.2-cm diameter BGO crystal and a 7.6-cm diameter phototube (Fig. 2–9). The detectors were placed a distance of 24.13 cm from the center of the target and subtended a solid angle of 139 msr. The energy loss in the detector entrance foil and in the scattering target limited the minimum detectable proton energy to 4 MeV at the center of the ^{12}C target.

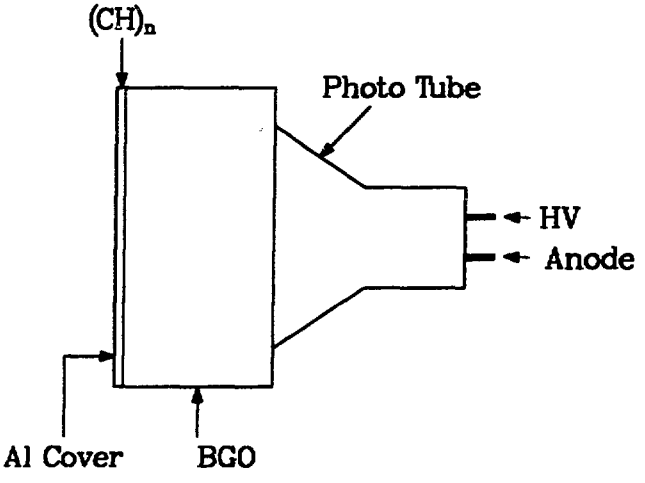

Fig. 2–9: Picture of the assembled plastic-BGO phoswich detector.

One advantage of using the phoswich detector is the clear separability of the pulse signals from the plastic scintillator and the BGO scintillator in a single phototube. This is possible because of the very different decay times of the scintillation light from the plastic scintillator ($\tau \sim$ 3ns) and the BGO crystal ($\tau \sim$ 300ns), as seen in Fig. 2–10. Also, a single photo-tube for each phoswitch detector reduces the number of photo-tube needed in the vacuum system. The electronics utilizing this two distinctive signals from the plastic and BGO are explained in subsection 2.2.4, and more details involved in decay/knocked-out particle identification will be made in chapter 3. The BGO crystal provides another benefit in size. Due to the combination of the high Z of bismuth and density of the BGO (7.13 gr/cm^3), the BGO material has a very high stopping power. This results in a reduction of the size of the detector. Some physical properties of BGO are shown in Table 2–3.

Table 2–3: The physical properties of BGO [Ha].

Pulse Height	10% of NaI(Tl)	Melting Point	1050°C
Decay Constant	0.30μs	Cleavage	None
Wavelength of maximum intensity	480 nm	Resistance to acids, bases	Inert
Afterglow	0.1% @ 3 msec	Crystal Structure	Cubic Eulytine
Refractive Index @480 nm @ 24°C	2.152	Linear Coeff. of Thermal Expansion	7×10^{-6}/°C 25 to 450°C
Hardness(Mho)	5.0	Hygroscopic	No

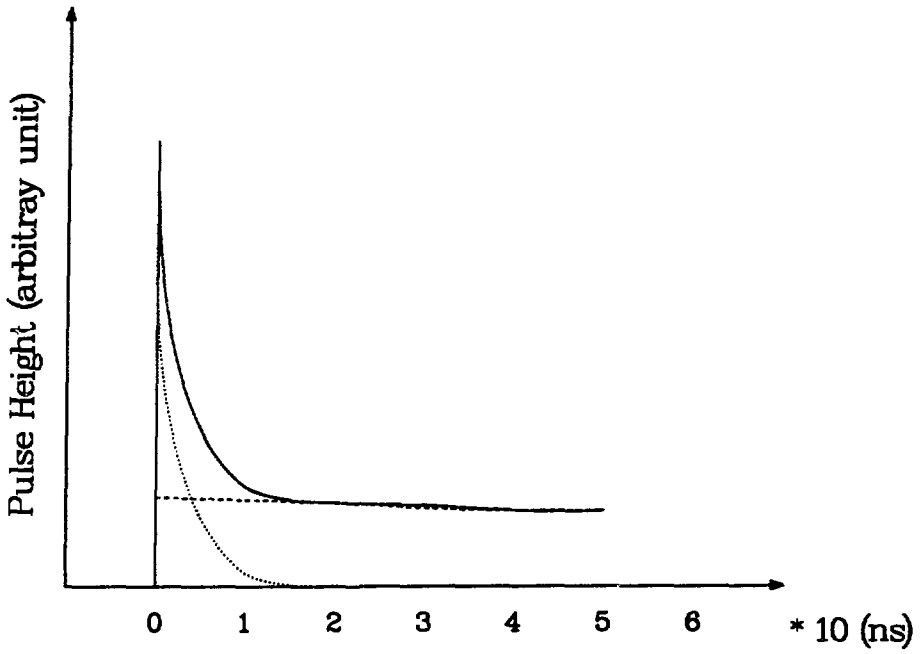

Fig. 2–10: Pulse height response of the plastic and BGO scintillator. The dotted line is for the plastic scintillator, the dashed for BGO crystal, the solid for the combined.

B. Scattered Particle Detection System

The scattered particles are detected by the detectors in the EPICS spectrometer. Delay-line multi-wire proportional chambers (MWPC), scintillators, and a freon Čerenkov counter are the chief components of the system. The Čerenkov detector, an electron-veto counter, was not used in this experiment because it is important only in low count reactions such as double charge exchange reaction where electrons constitute a substantial background.

(1) MWPC

Two MWPC [Mo-78, At-81, Mo-82] are used for each trajectory measurement of the scattered particles. One is the front chamber (F1-4) located near the focus of the quadrupoles (QM01-03), and the other is the rear chamber (R5-6, R9-10) mounted in the focal plane of the spectrometer (Fig. 2–8). Each chamber has the same components as shown in Fig. 2–11. The anode plane is composed of anode wires and alternate field defining cathode wires with 8 mm wire sapcings (anode to anode wire or cathode to cathode wire). The anode wires are soldered to a 2.5 ns/cm delay-line. The cathode wires are bussed together alternately, producing two cathode outputs per plane. The anode wires are operated at around 2150 Volt, while the cathode wires are at about ground potential. The anode plane is paired with a grounded aluminized-mylar foil cathode plane. The planes of each pair are offset from each other by $\frac{1}{2}$ wire spacing to provide redundant information for eliminating the left-right ambiguity in determining which side of a wire detects the passed particle. Four pairs of the front chamber planes measure

the coordinates of each particle: $x_f, y_f, \theta_f (= dx/dz)$, and $\phi_f (= dy/dz)$, while the rear chamber measures x_r, y_r, θ_r, and ϕ_r. The front chamber has an active area of 20×30 cm^2 and is operated in vacuum whereas the rear chamber has an active area of 30×90 cm^2 and is operated in air. Fig. 2-12 shows an assemblage of the chamber.

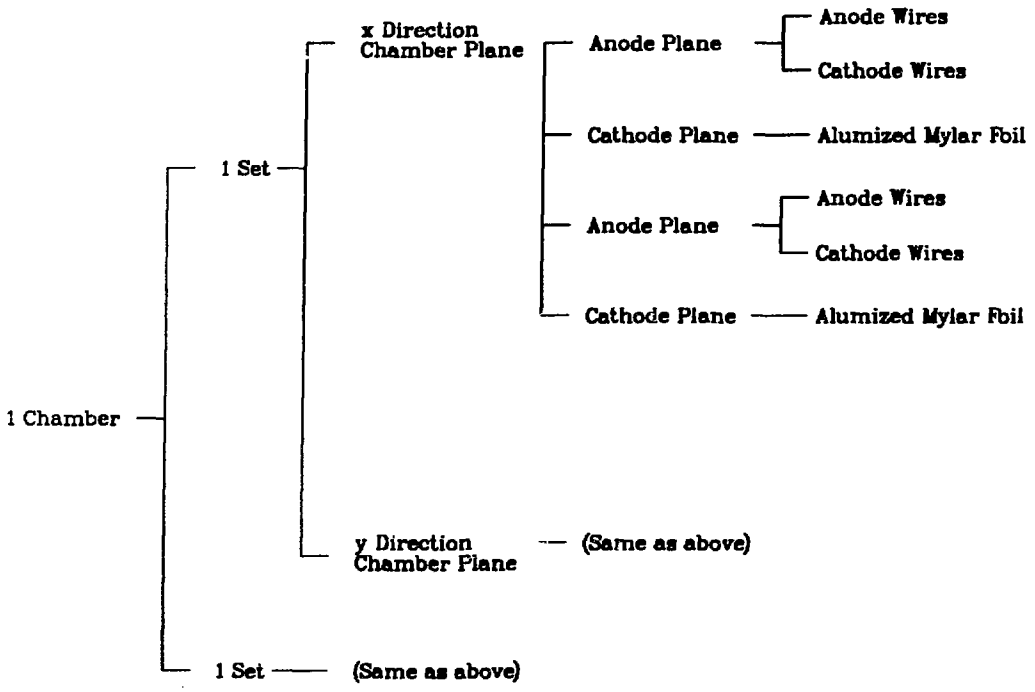

Fig. 2-11: Composition of the multi-wire proportional chamber.

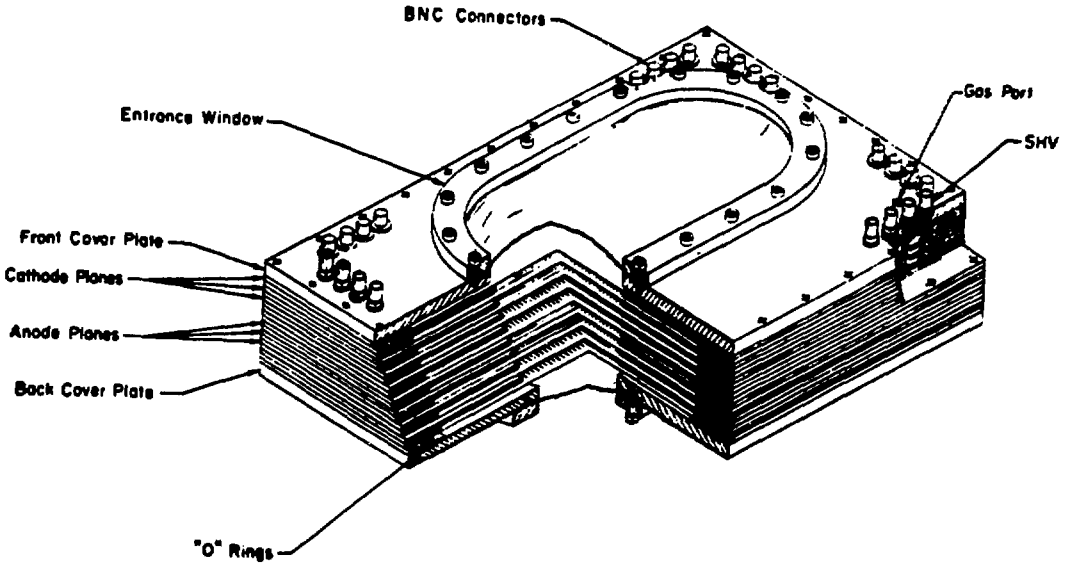

Fig. 2–12: Assemblage of the multiwire proportional chamber [Mo-82].

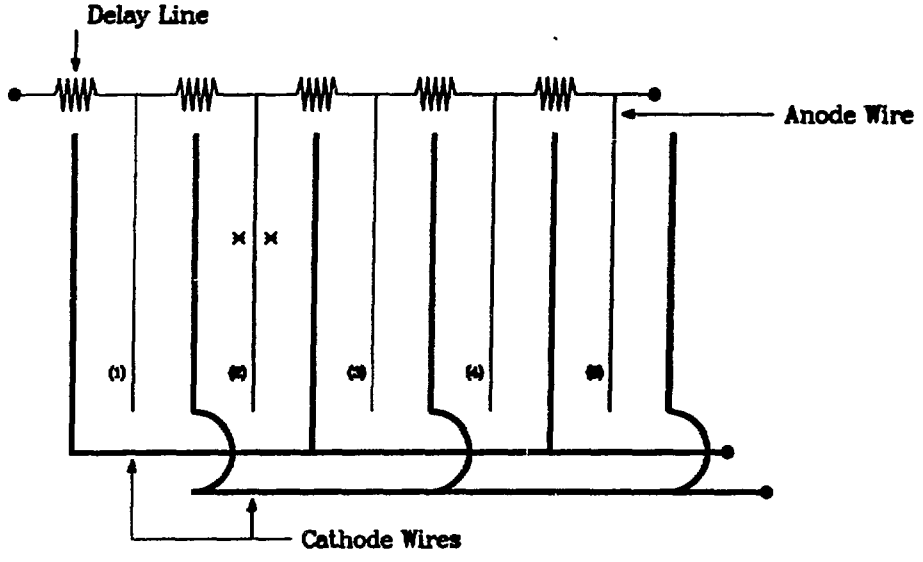

Fig. 2–13: A simplified anode wire plane.

Fig. 2–13 shows a simplified anode wire plane to illustrate how the position of a charged particle is measured. When a charged particle passes through a magic gas mixture (65% argon, 35% isobutane, 0.10% freon and 0.50% isopropyl alcohol) of the chamber, it produces electrons (firing the nearest anode wire) and inducing a positive pulse on the nearest cathode wire. Suppose there are five anode wires in the anode plane, If wire (2) is fired, then the time measured at the left end of the delay line is

$$T_{left} = 2t_{delay} + t_{drift}$$
$$\uparrow$$
fired wire number from the left

and the time measured at the right end of the delay line is

$$T_{right} = (5-2)t_{delay} + t_{drift} = 3t_{delay} + t_{drift}$$
$$\uparrow$$
the total number of wires in the anodeplane

where

t_{delay} = the characteristic time of the delay line for each wire spacing

and

t_{drift} = the drift time from the fired position to the nearest anode .

The time difference is

$$T_{diff} = T_{left} - T_{right}$$
$$= -1 \cdot t_{delay} .$$

Now we can assign -1 as the wire number (2). Similarly, -3, $+1$, $+3$, $+5$, $\cdots$ will be assigned as wire number (1),(3),(4) and (5). Thus, the digitized time difference information measures the position within $\pm$ 4 mm. The time sum,

$$\begin{aligned} T_{sum} &= T_{left} + T_{right} \\ &= 2 \cdot t_{drift} + 5t_{delay} \\ &\qquad\qquad \uparrow \\ &\qquad\qquad \text{the signal wire length correction} \\ &= 2t_{drift} + constant \end{aligned}$$

(always true regardless of which wire is fired) ,

measures the drift time for each event. After position calibration tha t includes the correction for signal dispersion and other non-linearities, the position resolution of the MWPC can be about 150μm (FWHM). The chamber can also be tolerated up to the maximum counting rates of several hundred KHz. A brief description of the wire chamber calibration will be presented in chapter 3. More details can be found in the work of Atencio et al. [At-81, Mo-82].

(2) Scintillators

There are nine scintillators (S1-S9) in the EPICS spectrometer (Fig. 2–8). The major function of the S1 scintillator is to be the reference point in obtaining the time of flight (TOF) information of the 9-m path to the rear scintillators S2 and S3. S1 is not usually used when good resolution is necessary because energy loss straggling degrades energy resolution. In the $(\pi, \pi' N)$ reactions reduction of

background was more important than resolution and, therefore, S1 was used. The scintillators S2 and S3, which are 1 m apart, further provide the TOF information of the outgoing particles. This information facilitates the separation of protons from π^+. Table 2–4 shows the time of flight measured between S2 and S3 for proton and pion.

Table 2–4: The time of flight of π and p between S2 and S3 [Pl-86].

E_π (MeV)	v_π (m/ns)	v_p (m/ns)	$\Delta t = t_p - t_\pi$ (ns)
100	0.244	0.061	12.3
500	0.284	0.122	4.7

Muons and electrons of the same momentum as the pion are major source of contamination of the pions in the spectrometer. These result from either elastic scatterings of the incident muons and electrons or from pion decays inside the spectrometer (see page 2). The contamination is especially bad at forward scattering angles (due to the pion decay cone), and low energy (due to the shorter decay length of the lower energy pion) (Table 2–1). Electrons can be separated using the time of flight method, but for muons whose mass is not much smaller than pions (m_μ = 105.66 MeV) the method is not very useful. Thus, a muon rejector is used to eliminate the muon contamination. Alternating wedges of graphite blocks and scintillators S4 through S9 form the EPICS muon rejector

[Mo-85]. Because of pion's nuclear interaction and shorter range (i.e., more energy loss) than muons of the same momentum, pions are absorbed by the graphites. Thus, the scintillation caused by the escaped muons is used to veto them. The thickness of each graphite block is varied so that it stops pions of a certain energy. That is, the graphite before S4, S5, S6, S7, S8, and S9 stops pions but not muons with kinetic energy of T_π = 100, 140, 180, 220, 260 and 300 MeV, respectively. Additionally, an absorber, which is the adjustable aluminum plates with various thickness, is used to fill the energy gap, i.e., for fine tuning, in the muon rejector.

C. Beam Monitoring System

Beam monitoring system at EPICS is composed of two ionization chambers (IC1 and BOT) and one charge integrating toroidal coil (1ACM02). IC1 is positioned in the scattering chamber on the same axis as the incoming beam down stream of the target, and monitors the intensity of the pion beam incident on the scattering target. The pion beam intensity is also monitored relatively to the primary proton beam current by 1ACM02 located upstream of the A-1 pion production target and BOT in the A-1 target cell. 1ACM02 that picks up the primary proton beam current was chosen as the beam flux monitor for this experiment. During the experiment the average pion flux was approximately 2.8 $\times$ 10^7 for π^+ and 1.5 $\times$ 10^7 for π^-, which were low enough to prevent the saturation of the BGO crystal with background.

2.2.4 EPICS Electronics and Data Acquisition

A. Signals

Two types of signals are handled at EPICS. One is analog signals from the scintillators and drift chambers. The other is logic signals of NIM (Nuclear Instrument Module) level and TTL (Transistor-Transitor Logic) level. NIM signals are typical in most fast logic circuitry used at EPICS such as discriminator and coincidence outputs. Width of NIM signal is variable depending upon application. TTL signals are primarily used for device status indications such as chamber voltage, gas, magnets and for slow logic. It is also used as LAMPF standard Beam Gate. Figure 2–14 displays the typical analog and digital signals acquired at EPICS.

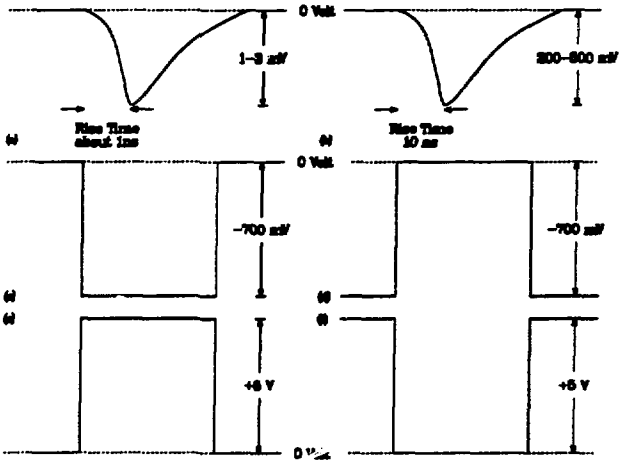

Fig. 2–14: Types of signals handled at EPICS:
(a) typical chamber pulse (b)scintillation pulse (c) standard NIM signal (d) complementary NIM signal (e) standard TTL signal (f) complementary TTL signal.

B. NIM Modules (Signal Controlling)

The analog signals of the scintillators, and the amplified and fastly discriminated chamber signals in the experimental areas are transmitted via coaxial cables to the NIM modules in the counting house. The NIM modules control the signals

by shaping, discriminating, delaying, and amplifying as necessary. The major electronic devices in the NIM modules are discriminators for timing information, coincidence units for logic information, mean timers for providing output pulse at time independent of impact position on double-ended scintillators, linear fan-ins/fan-outs for summing/distributing, logic fan-ins/fan-outs, and level shifters.

C. CAMAC Modules

The signals after the NIM modules are processed by the CAMAC modules, which contain Analog-to-Digital Converters (ADC's), Time-to-Digital converters (TDC's), and scalers. The ADC (now using FERA) is a charge-sensitive device, and integrates the charge in a linear pulse such as scintillator signal and digitize it in order to provide the computer with signal. For this experiment, in addition to the normal electronics set-up for ordinary single arm inclusive EPICS experiments, two integrating ADC's are used for each BGO phoswich detector. As seen in Fig. 2–15, the anode signal (comprising both a fast light pulse from the plastic scintillator and a slow light pulse from the BGO) is "viewed" by a single photo-multiplier tube. This signal is split by a linear fan out and sent into two different linear gates. These separated signals are then fed into two ADC's. The ΔE signal from the plastic is obtained using a short ($\approx$ 15 ns) gate and the E signal from the BGO is obtained using a longer ($\approx$ 300 ns) gate. TDC is used in order to convert time to charge at constant rate for the front and rear chamber pulses with common start and individual stops. The output S2·S3, where · is defined as logical "and", is adopted as the stop [Se-81]. The trigger, which is the

gate signal for the CAMAC modules, is called EVENT if

$$\text{EVENT} = S1 \cdot S2 \cdot S3 \cdot (\text{F1 } \textit{or } \text{F2}) \cdot (\text{F3 } \textit{or } \text{F4}) \, .$$

A Scaler is a device that counts NIM level pulses from IC1, BOT, 1ACM02. The scaler also scales signals from various sources such as EVENT and EVENT·NOT BUSY (i.e., EVENT·$\overline{\text{BUSY}}$) signals. The BUSY signal is generated by the Vax 11/730 computer that is interfaced to the CAMAC system through a LAMPF designed Microprogrammable Branch Driver (MBD). The computer can read only one EVENT at a time from the CAMAC system, otherwise, it produces the BUSY signal, meaning it cannot accept any events. The scalers are used for the estimation of the computer live (dead) time. A decade scaler is another scaler used as a part of fast clear circuit developed previously [Se-81]. The purpose of the fast clear circuit is to reduce elastic events which outnumber inelastic events, so that inelastic scatterings can be measured more rapidly. The signal from a single channel analyzer, resulting from a window on the elastic peak in the energy loss spectrum, is called fast clear signal, and sent to a fan-out unit, one of whose outputs goes to the decade scaler. Then, the decade scaler vetos 9 out of 10 elastic events before they are read into the computer, and count the events not rejected. More details about the fast clear circuit can be found in the thesis of Seestrom-Morris [Se-81]. In figure 2–16 the block diagram of the EPICS electronic logics is featured.

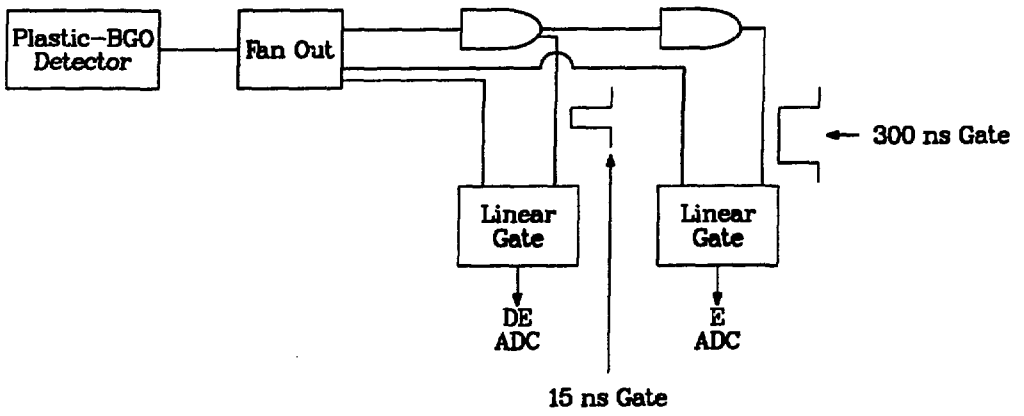

Fig. 2–15: Block diagram of the plastic-BGO phoswich electronics.

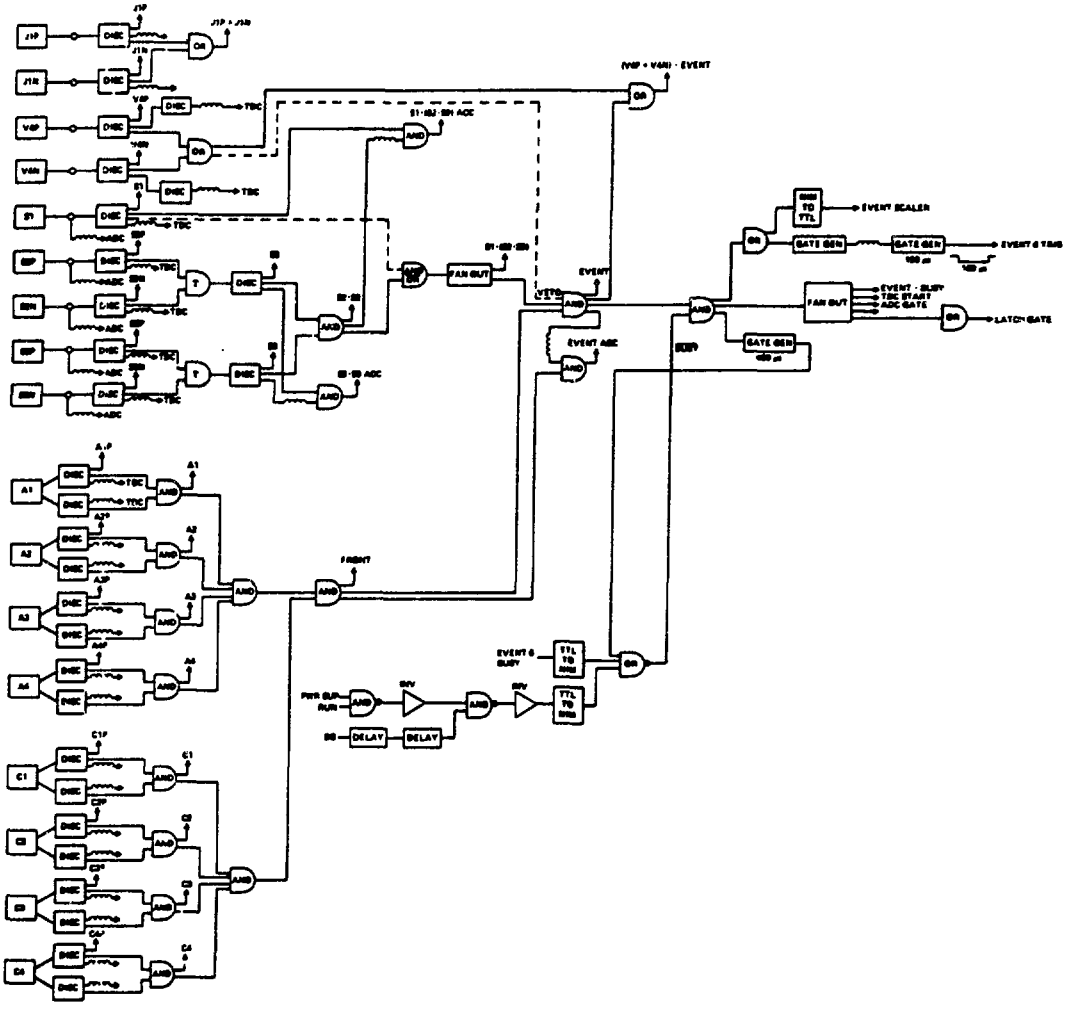

Fig. 2–16: Block diagram of the EPICS electronics.

D. The Q System for Data Acquisition and Analysis

The LAMPF standard Q system [Am-79] is a set of computer programs that enable the computer to read, record, analyze, and picture the data. When an EVENT is present the data acquisition processes it; that is, the Q program causes the computer to read the CAMAC modules and write the information to magnetic tape. The program also makes the computer to read out various scalers periodically. When the computer has time from EVENT acquisitions, the Q system does EVENTS analysis and histogramming, using the subroutines that can be discussed in three groups, an analyzer, a data testing package, and a histogramming package.

The analyzer is used to calculate coordinates, trajectories, and momentum of the particle of each EVENT from the ADC and TDC quantities read from CAMAC. The analyzer calculates P_π, $P_{\pi'}$ and θ_{scatt}, utilizing quantities $x_f, \theta_f, y_f, \phi_f, x_r, y_r, \theta_r, \phi_r$ measured by the multiwire chambers. The analyzer also computes timings of each decay/knocked-out particles.

The momentum of the incident pion, P_π, can be determined from the formula,

$$P_\pi = (1 + \delta_c) \cdot P_c \,, \tag{6}$$

where $\delta_c = \frac{x_{tgt}}{D_c}$ and D_c is the dispersion of the channel (due to the abberations in magnetic field) in units of cm/(% difference of P_π from P_c), and x_{tgt} is the x coordinate of the incident particle at the scattering target. In Eq. (6), δ_c is the unknown value, and it is acquired from the computation of the quantities x_{tgt}, y_{tgt}, θ_{tgt}, and ϕ_{tgt} as a fourth order polynomial of $x_f, y_f, \theta_f, \phi_f$, and x_r, respectively.

This polynomial optimization [Bo-79] is concisely explained in chapter 3 and Appendix I. The obtained coefficients of the polynomial from the optimization are saved in the POL.DAT file, which is read by the analyzer. P_π is then determined from the value of P_c given by the field in BM04. $P_{\pi'}$ can be calculated from

$$P_{\pi'} = (1 + \delta_{sp}) \cdot P_{sp} \ , \tag{7}$$

where δ_{sp} is also expressed as a polynomial of $x_f, y_f, \theta_f, \phi_f$, and x_r. Again, the coefficients are stored in the POL.DAT file, then, taking the value of P_{sp} from BM06, $P_{\pi'}$ is estimated. Scattering angle in the lab frame, θ_{scatt}, is obtained from

$$\theta_{scatt} = \theta_{spec} + \phi_{tgt} \ , \tag{8}$$

where θ_{spec} is the angle of the spectrometer with respect to the incident beam direction. For this experiment, ϕ_{tgt} was 0°.

CALKIN, a subroutine of the analyzer, calculates the excitation energy of the residual nucleus called the "missing mass", Q. Borrowing the relativistic relationship between the free particle's momentum (P) and energy (E), $E^2 = P^2 + m^2$ with $c = 1$, the missing mass Q can be expressed as

$$(E_{miss} + M)^2 = (Q + M)^2 + q^2 \ , \tag{9}$$

where E_{miss} is the missing energy, M is the mass of the residual nucleus, and q is the momentum transfer, $\vec{q} = \vec{P}_\pi - \vec{P}_{\pi'}$. To get E_{miss}, the energy balance equation for inelastic pion scattering from a target with the rest mass energy, M_0,

$$E_\pi + M_0 = E_{\pi'} + E_{miss} + M \ , \tag{10}$$

is also used. Then, expressing Eq. (10) for E_{miss} results in

$$E_{miss} = (T_\pi + M_\pi) + M_0 - \sqrt{P_{\pi'}^2 + M_{\pi'}^2} - M \,. \tag{11}$$

Thus, using the input values, P_π, $P_{\pi'}$, M_π and $M_{\pi'}$, the subroutine CALKIN calculates T_π, q and M, followed by E_{miss} in Eq. (11) and the missing mass Q in Eq. (9).

The test package provides for sorting (i.e, testing), based on the value of any data word for each EVENT. The test is done through two sets—macrotests and microtests. Macrotests use the results of the microtests using logical AND, NOT, and inclusive or exclusive OR. Microtests are tests on the values of raw data words and data words claculated in the analyzer. Microtests include BIT test, direct and indirect GATE test, and BOX test. The BIT test is for checking whether the specified bit in a given data word is satisfied. GATE test is for checking whether the value of the specified data word falls in between low limit and high limit, which are set either directly in a test file, or indirectly using computer key board that allows variable setting of the limits. BOX test is a combination of two GATE tests. The test package is very flexible since the test file can be changed and edited for user's needs. The sample test file is shown in Appendix II.

Viewing the pictures of the data is achieved by the Q histogramming and dot-plotting systems. In the histogramming system various tasks are used for creating, listing, plotting, printing, fitting, and saving histograms. Like the test package, the histogramming package uses a flexible histogram file, in which the user defines the histogram name, data (index) word(s) to be histogrammed, the

test(s) used in the test file, a lower and upper limit, and a binning factor (Appendix II). The function of the tasks can further be examined in the LAMPF user's guide. The dot plotting system also has similar user interfaces, but a dot plot is used for a 2-dimensional-live display of data for diagonostic purposes of the system. Fig. 2–17 illustrates the data flow that we have described so far in a diagram. The experimental information of this thesis experiment is also epitomized in Table 2–5.

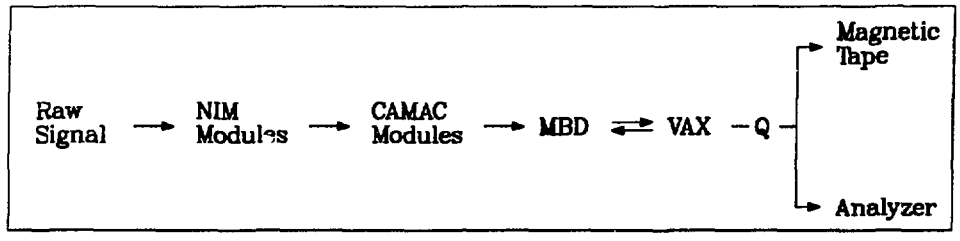

Fig. 2–17: EPICS data flow diagram.

Table 2–5: Summerized experimental information of the experiment 1039.

T_π	180 MeV
Target	^{12}C 91 mg/cm^2 ^{208}Pb 150 mg/cm^2 CH_2 73 mg/cm^2 (normalization) CH_2 70 mg/cm^2 (calibration)
Phoswich Detector Angle	120°, 90°, −60°, −90°, −120°
$\theta_{scattering}$	20° (lab frame)
θ_{tgt}	60° (^{12}C, ^{208}Pb, normalization) −50° (calibration)

Chapter 3. Event Analysis and Results

The parameters used by the software analyzer were obtained from the calibration of multiwire chamber and polynomial optimization for scattered particle trajectory, and the calibration of the five plastic-BGO detectors. The chamber calibration and polynomial optimization were carried out during the development period at the beginning of the experiment cycle 50, while the five BGO phoswich detectors were calibrated by replaying the already recorded data in the magnetic tapes.

The purpose of chamber calibration is to determine the parameters needed to calculate positions accurately from the times read in from the chambers. The ploynomial optimization is important because it calibrates the measurement of the outgoing particle momentum at the spectrometer as well as it improves the resolution of the missing mass histogram. A procedure called a δ scan is used to achieve the optimization. In this procedure elastic scattering from a heavy target (usually thin 93Nb target) is measured for a fixed spectrometer magnetic field and varying channel fields. The calculated momenta from a program (COFEPX) [Bo-79] is linear-least-squarelly fitted to the expected values. Typical procedures of the chamber calibration and polynomial optimization are presented in Appendix I. The details of the phoswich detector calibration will be discussed in section 3.1.

One of the ultimate purposes of the Event analysis is to obtain a clean missing-mass histogram. Background contaminating the outgoing pions must be removed. To eliminate background events a Good Event Test is used. This test

includes a particle identification test (PID), a good chamber test, and background rejection tests.

The PID test, done lively during on-line data acquisition, is a box cut on a 2-dimensional dot plot of the time-of-flight between S2 and S3 versus the geometric mean of the pulse heights in S2 and S3. This test removes protons due to proton's longer time of flight than that of a pion with the same momentum (see Table 2–4). Because of the short distance between S2 and S3, however, the pions are not easily distinguished from background electrons and muons. For these particles, the TOF from S1 to S3 and the muon rejection system (Chapter 2) are used, along with the various background rejection tests that will be described below.

The Good chamber test is composed of drift-time and drift-difference tests. The drift-time tests inspect the drift times of each event in each of the sixteen chamber planes. The drift time should be within the range of the time that is confined with the maximum drift distance of 4 mm in each cell in each plane. Therefore, the drift-time tests check whether events generate signals within a cell (4 mm) in one or more planes of sixteen chamber planes. Only events that generate signals with the physical drift times in all sisxteen chambers are accepted. The drift-difference test throws away events whose drift distance is more than 4 mm in each plane. This can be done by comparing the measured position of each event from the drift time information to the fitted line of the measured position in each plane. The drift-difference tests help eliminating pions that decay between the wire chambers as well as particles passing through the chambers

simultaneously [Se-81].

The background rejection tests are the combination of gate tests set on the six data-words XTGT, YTGT, PHITGT, THTTGT, THTCHK (θ_{check}) and PHICHK (ϕ_{check}). XTGT and YTGT represent the x and y coordinates of the scattering centers at the target. PHITGT and THTTGT are the angular directions of the scattered pion at the target, i.e, PHITGT being $dy/dz(= \phi_{tgt})$, and THTTGT $dx/dz(= \theta_{tgt})$. Histograms of these first four data-words exhibit relatively sharp edges as shown in Fig. 3–1 for the XTGT. Thus, events outside edges were discarded as not corresponding to events in the scattering target. THTCHK and PHICHK are obtained from the difference between the front angles measured at the front chambers and those calculated from the optimized polynomial that uses the information measured at the rear chambers. If the difference is more than ± 10 mr (which is the typical difference for good pion events), then the event is rejected. Since an opening angle of the $\pi \rightarrow \mu + \nu$ decay cone ranges from $\sim$ 230 mr at $T_\pi = 292$ MeV to $\sim$ 550 mr at $T_\pi = 120$ MeV, the THTCHK and PHICHK histograms are very useful in purging muon background from the π decay in the spectrometer [Se-85]. Fig. 3–2 shows the missing-mass histogram of pions that have passed the Good Event Test.

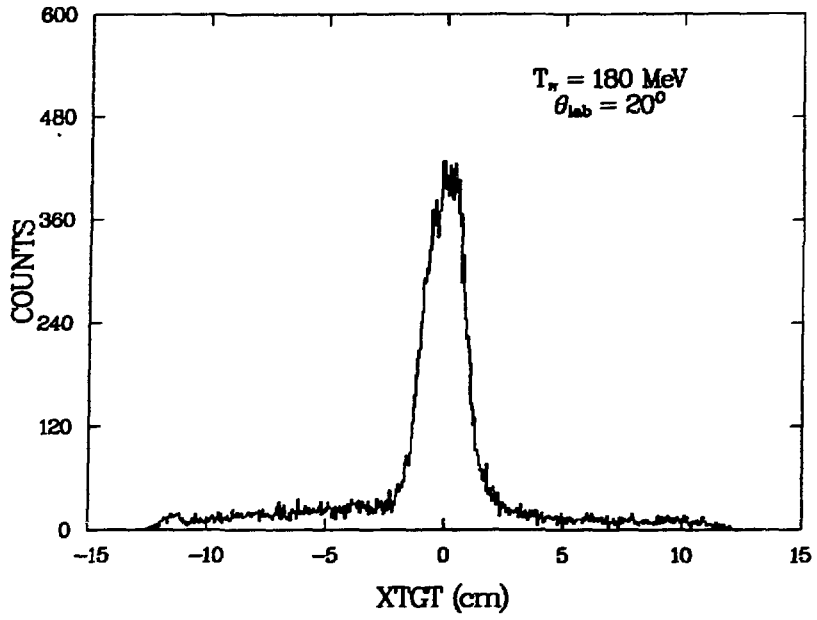

Fig. 3–1: XTGT histogram. Target was ^{12}C. Scattering angle was at 20°.

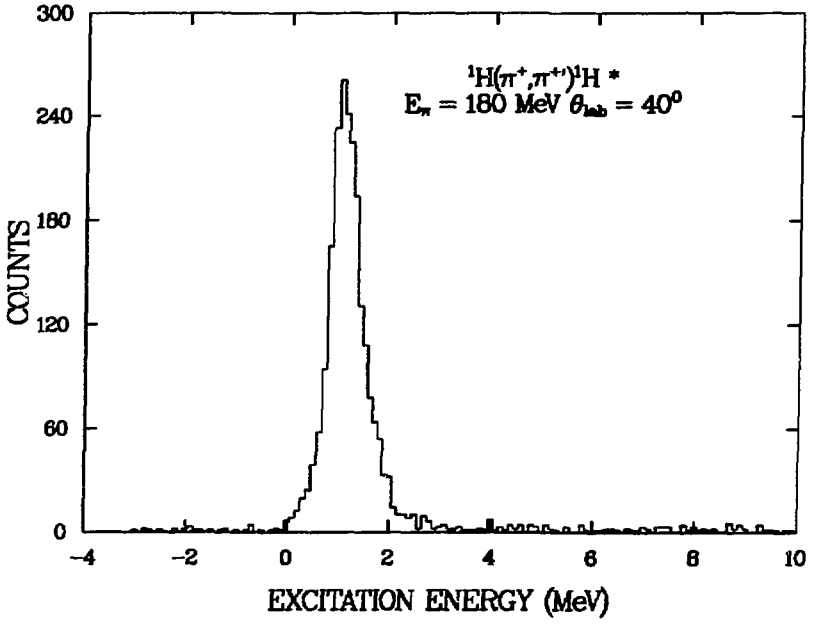

Fig. 3–2: Missing mass histogram. The elastic peak is not at 0 MeV due to mis-setting of the magnetic field.

3.1 Event Analysis of $^{12}C(\pi^{\pm}, \pi^{\pm\prime} p)$ reactions

(1) Calibration of the BGO phoswich detectors

The purpose of the calibration of the BGO-phoswitched detectors is to determine accurate values of E and ΔE separately from the raw (uncalibrated) "short" (plastic) and "long" (BGO) signals which are a mixture of both E and ΔE. For the calibration a CH_2 target with areal density of 70mg/cm^2 was used. The incident pion energy was 180 MeV. The lab scattering angle was 70°. Each of the proton detectors was positioned at $-50°$ which is near the angle at which most of protons with $\sim$ 47.4 MeV from the $^1H(\pi^+, \pi^{+\prime})^1H$ reaction are expected to come out. The detector angle was large enough to prevent the scattered pions (particles) off the flange of the spectrometer from entering it.

Fig. 3–3 shows typical 2-dimensional ΔE versus E plots of the (uncalibrated) raw data from the calibration target (CH_2) and the ^{12}C target respectively. The uncalibrated ΔE–E plot from the ^{12}C shows charged particles that stopped in the plastic scintillator [band **1**], charged particles that passed through the plastic scintillator and stopped inside the BGO detector [band **2**], and neutral particles that had passed through the plastic scintillator and created signals inside the BGO detectors [band **3**]. Since the plastic scintillator(CH_2) was thin (0.3 cm), the neutral particles did not deposit much energy in the ΔE counter. The ΔE–E plot of the calibration target shows most particles in the band **2** since the prtons are emitted with nearly the same high energy ($\sim$ 47 MeV). The tail toward high energies is due to pile-up (saturation) in the BGO detector. Because

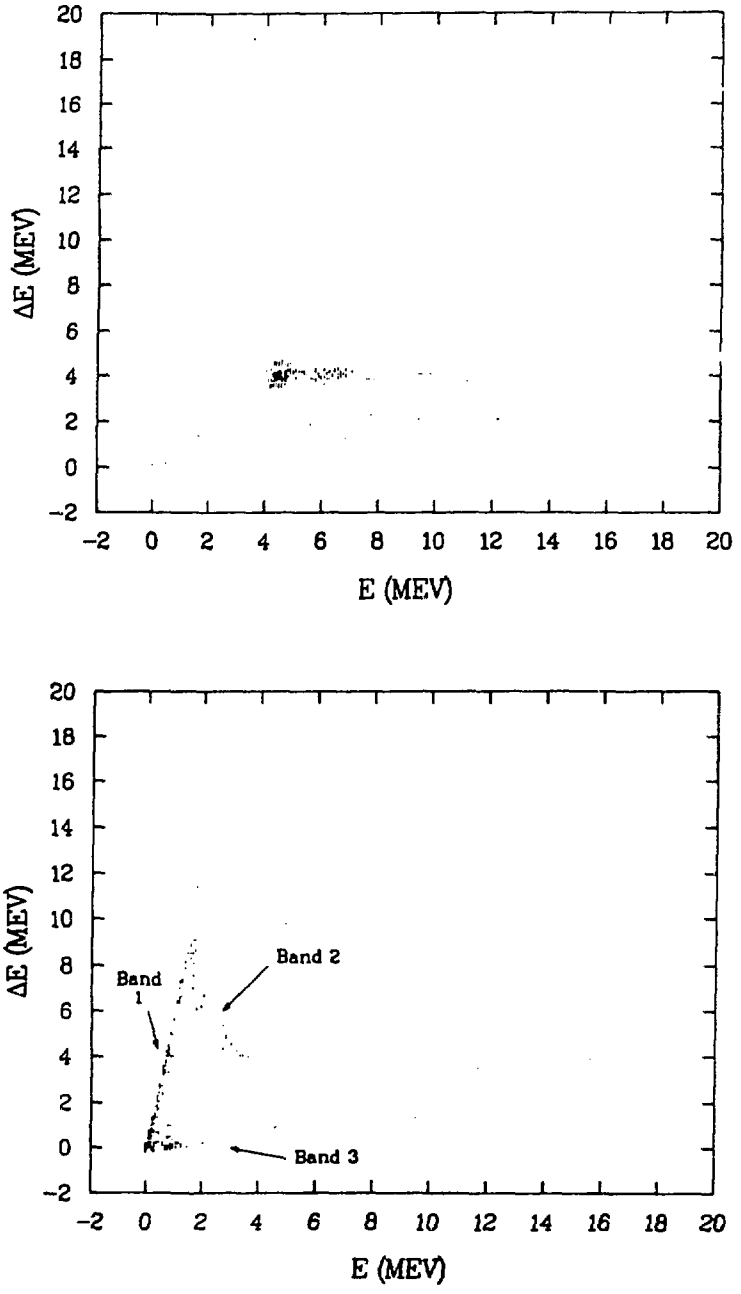

Fig. 3–3: Uncalibrated ΔE–E plots from the calibration target (top) and the ^{12}C target (bottom). Here ΔE and E shoud have been designated as "short (15ns gate)" and "long (300ns gate)" because the raw signlas separated by the two ADC gates for each photo-tube are still mixtures of both pure plastic (ΔE) and BGO (E) signals .

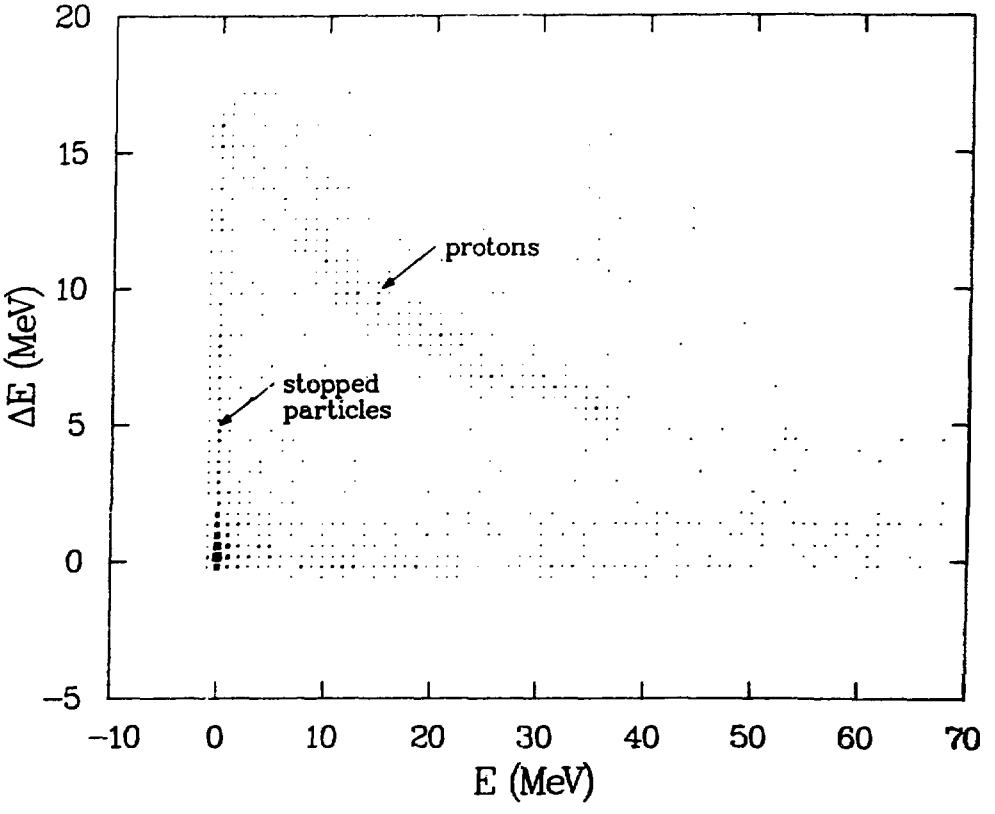

Fig. 3–4: Calibrated ΔE–E plot.

of this lack of events in the ΔE counter, the data from the ^{12}C target was also used in addition to the CH_2 calibration runs to reach the ultimate calibrated plot demonstrated in Fig. 3–4.

The starting step of the calibration was to rotate the raw data in Fig. 3–3b so that the band **1** and **3** could be perpendicular to each other like in Fig. 3–4. For this purpose one of the ^{12}C runs was chosen because those runs showed enough events in both bands. To obtain the right rotation parameters, ROT1 and ROT2, the following simple formulae were used.

$$E_{rot} = (E_{unrot} + DE_{unrot} \times ROT1) \cdot EGAIN \text{ [for band 1]} \quad (12)$$

$$DE_{rot} = (DE_{unrot} + E_{unrot} \times ROT2) \cdot DEGAIN \text{ [for band 3]} \quad (13)$$

Let DEGAIN and EGAIN be 1 tenatively. Then, using the average values in the perpendicularly rotated band **1** and **3**, $\overline{E}_{rot} = 0$ and $\overline{DE}_{rot} = 0$ produce

$$ROT1 = -\frac{\overline{E}_{unrot}}{\overline{DE}_{unrot}}$$

and

$$ROT2 = -\frac{\overline{DE}_{unrot}}{\overline{E}_{unrot}}$$

from Eq. (12) and Eq. (13), respectively.

The next step was to find correct parameters, EGAIN and DEGAIN, which locate the certain energy of the emitted particle in the anticipated position in the ΔE–E plot. The proton with kinetic energy of ~ 47.4 MeV from the $^1H(\pi^+,\pi^{+\prime})^1H$ reaction was used. The energy loss for this proton in the thin plastic scintillator due to the ionization is about 4 MeV, and the energy loss in the calibration-CH_2

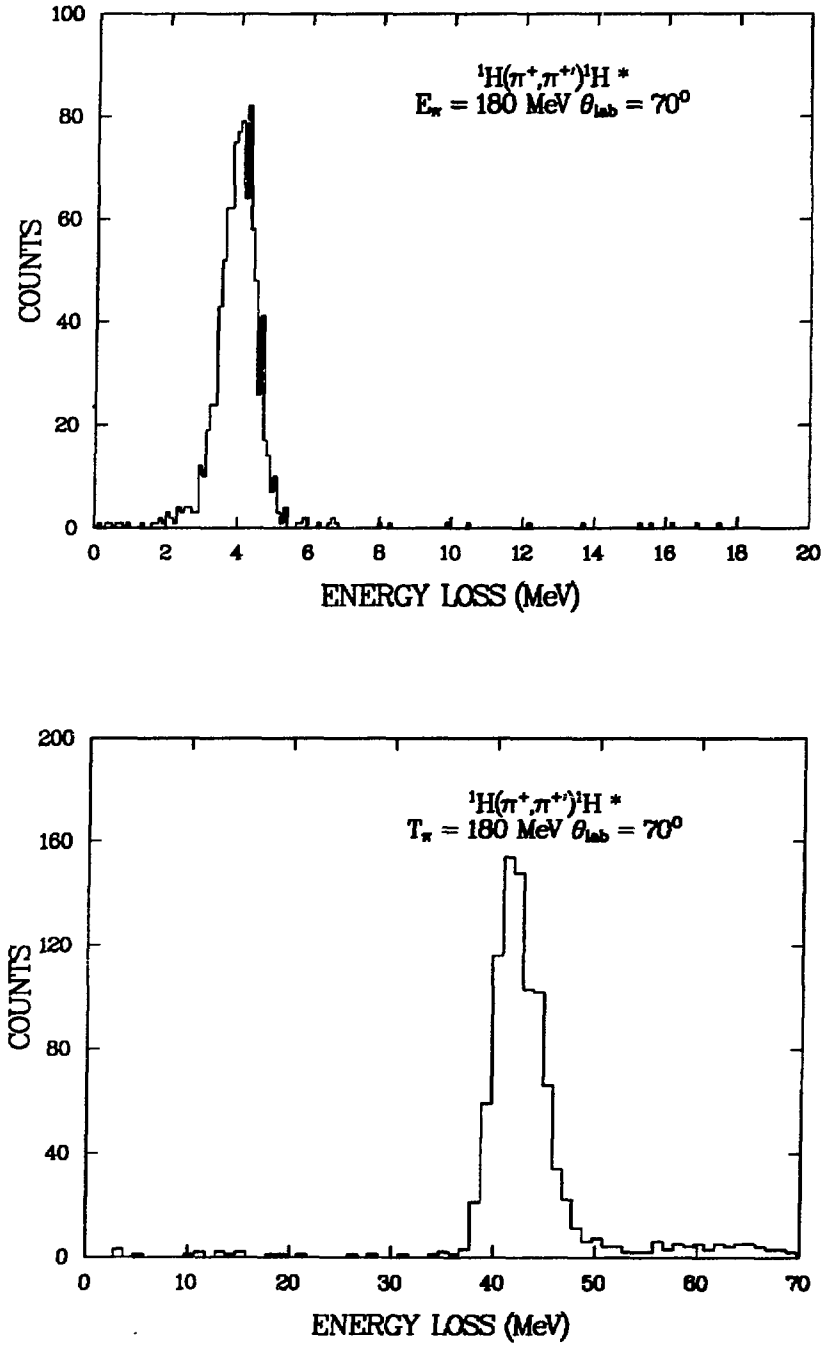

Fig. 3–5: Energy loss of the emitted protons in the plastic scintillator (top) and the BGO crystal (bottom).

target is $\sim$ 0.5 MeV at the center of the target. Thus, the expected value of DE and E of the specific proton is approximately 4 MeV and 42.9 MeV. The multiplication factors, EGAIN and DEGAIN, were adjusted until those values were obtained (Fig 3–5).

The thin plastic scintillator used for this experiment could stop a proton with the kinetic energy up to around 16.5 MeV. Checking this cutoff piont provides a mean to evaluate whether the DEGAIN correction has been made rightly. Again, using one of the ^{12}C runs, DEGAIN was corrected. The result is the calibrated ΔE–E plot in Fig. 3–4.

(2) Proton Identification

A box was set up on the ΔE–E plot (Fig. 3–4) to identify and select low energy decay protons from the ^{12}C target, which were stopped inside the plastic scintillator with kinetic energy less than about 18 MeV. This task was achieved by using the different flight time for different types of particles from the target to the plastic-BGO detectors. That is, the protons in this box ($2 \leq$ DE ≤ 20 MeV and $-2 \leq$ E ≤ 2 MeV) were separated from other particles using the time of flight information with respect to the spectrometer (from S1 to S3). The blob shown in Fig. 3–4 wasn't included since it is mainly pedestals and low energy neutrals. The picture shown in Fig. 3–6 (top) is a histogram called CT, which is the histogram of corrected time of flight of emitted particles from the target to the plastic-BGO detector based on pion mass. Between channel 100 and 150 the CT histogram shows protons with various velocities. The corrected time of

flight based on proton mass, CTP, is shown in the bottom part of Fig. 3–6, displaying the obvious proton peak near channel 100. The events above channel 100 represent heavier particles such as deuterons and alphas as well as accidentals. Lighter particles than protons appear in the lower channel numbers. A gate was set around the proton peak to separate protons from the other particles.

The band with the slope identified as protons in our ΔE–E plot (Fig. 3–4) mainly represents the high energy decay protons. The heavier particles with high kinetic energies would appear in higher locations because of higher energy loss in the ΔE detector due to higher charges. Not many heavier particles are seen. In order to set up a box to gate protons in the slope in an easy fashion, the proton ΔE-E slope was fitted with a straight line using logarithms up to 3rd order. That is, the purpose was to make those protons that passed the plastic but stopped in the BGO come out in a straight band as shown in Fig. 3–7. The CTP test was additionally used to ensure that they were the protons. The block diagram made in Fig. 3–8 is the proton identification algorithm adopted in the analyzer. A good proton event must not only pass the tests described in the algorithm, but also be in coincidence with a good pion event. Fig. 3–9 is a 2-dimensional histogram of missing mass in ^{12}C versus the total energy of the decay protons. The approximately 45° line is due to protons from direct–knockout; this line can be used to judge how well the calibration was done.

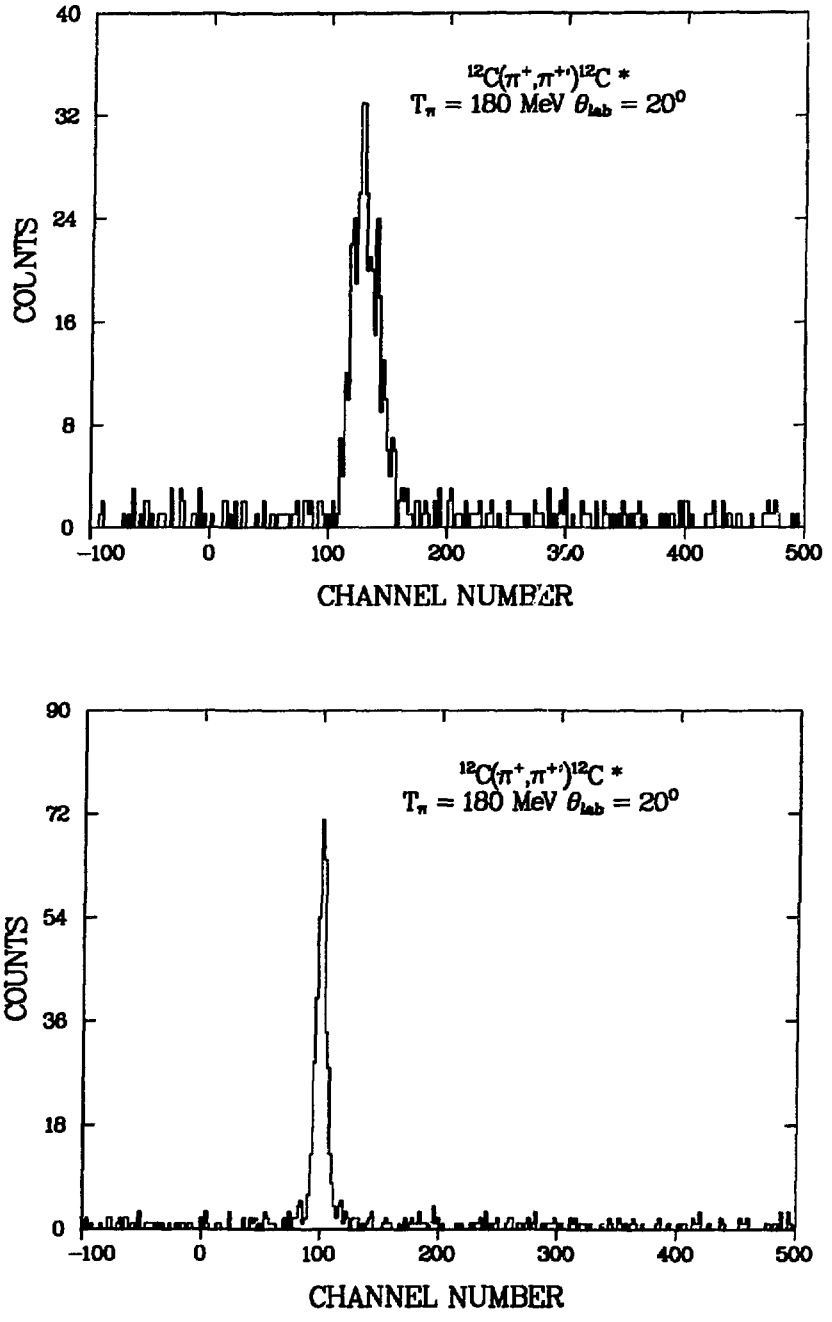

Fig. 3–6: CT (top) and CTP (bottom).

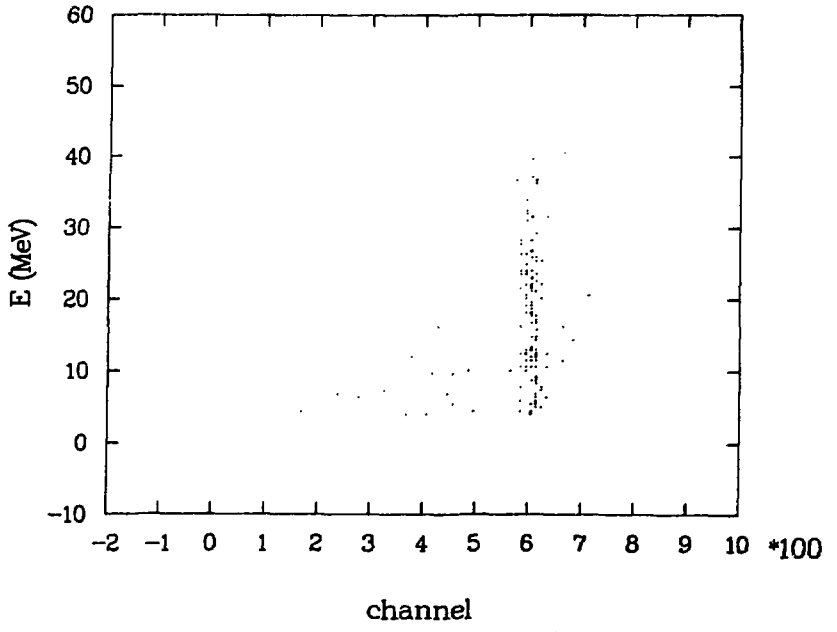

Fig. 3–7: PID vs. E. "Channel" shoud have been designated as PID.

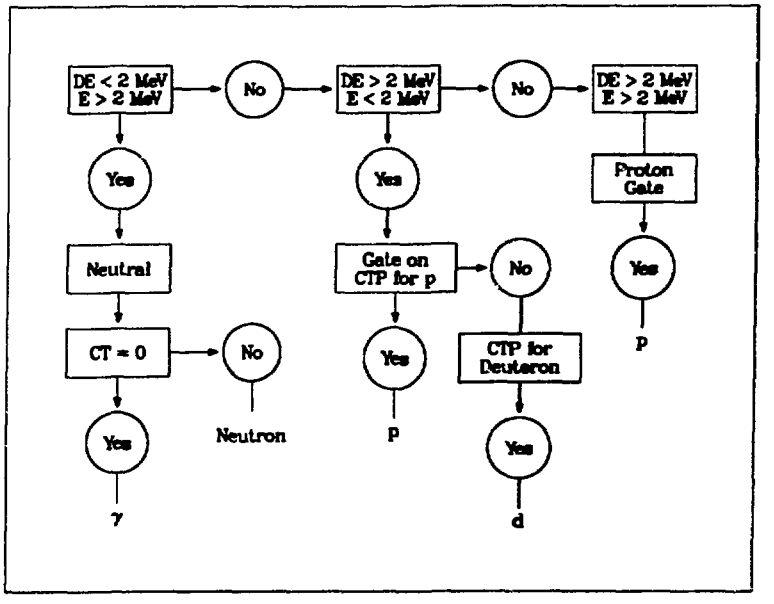

Fig. 3–8: Proton identification algorithm.

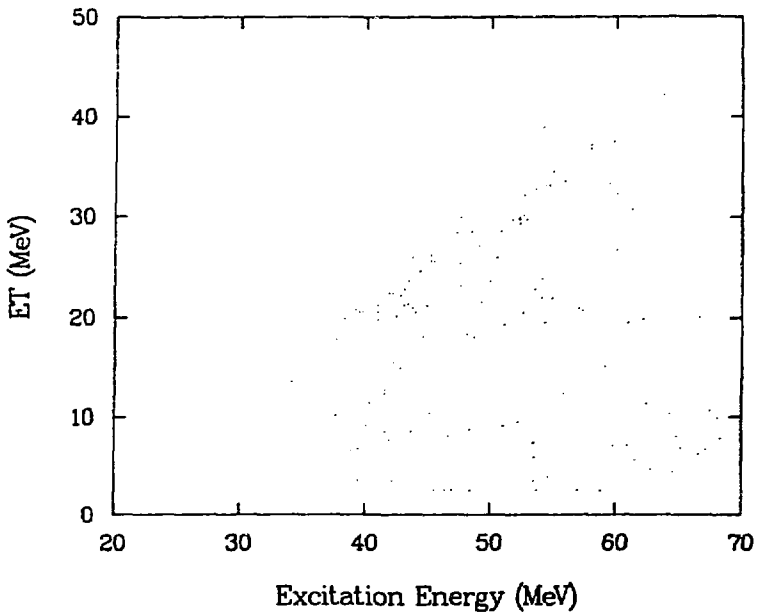

Fig. 3–9: Missing mass (^{12}C) vs. total energy of emitted particle (ΔE + E).

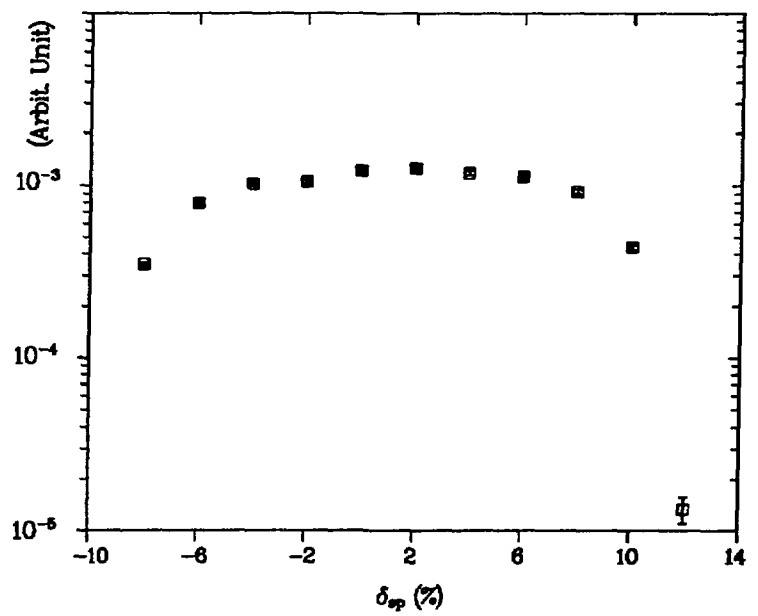

Fig. 3–10: Acceptance scan.

(3) Acceptance Scan

The EPICS spectrometer acceptance (solid angle $\Delta\Omega_{sp}$, designed to be 10 msr), varies as a function of outgoing pion momentum (i.e., different excitation energy). The acceptance is calibrated by measuring elastic scattering yields at a fixed beam energy for various values of spectrometer field. This procedure is called the "acceptance scan".

A previously measured acceptance scan was used for this experiment. The target was 93Nb with areal density of 66 mg/cm^2. The incoming beam was π^+ with the kinetic energy of 180 MeV. The scattering angle was 20°.

During this experiment the beam-defining jaws were set more narrowly than in the acceptance scan runs. Therefore, a narrow gate (-1.35 cm $\leq$ x $\leq$ 1.35 cm) on XTGT was applied in the missing mass histogram of the acceptance runs. The results of the acceptance scan are shown in Fig. 3–10. Because of the narrow XTGT gates this acceptance scan is flatter than a typical EPICS acceptance scan. The two momentum bites used for the ^{12}C($\pi^{\pm}, \pi^{\pm\prime}$p) reaction put $E_x(^{12}C)$ = 22 MeV and 52 MeV respectively at δ_{sp} = 2%.

(4) Normalization

The formula for the conversion of the counts contained in a missing mass histogram to the differential cross section in the lab frame can be expressed as

$$\left(\frac{d\sigma}{d\Omega}\right)_{lab} = \left(\frac{Counts \cdot CF}{N_\pi \Delta\Omega_{sp}}\right) \cdot \frac{1}{N_{tgt}} \times NF$$

$$= Yield \cdot \frac{1}{N_{tgt}} \times NF \qquad (14)$$

where

$$
\begin{aligned}
Counts &= \text{the number of counts in the peak} \\
CF &= \text{an efficiency correction factor for the detection system} \\
N_\pi &= \text{the number of the incident } \pi \\
\Delta\Omega_{sp} &= \text{solid angle of the spectrometer} \\
N_{tgt} &= \text{the number of target nucleons per unit area.}
\end{aligned}
$$

The factor CF is given by,

$$
CF = \frac{\cos\theta_{tgt}}{LT \cdot CHEFF \cdot DREFF \cdot LEV \cdot SF} \quad . \tag{15}
$$

Here, $\cos\theta_{tgt}$ is included because the beam is not incident normally on the target (Fig. 2–7). LT is the computer life time defined as Events·($\overline{\text{Busy}}$)/Events. CHEFF is the product of each chamber efficiency. The drift efficiency, DREFF, is the number of events that passed the drift-difference tests over the drift-time tests. The loop per event, LEV, is the ratio of the number of events analyzed by the computer to the total number of taped events. The survival fraction SF, the fractions of pions that does not decay between the target and the S3 scintillator, can be calculated from the formula,

$$
\begin{aligned}
SF &= e^{(-t/\tau_\pi^{lab})} \\
&= \exp\left(-\frac{Lm_\pi}{P_\pi \tau_\pi^{lab}}\right)
\end{aligned} \tag{16}
$$

where

$$
\begin{aligned}
t &= \text{the pion flight time in the lab system} \\
\tau_\pi^{lab} &= \text{the pion life time in the lab system} \\
&= \frac{\tau_\pi^{rest}}{\gamma} \\
\tau_\pi^{rest} &= \text{the pion life time in its rest frame} \\
\gamma &= \frac{1}{\sqrt{1 - v^2/c^2}} \\
\mathrm{P}_\pi &= \gamma m_\pi v \\
L &= \text{the path length} \\
&= 12.28 - 0.035\delta_{sp} \text{ (meters)}
\end{aligned}
$$

The number of incident pions, N_π, and the spectrometer solid angle, $\Delta\Omega_{sp}$, cannot be measured absolutely in the EPICS system. For N_π the value of 1ACM02 was used for relative pion fluxes and for $\Delta\Omega_{sp}$ DOMEGA from the aceptance scans was used for relative solid angle. Because N_π and $\Delta\Omega_{sp}$ are not measured absolutely overall normalization factor NF is obtained from comparing yields from $\pi^\pm$ + p scattering to cross sections calculated from the phase shifts of Rowe, Salomon, and Landau [Ro-78]. Thus,

$$
\text{Yield} = \left(\frac{Counts \cdot CF}{1ACM02 \cdot DOMEGA}\right) \tag{17}
$$

$$
\left(\frac{\text{Yield(H)}}{\text{N}_{tgt}\text{(H)}}\right)_{\text{data}} NF = \left(\frac{\mathrm{d}\sigma}{\mathrm{d}\Omega}\right)^{\text{H}}_{\text{known}} \tag{18}
$$

One of the inputs to Eq. (14), N_{tgt} (nucleons/mb), can be calculated from

$$
N_{tgt} = \frac{\rho_{tgt}\left(\frac{gr}{cm^2}\right) N_A \left(\frac{atoms}{mole}\right) \times 10^{-27}\left(\frac{cm^2}{mb}\right)}{M_{tgt}\left(\frac{gr}{mole}\right)} \tag{19}
$$

where ρ_{tgt} is the areal density of the target, N_A, is Avogadro's number, and M_{tgt} is the mass of the target. For the π + p normalization using CH_2 target, the formula (14) can be expressed as

$$\left(\frac{d\sigma}{d\Omega}\right)_{lab} = \frac{Y(tgt)\ A_{tgt}}{\rho_{tgt}\ N_A \times 10^{-27}} \left(\frac{d\sigma}{d\Omega}\right)^{H}_{known} \frac{1}{Y(H)} \frac{2}{14} \rho_{CH_2}\ N_A \times 10^{-27}$$

$$= \frac{2}{14} \frac{Y(tgt)A_{tgt}}{\rho_{tgt}} \left(\frac{d\sigma}{d\Omega}\right)^{H}_{known} \frac{\rho_{CH_2}}{Y(H)} \qquad (20)$$

from EQ. (17), (18), and (19). The conversion from the lab system to the CM system can be made, multiplying Eq. (14) by Jacobian. The picture shown in Fig. 3-11 is a normalization fit for the hydrogen elastic peak by using the program NEWFIT written by C. L. Morris [Mo].

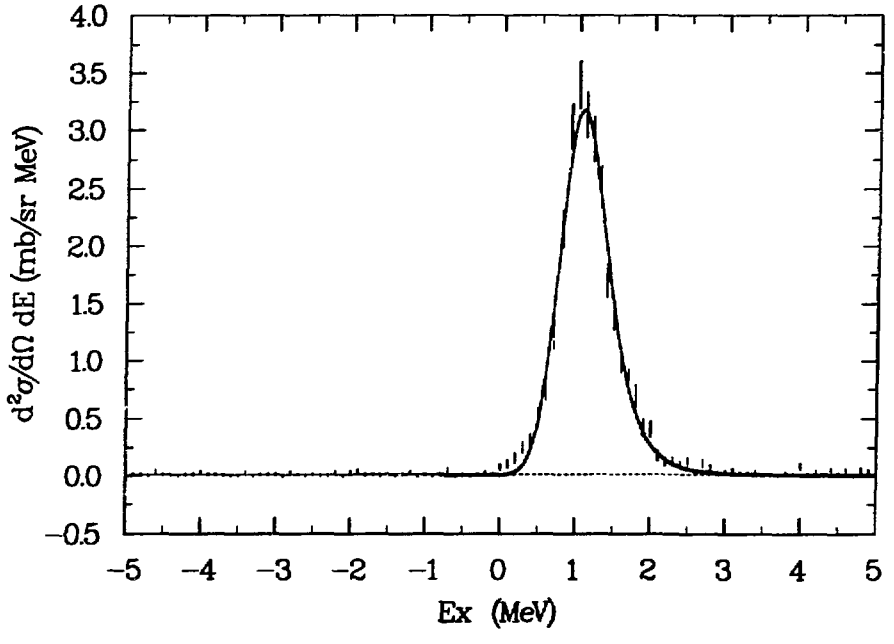

Fig. 3-11: Normalization Fit.

3.2 Results of $^{12}C(\pi^{\pm}, \pi^{\pm\prime}p)^{11}B$ reactions

Acceptance-corrected missing mass spectra for π^+ and π^- inelastic scattering at $\theta_{lab} = 20°$ for $T_\pi = 180$ MeV are plotted in Fig. 3-12. The 20° scattering angle was chosen since it is near the maximum in the angular distribution for the GDR in ^{12}C [Bl-84]. The π^+ and π^- cross sections are nearly equal everywhere as expected in a self-conjugate nucleus because of charge symmetry. An exception occurs for isospin mixing as observed in a doublet near 19 MeV ($J = 4^-$; $T = 0$, 1) [Co-87].

Figure 3-13 and 3-14 show the $^{12}C(\pi^+, \pi^{+\prime}p)$ and $^{12}C(\pi^-, \pi^{-\prime}p)$ exclusive cross sections measured at $T_\pi = 180$ MeV and $\theta_{lab} = 20°$. The top panel of each figure represents the ^{12}C missing mass spectrum, gated by the requirement of detecting a coincident proton at an energy which implies that the excitation energy of the residual nucleus, ^{11}B, is less than 10 MeV, and summed over all five proton detectors. In contrast to the inclusive singles spectra above $E_x(^{12}C) = 20$ MeV, the exclusive $(\pi, \pi' p)$ coincidence yields are larger for π^+ than π^- throughout the spectrum. The missing mass spectrum gated by detecting a proton leading to excited states of ^{11}B higher than 10 MeV is shown in the lower part of each figure. In this case, which includes multiparticle break-up states, the $(\pi^+, \pi^{+\prime}p)$ and $(\pi^-, \pi^{-\prime}p)$ cross sections are about the same for all excitation energies. One thing to note is that the 4 MeV threshold for proton detection in our phoswich detectors seems to have minimal effect on the results of our coincidence data since we are considering the region above the excitation energy of 20 MeV in ^{12}C.

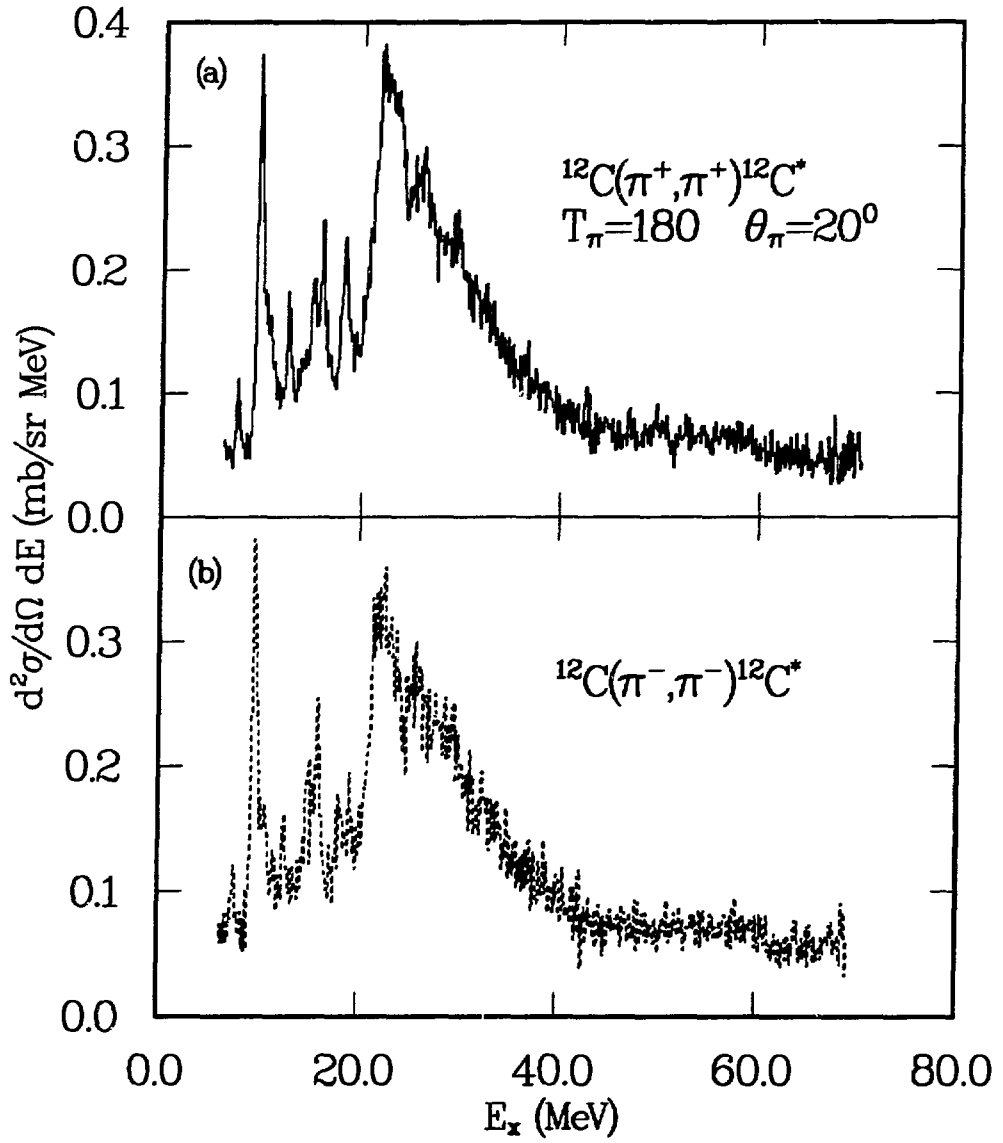

Fig. 3–12: Missing mass spectra for $^{12}C(\pi^{\pm},\pi^{\pm\prime})^{12}C^*$ reaction.

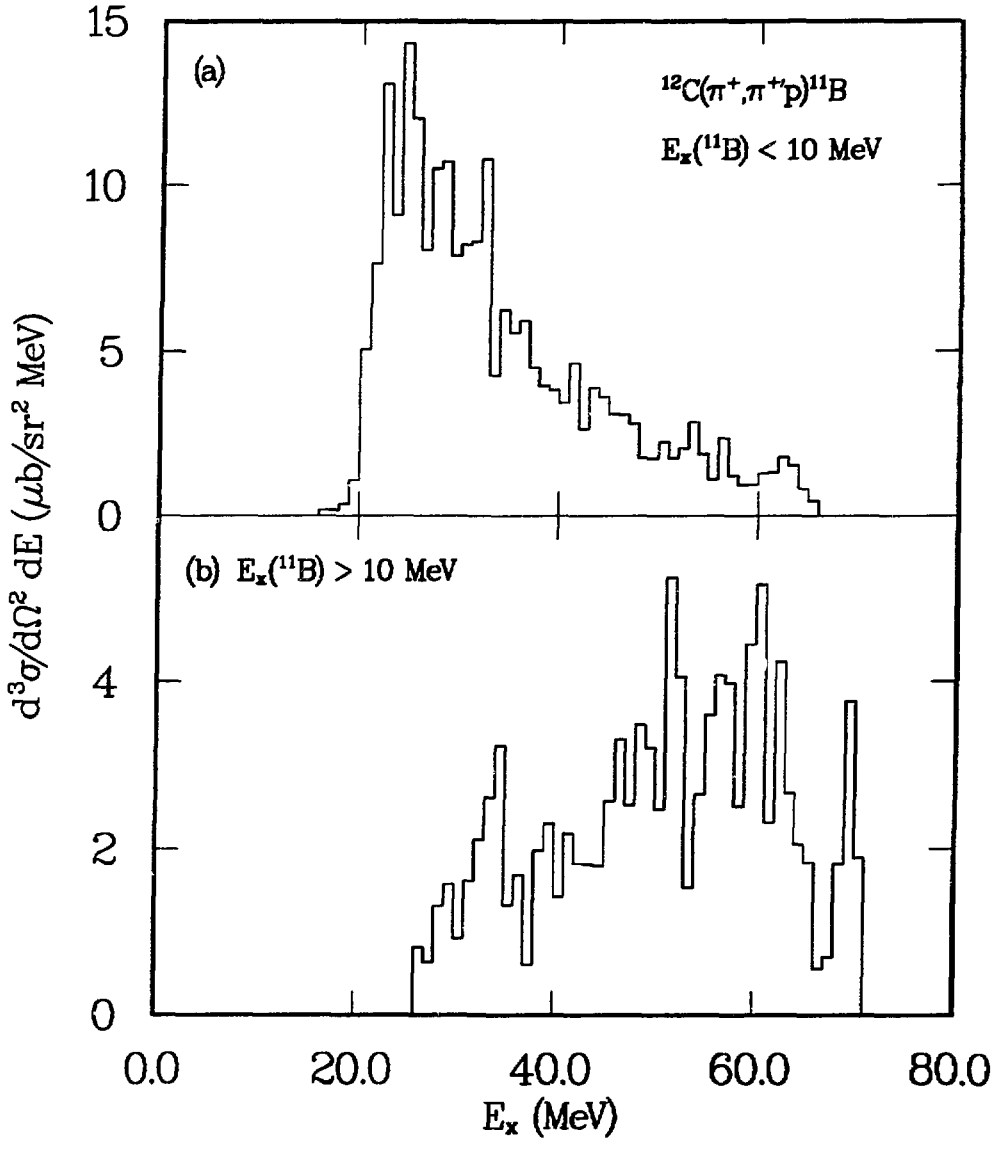

Fig. 3–13: $^{12}C(\pi^+,\pi^{+\prime}p)^{11}B$ reaction.

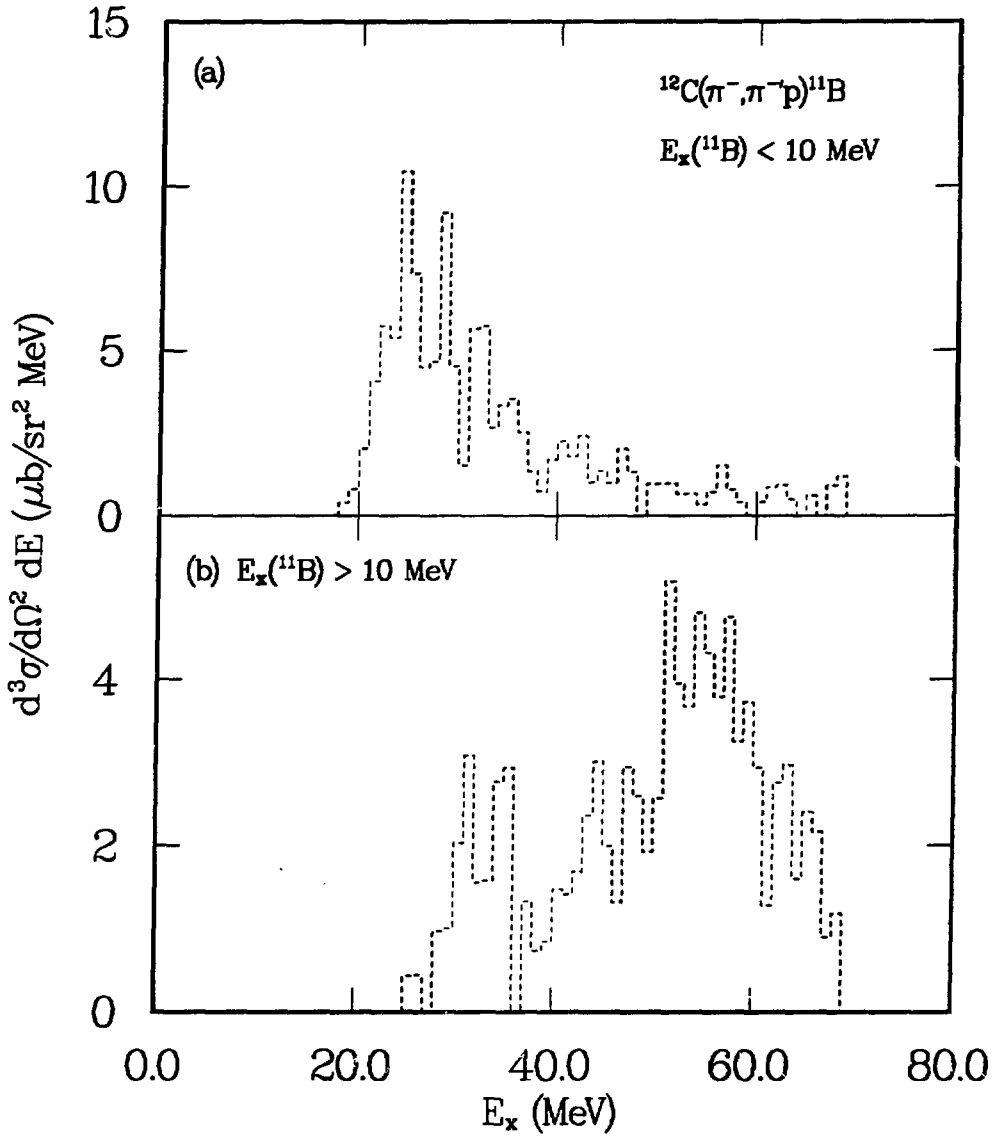

Fig. 3–14: $^{12}C(\pi^-,\pi^{-\prime}p)^{11}B$ reaction.

Excitation energy spectra of the residual ^{11}B nucleus from the reactions shown in Fig. 3–13 and –14 are presented in Fig. 3–15 and –16. Both pictures exhibit that a substantial number of events lead to the ground state of ^{11}B (with about a 2:1 dominance of π^+ over π^-), and a broad peak around 20 – 25 MeV (with about equal magnitude in π^+ and π^-). For comparison the ^{12}C($\pi^{\pm}, \pi^{\pm\prime}$p) data of Ziock et al. [Zi-79], measured at high excitation energies in ^{12}C and large pion scattering angle is shown in Fig. 3–17. Even though there is a small difference in the position of the broad peak, both the current data and the data of Ziock feature a similar shape for π^+. However, there is a striking difference between two data sets for π^-. This thesis data for π^- has strong enhancement in the ground state and lower stable states of ^{11}B, whereas the π^- data in the reference are *dramaticlly damped. The angular distributions of the emitted* protons provide valuable source of information on the excitation of the continuum of ^{12}C. These distributions will be presented with theoretical calculations in Chapter 4.

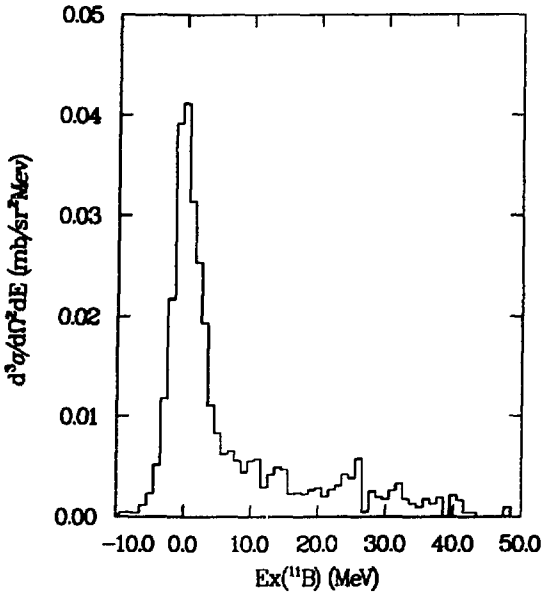

Fig. 3–15: Energy spectra as a function of $E_x(^{11}B)$ due to $^{12}C(\pi^+, \pi^{+\prime}p)$ reaction.

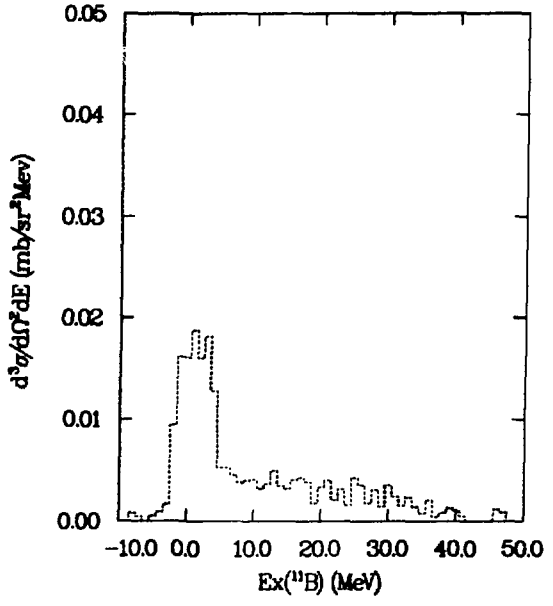

Fig. 3–16: Energy spectra as a function of $E_x(^{11}B)$ due to $^{12}C(\pi^-, \pi^{-\prime}p)$ reaction.

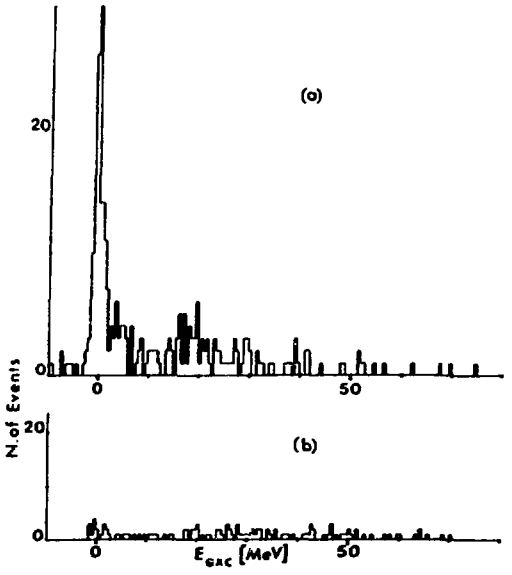

Fig. 3–17: Missing mass spectrum as a function of $E_x(^{11}B)$ gated by $E_x(^{12}C)$ from 59 to 109 MeV at $T_\pi = 180$ MeV, $\theta_\pi = -110°$, $\theta_p = 30°$ [Zi-79]. (Top) $^{12}C(\pi^+, \pi^{+\prime}p)$. (Bottom) $^{12}C(\pi^-, \pi^{-\prime}p)$.

3.3 Event Analysis of $^{208}Pb(\pi^\pm, \pi^{\pm\prime}N)$ reactions

(1) Proton Identification

The same method of the proton identification described in previous section was used. In addition, events corresponding to the excitation energies in ^{208}Pb less than 8 MeV, the proton separation energy, were discarded to clean up accidentals.

(2) Neutron Identification

From the assumption that neutral particles would not deposit much energy in the plastic scintillator because of its thiness (3 mm), a box ($-2 \leq$ E $\leq$ 100 MeV and $-1 \leq$ DE $\leq$ 3 MeV) was set up on the ΔE–E plot of Fig. 3–4 to identify neutrons. In addition to this box which eliminates charged particles that deposit energy in the thin plastic scintillator, events corresponding to the excitation energies in ^{208}Pb less than 7.4 MeV, the neutron separation energy, were also rejected. Events that passed these tests as well as the good pion event test were accumulated in a time of flight histogram, CTN, which is the flight time of the emitted particles from the target to the detector, corrected for the outgoing pion energy. Figure 3–18 shows the CTN histogram with the clearly visible neutron peak. The events in the blob ($-1 \leq$ E $\leq$ 2 MeV and $-1 \leq$ DE $\leq$ 3 MeV) shown in Fig. 3–4 were slow neutrons. Due to the very high Coulomb barrier in ^{208}Pb, protons with such low energies could not be detected. As seen in the CTN picture, there were many accidentals. To subtract the accidental background two time gates were used, one on the neutron peak ($100 \leq$ CTN $\leq$ 150) and the other in the background region ($-100 \leq$ CTN $\leq$ 100). The events found in $100 \leq$ CTN $\leq$ 150 after the subtraction were assumed to be neutrons.

An approximated neutron detection efficiency, $\epsilon_n \sim \frac{\sigma(\pi^-, \pi^{-\prime} n)}{\sigma(\pi^+, \pi^{+\prime} p)}$, was estimated by detecting both neutrons and protons from the ^{12}C target. The number of neutrons observed in $(\pi^-, \pi^{-\prime}\mathrm{n})$ was assumed to be equal to that of protons observed in $(\pi^+, \pi^{+\prime}\mathrm{p})$ because of charge symmetry. Both cross sections were summed over from 20 MeV to 40 MeV of the excitation energies of ^{12}C. The

average neutron detection efficiency was determined to be about 9.8% from this comparison.

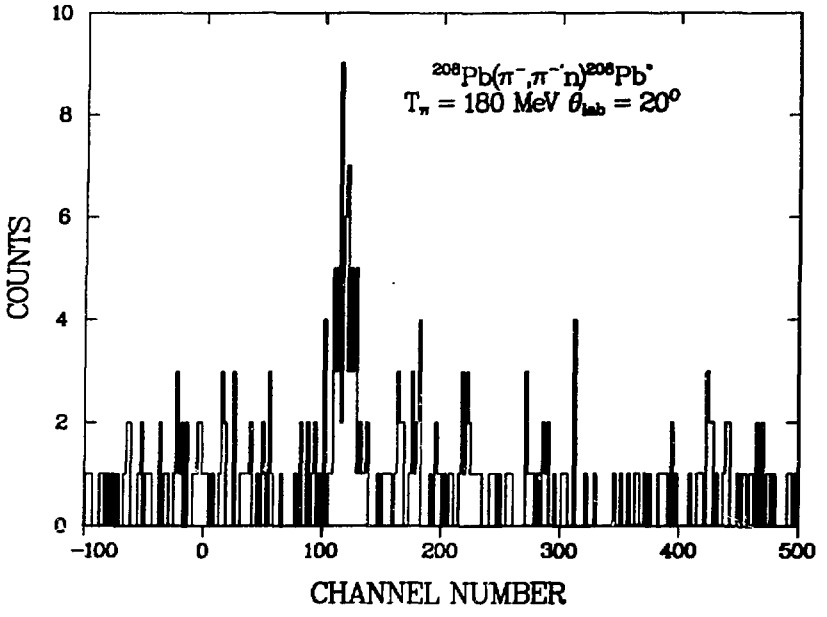

Fig. 3–18: CTN histrogram.

3.4 Results of ^{208}Pb($\pi^{\pm}$, $\pi^{\pm\prime}$N) reactions

Normalized singles spectra for π^+ and π^- scattering at T_π = 180 MeV and θ_{lab} = 20° are presented in Fig. 3–19a. The normalization was done in the same condition already described in section 3.1.4. Throughout the continuum region ($E_x(^{208}Pb) > 8$ MeV), the cross section ratio $r = \frac{\sigma(\pi^-)}{\sigma(\pi^+)}$ maintains approximately a constant value of near 2. This is true for both the GR and the background. The

difference in $\sigma(\pi^+)$ and $\sigma(\pi^-)$ is consistent with the previous results obtained at T_π = 162 MeV [Se-86].

In Fig. 3–19b and –19c, missing mass spectra (as a function of excitation energies in ^{208}Pb of ^{208}Pb($\pi^\pm, \pi^{\pm\prime}$n) and ^{208}Pb($\pi^\pm, \pi^{\pm\prime}$p) reactions), summed over all five detectors are shown. The neutron and proton penetrabilities in ^{208}Pb $\rightarrow$ ^{207}Pb + n and ^{208}Pb $\rightarrow$ ^{207}Tl + p for different values of the relative angular momentum ℓ are shown in figure 3–20 and 3–21. Since the neutron penetrabilities are so much larger than that of protons the neutron decay is the dominant decay channel of the GR in ^{208}Pb. Even above the Coulomb barrier ($E_x = E_{th} + E_{Coul} \geq 24$ MeV), the preponderance of neutron over proton decay is maintained due to the higher penetrability of neutrons. Angular distributions of neutrons for both the ($\pi^+, \pi^{+\prime}$n) and ($\pi^-, \pi^{-\prime}$n) reactions will be featured and discussed in chapter 4.

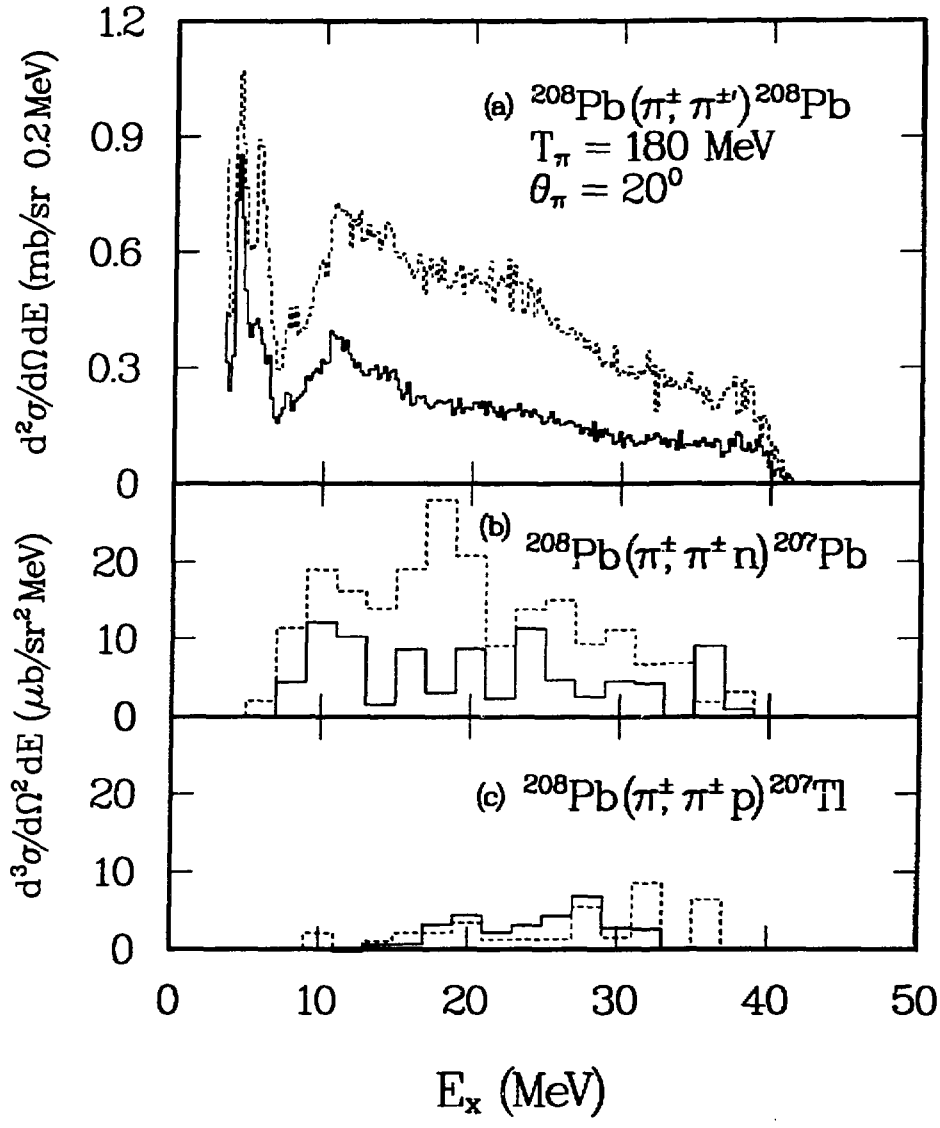

Fig. 3–19: Normalized singles spectra. (Top) $^{208}Pb(\pi^{\pm},\pi^{\pm\prime})$ reaction. (Middle) $^{208}Pb(\pi^{\pm},\pi^{\pm\prime}n)$ reaction. The correction for the neutron detection efficiency has not been made. (Bottom) $^{208}Pb(\pi^{\pm},\pi^{\pm\prime}p)$ reaction. Solid line is for π^+ and dashed for π^-.

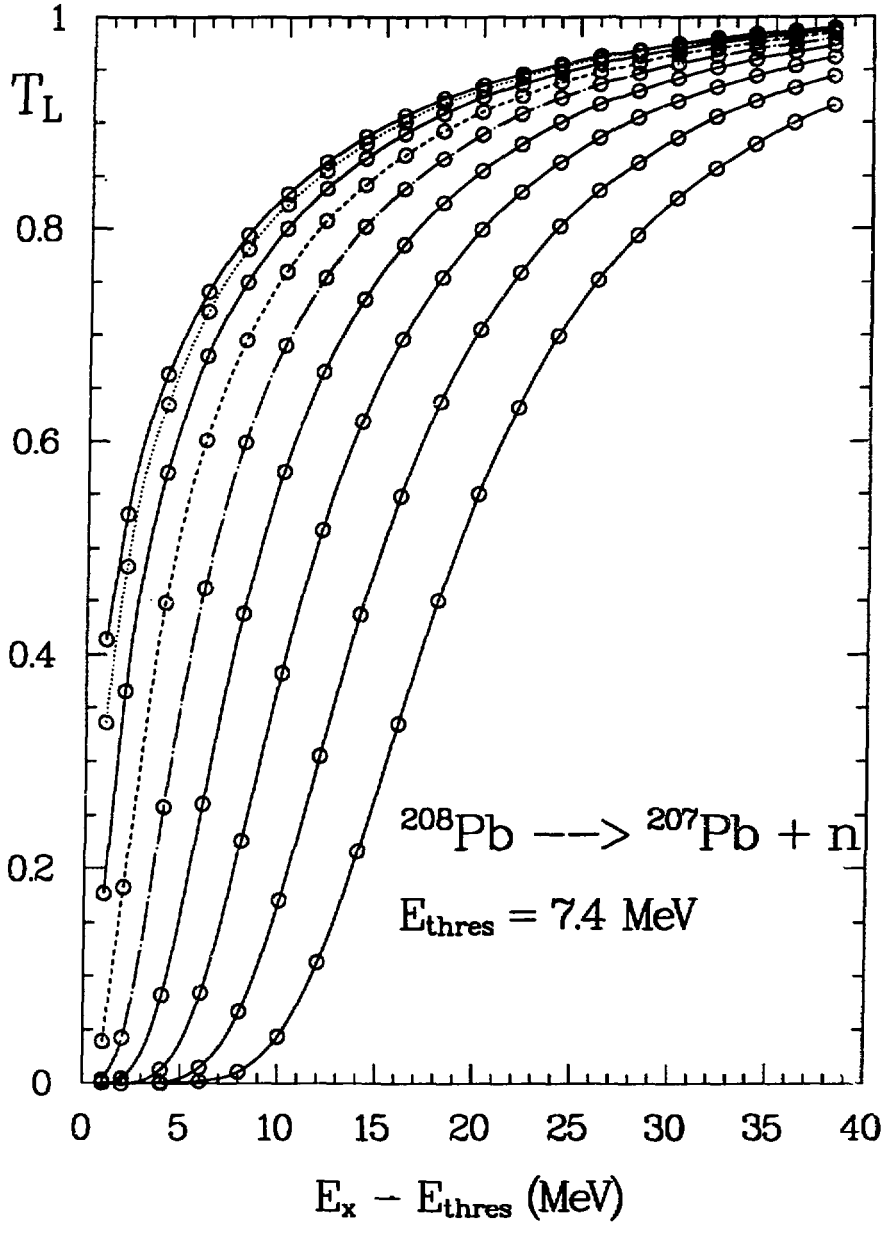

Fig. 3–20: Neutron penetrabilities in $^{208}Pb \rightarrow {}^{207}Pb$ + n reaction for different values of the relative angular momentum ℓ. From left to right $\Delta\ell = 0, 1, 2, 3, 4, 5, 6, 7, 8$ [Ye-88].

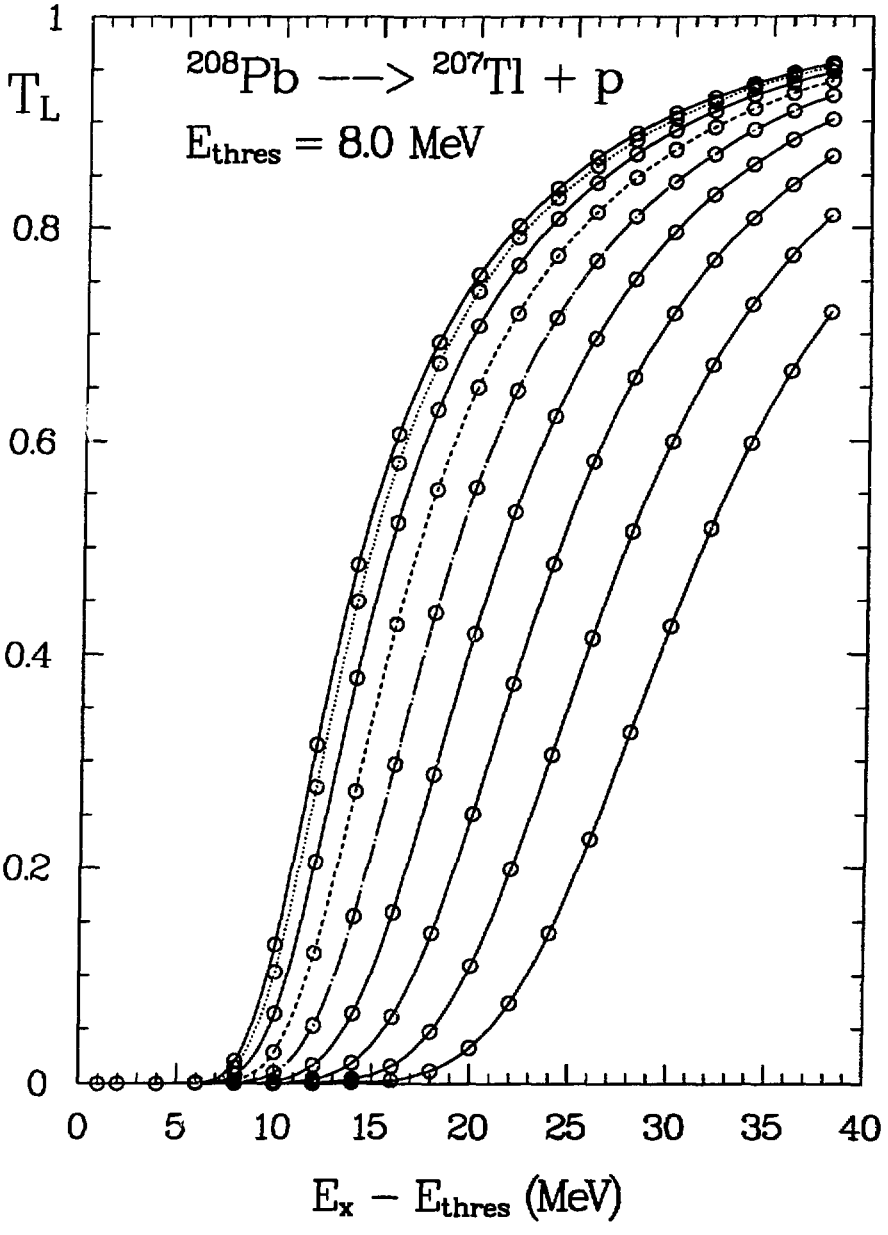

Fig. 3–21: Proton penetrabilities in $^{208}Pb \rightarrow {}^{207}Tl + p$ reaction for different values of the relative angular momentum ℓ. From left to right $\Delta\ell = 0, 1, 2, 3, 4, 5, 6, 7, 8$ [Ye-88].

Chapter 4. Theoretical Analysis of the Data

Basic scattering formulae are presented in section 4.1 in order to understand the following discussion of π–A (nucleus) scattering better. Then the formula for the pion-induced single nucleon knock-out reaction is described along with the presentation of the theoretical calculations for the $^{12}C(\pi^{\pm}, \pi^{\pm\prime}p)$ reactions in section 4.2, followed by the discussion of the $^{208}Pb(\pi^{\pm}, \pi^{\pm\prime}N)$ data in section 4.3. Finally, in section 4.4, inelastic scatterings to the GQR state in ^{208}Pb are studied using a macroscopic model.

4.1 Brief Survey of Basic Scattering Theory

Let's consider that an incoming projectile **a** collides with a target **A**, that is, **A(a,b)B** reaction, where the outgoing particle **b** may be **a** or a different particle and the residual nucleus **B** may be **A or A*** (an excited state) or a different nucleus. Assume that **a** and **A** interact through a fixed central potential $V(\vec{r})$. Then the time-independent Schrödinger equation $(\nabla^2 + K_\alpha^2)\Psi(\vec{r}) = V(\vec{r})\Psi(\vec{r}) \equiv F(\vec{r})$, can be solved asymptotically and the total wave function of the system can be expressed as:

$$\Psi_{aA\to aA'} \xrightarrow{r\to\infty} e^{i\vec{K}_\alpha\cdot\vec{r}} + \frac{e^{iK_\alpha r}}{r} f_\alpha(\theta,\phi) \quad \text{for elastic channel} \quad (K_\alpha = K_\beta, \text{on shell}) \tag{21}$$

and

$$\Psi_{aA\to bB} \xrightarrow{r\to\infty} \frac{e^{iK_\beta r}}{r} f_\beta(\theta,\phi) \quad \text{for non-elastic channel} \quad (K_\alpha \neq K_\beta, \text{off shell}) \tag{22}$$

where

$$\begin{aligned} f_\beta(\theta,\phi) &= -\frac{1}{4\pi}\int (e^{i\vec{K}_\beta\cdot\vec{r}'})^* V(\vec{r}\,')\psi(\vec{K}_\alpha,\vec{r}\,')d\vec{r}\,' \\ &= -\frac{1}{4\pi}\langle\phi_\beta|V(\vec{r}\,')|\psi_\alpha\rangle \\ &\equiv \frac{1}{4\pi}T_{BA}\ , \end{aligned} \tag{23}$$

and K_α (K_β) is the relative wave number for the entrance (exit) channel. This description is made in the center of mass system (CMS), and can be converted to the lab system using the invariance under change of frame [Ei-80]. The scattering amplitude, $f_\beta(\theta,\phi)$, is related to the differential cross section:

$$\frac{d\sigma_\beta}{d\Omega} = \frac{v_\beta}{v_\alpha}\,|f_\beta(\theta,\phi)|^2\ . \tag{24}$$

The factor $\frac{v_\beta}{v_\alpha}$ is there because the cross section is proportional to particle flux while the square of the scattering amplitude, $|f(\theta,\phi)|^2$, represents the particle density [Sa-80].

If the potential $V(\vec{r})$ is weak, we can assume that the scattering amplitude f is small. Then, the asymptotic total-wavefunction in Eq. (21) can be approximated by the plane wave, i.e. $\psi_\alpha \sim e^{i\vec{K}_\alpha\cdot\vec{r}}$. This is the famous Born Approximation. The scattering amplitude for the Born Approximation can be expressed as:

$$f_{Born}(\theta,\phi) = -\frac{1}{4\pi}\int e^{i\vec{q}_{CM}\cdot\vec{r}}V(\vec{r}\,')\,d\vec{r}\,' \tag{25}$$

where $\vec{q}_{CM} = \vec{K}_\alpha - \vec{K}_\beta$.

Assume further that $V(\vec{r}) = V_1(\vec{r}) + V_2(\vec{r})$. Then, a generalized solution for the time-independent Schrödinger equation [Me-62] can be written as:

$$\chi(\vec{K},\vec{r}) \overset{r\to\infty}{\longrightarrow} \chi_1^{(+)}(\vec{K},\vec{r}) + \frac{e^{iKr}}{r}f_2(\theta,\phi) \tag{26}$$

where

$$\chi_1^{(+)}(\vec{K},\vec{r}) \overset{r\to\infty}{\longrightarrow} e^{i\vec{K}\cdot\vec{r}} + \frac{e^{iKr}}{r} f_1(\theta,\phi) \tag{27}$$

$$f_1(\theta,\phi) = -\frac{1}{4\pi}\int (e^{i\vec{K}'\cdot\vec{r}'})^* V_1(\vec{r}\,')\chi(\vec{K},\vec{r}\,')d\vec{r}\,' \tag{28}$$

$$f_2(\theta,\phi) = -\frac{1}{4\pi}\int \chi_1^{(-)}(\vec{K}',\vec{r}')^* V_2(\vec{r}\,')\chi(\vec{K},\vec{r}\,')d\vec{r}\,' . \tag{29}$$

Superscript $(+/-)$ denotes an outgoing and an ingoing scattered wave, respectively. Subscript 1 is for the potential V_1 and 2 is for V_2. Eq. (26) must be approximated because it contains the exact solution χ. If we assume $V_1(\vec{r}) \gg V_2(\vec{r})$, we can replace χ with the solution $\chi^{(+)}$ for the potential V_1. This is a more sophiscated version of the Born Approximation called the distorted-wave Born approximation (DWBA). This approximation bears 'Born' because it is first order in V_2. It is also 'distorted-wave' because the distorted wave χ_1 is used in Eq. (29) instead of the plane wave as in Eq. (28) [Sa-80]. The potential V_1 describes the elastic scattering whereas V_2 is the potential that causes the non-elastic transition. Thus, the DWBA is good only when elastic scattering is the most dominant reaction channel. In the DWBA approximation the scattering amplitude for a reaction **A(a,b)B** is expressed as

$$F_{DWBA}(\theta,\phi) = f_\alpha(\theta,\phi) - \frac{1}{4\pi}\int \chi_\beta^{(-)}(\vec{K}_\beta,\vec{r}_\beta)\,\langle b,B|V_2(\vec{r})|a,A\rangle\,\chi_\alpha^{(+)}(\vec{K}_\alpha,\vec{r}_\alpha)d\vec{r}_\alpha d\vec{r}_\beta . \tag{30}$$

A partial wave expansion is a useful way of expressing the total wave Ψ in the case of a central potential. That is $\Psi = \sum_{\ell,m} C_{\ell,m} U_\ell(r) Y_{\ell,m}(\theta,\phi)$, where $C_{\ell,m}$ is the Clebsh-Gordan coefficient, $U_\ell(r)$ is the radial part of the wavefunction and $Y_{\ell,m}$ is the angular part. The partial wave expansion is specially useful when ℓ

$\leq \ell_{max} = K_\alpha R$ is a small value where R is the radius of the nucleus. The plain wave of Eq. (21) can be written as

$$\begin{aligned}(e^{i\vec{K_\alpha}\cdot\vec{r}}) &= (e^{iK_\alpha r\cos\theta}) \\ &= \sum_{\ell=0}^{\infty}(2\ell+1)\, i^\ell\, j_\ell(K_\alpha r)\, P_\ell(\cos\theta) \\ &\xrightarrow{K_\alpha r \gg 1} \sum_{\ell=0}^{\infty}(2\ell+1)\, i^\ell\, \frac{\sin(K_\alpha r - \frac{\ell\pi}{2})}{K_\alpha r}\, P_\ell(\cos\theta).\end{aligned} \tag{31}$$

The partial wave expressions for the scattering amplitude are asymptotically

$$f(\theta,\phi) = \frac{1}{2iK_\alpha}\left(\frac{v_\alpha}{v_\beta}\right)^{1/2}\sum_\ell (2\ell+1)\,[\eta_\ell e^{2i\delta_\ell}-1]\,P_\ell(\cos\theta) \tag{32}$$

(for non-elastic channel and $\eta_\ell < 1$)

$$= \frac{1}{K_\alpha}\sum_\ell (2\ell+1)\, e^{2i\delta_\ell}\, \sin\delta_\ell\, P_\ell(\cos\theta) \tag{33}$$

(for elastic channel)

where δ_ℓ is the phase shift and positive real number. Eq. (32) and (33) hold only if the reaction is spin independent. From Eq. (24) the differential cross section for each case is:

$$\begin{aligned}\left(\frac{d\sigma}{d\Omega}\right)_{elastic} &= |f(\theta,\phi)|^2_{elastic} \\ &= \frac{4\pi}{K_\alpha^2}\sum_\ell (2\ell+1)\sin^2\delta_\ell\end{aligned} \tag{34}$$

and

$$\begin{aligned}\left(\frac{d\sigma}{d\Omega}\right)_{non-el} &= \frac{v_\beta}{v_\alpha}|f(\theta,\phi)|^2_{non-el} \\ &= \frac{\pi}{K_\alpha^2}\sum_\ell (2\ell+1)\,|\eta_\ell e^{2i\delta_\ell}-1|^2\,.\end{aligned} \tag{35}$$

For a general case, that is, when potential is not central, we can express the total wave in terms of the Green function (operator), G. The Green operator

G is obtained from

$$H_{tot}\Psi = E\Psi$$

where

$$\begin{aligned} H_{tot} &= H + V_\alpha = H_a + H_A - \frac{\hbar^2}{2\mu_\alpha}\nabla_\alpha^2 + V_\alpha \ , \\ H &\equiv \text{Hamiltonian for the internal states of the} \\ &\quad \text{two colliding nuclei } \mathbf{a} + \mathbf{A} \text{ with their} \\ &\quad \text{relative kinetic energy.} \\ V_\alpha &\equiv \text{the interaction between } \mathbf{a} \text{ and } \mathbf{A}. \end{aligned}$$

That is,

$$(E - H)\Psi = V_\alpha\Psi$$

Then,

$$\begin{aligned} \Psi &= \lim_{\epsilon\to 0} \frac{1}{E - H + i\epsilon} V_\alpha \Psi \\ &= GV_\alpha\Psi \ . \end{aligned}$$

$i\epsilon$ ($\epsilon > 0$) is introduced to avoid the singularity where E = H. Now, the total wave function can be generated by the expansion of the Green's operator:

$$\Psi = \phi_\alpha + GV_\alpha\Psi + GV_\alpha GV_\alpha\Psi + \cdots \ .$$

4.1.1 Optical Potential and Mean Free Path

Before we discuss the π-nucleus interaction, it is helpful to review the relationship between the optical potential and the mean free path, and the definition of the impulse approximation.

The optical potential, the term from the optics, is a complex potential whose imaginary part is related to the mean free path of an incident particle inside a material. In an analogous way to the optics, the optical potential can be used in studying the medium-energy pion-nucleus scattering. Following the description given in Eisenberg and Koltun [Ei-80], a generalized form of the π-nucleus optical potential can be deduced. Let's suppose a plane wave of propagation vector $\vec{K}$ in vacuum incident on a semi-infinite medium of scatters as shown in Fig. 4–1.

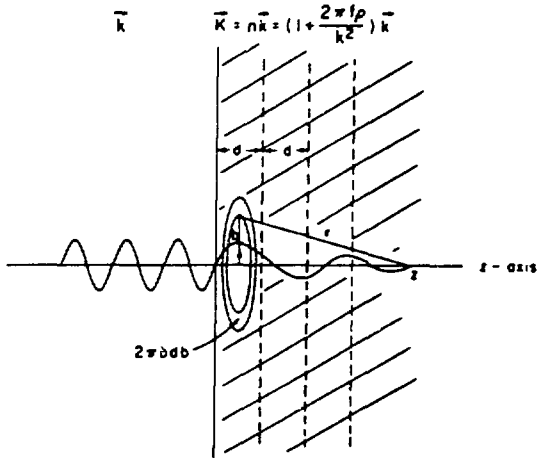

Fig. 4–1: The propagation of a wave with external momentum $\vec{K} \parallel \vec{z}$ in a semi infinite medium of density $\rho(\vec{r})$ and scattering amplitudes f [Ei-80].

Further, assume

(1) uniform density of the medium, $\rho(\vec{r})$,

(2) energy-independent forward scattering amplitude f

(3) very small attenuation, that is, $\psi_{external} \sim \psi_{inside}$,

(4) f and ρ not varying over the slab thickness.

The wave at position z will be the original plane wave plus the contributions of the scattered wave from each scattering center up to z as in Eq. (21):

$$\psi(z) = e^{iKz} + \int_0^\infty f\frac{e^{iKr}}{r}\rho d2\pi b\, db \tag{36}$$

where $\vec{b}$ is impact parameter and $\vec{r}^{\,2} = \vec{b}^{\,2} + z^2$. Since we assumed $\psi_{external} \sim \psi_{inside}$, we need a factor, $e^{-\xi r}$, to damp the contributions of the scattered waves. Using bdb = rdr,

$$\begin{aligned} \psi(z) &= e^{iKz} + 2\pi f\rho d\int_z^\infty e^{iKr-\xi r}\, dr \\ &\xrightarrow{\xi\to 0} e^{iKz}\left(1 + i\frac{2\pi f\rho d}{K}\right) . \end{aligned} \tag{37}$$

If the scattering from each slab (N slabs in the medium) is independent, the Poission distribution gives,

$$\begin{aligned} \psi(z) &= \lim_{N\to\infty} e^{iKz}\left(1 + i\frac{2\pi f\rho z}{KN}\right)^N \\ &= \exp\left[iK\left(1 + \frac{2\pi f\rho}{K^2}\right)z\right] \\ &= e^{inKz} \end{aligned} \tag{38}$$

for $z = Nd$. Here $n = 1 + \frac{2\pi f\rho}{K^2}$ and is called index of refraction. In actual situation that is not in vacuum, we have attenuation of the beam in the forward propagation direction ($\theta = 0°$), that is,

$$\begin{aligned} n &= 1 + \frac{2\pi\rho}{K^2}\,[Ref + i\ Imf] \\ &= Ren + i\,\frac{2\pi\rho}{K^2} Imf\ . \end{aligned}$$

From the optical theorem,

$$Imf = \frac{K\sigma_{tot}}{4\pi}\ .$$

Then,

$$\psi(z) = e^{i(Ren)Kz} \exp\left(-\rho\sigma_{tot}\frac{z}{2}\right)$$

and

$$|\psi(z)|^2 = \exp(-\rho\sigma_{tot}z) = e^{-z/l}$$

where l is the mean free path, the average distance traveled between successive collisions, of the projectile in the medium and defined as

$$l = \frac{1}{\rho\sigma_{total}}\ . \tag{39}$$

Now suppose $\psi(z) = \exp\left[iK\left(1 + \frac{2\pi f\rho}{K^2}\right)z\right]$ in Eq. (38) is the solution of the Schrödinger equation,

$$\left[-\frac{1}{2m}\nabla^2 + V\right]\psi(z) = \frac{K^2}{2m}\psi(z)\ , \tag{40}$$

which has the potential V (with $\hbar \equiv 1$). Solving the equation yields

$$V = -\frac{1}{2m}\left(4\pi f\rho + \frac{4\pi^2 f^2\rho^2}{K^2}\right)\ . \tag{41}$$

If the effect of the medium is small, i.e., ρf is small, then,

$$\begin{aligned} V &\sim -\frac{2\pi}{m}\rho f \\ &= -\frac{2\pi}{m}\rho\,[Ref + iImf]\,. \end{aligned} \tag{42}$$

Thus, the potential is complex and called optical potential. The models that use complex potentials (optical potentials) are called optical models. The key point about the optical potential is that it relates the potential for π-nucleus scattering to the fundamental π-nucleon scattering amplitude [Ei-76]. For a nucleus, averaging over protons and neutrons, the pion-nucleus optical potential becomes

$$V = -\frac{2\pi}{m}\,[\rho_n f_{\pi n} + \rho_p f_{\pi p}]\,. \tag{43}$$

4.1.2 Impulse Approximation

The impulse approximation is a single scattering approximation. The interaction between the incident π and the target nucleus can be expressed as the sum of two-body interactions, $V = \sum_i v_i$, between the pion and each target nucleon i. The conditions [Sa-80] for validity of the impulse approximation are:

1. the incident π bombarding energy is greater than binding energies of the struck nucleons, so that binding effects can be neglected;
2. the collision time τ must be smaller than the period of the bound target nucleon, i.e., $\omega\tau \ll 1$;

   So if $s \equiv$ range of the nuclear force ($\sim$ 2 fm)

   $v \equiv$ the projectile velocity

$B \equiv$ the binding energy of the bound nucleon,

then,

$$\omega\tau = \frac{B}{\hbar}\frac{s}{v} \ll 1 ;$$

3. for the validity of the single scattering approximation, the mean free path l of the incident pion inside the nucleus must be larger than the nuclear radius, $l > R$, that is, from Eq. (39), $R\rho\sigma_{tot} < 1$.

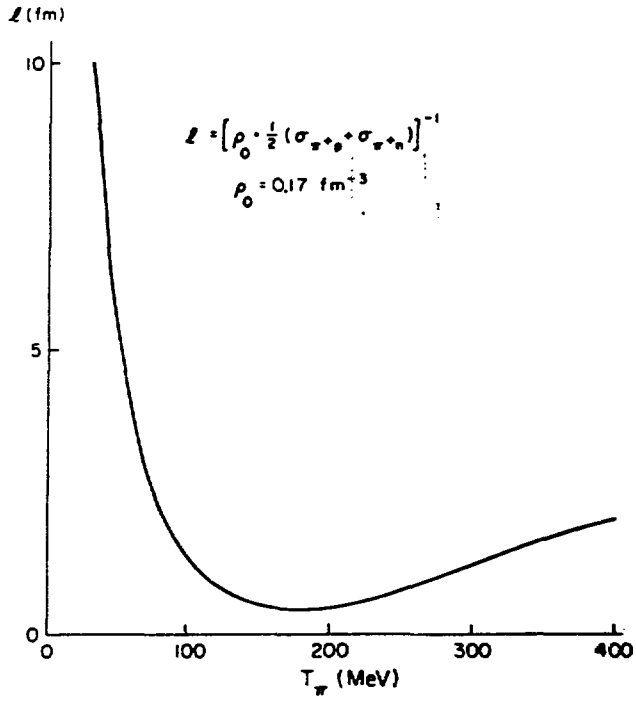

Fig. 4–2: The mean free path l for $\pi^{\pm}$ in a self-conjugate nucleus [Ei-80].

Even if the first two conditions are met, there are chances that the condition for the single scattering approximation is not satisfied. In Fig. 4–2 the mean free path of the incident pion inside nucleus is plotted as a function of the kinetic energy of the incident pion. It is clear that the pion mean free path near the $\Delta_{3,3}$ resonance is shorter than the nuclear radius even for light nuclei ($\langle R \rangle_{^{12}C} \sim 2.7$ fm). Thus, once a pion with the kinetic energy near 180 MeV penetrates inside the target nucleus, it has strong possiblity to go through multiple scatterings. However, since pion-nucleus interaction normally occurs near surface of the nucleus [Ko-85, Oa-89], the impulse approximation still holds near the $\Delta_{3,3}$ region.

4.2 Theoretical Analysis of $^{12}C(\pi^{\pm}, \pi^{\pm\prime}p)^{11}B$ Data

4.2.1 DWIA Formula for π-induced Knock-out Reaction

The Feynman diagrams in Fig. 4–3 present two possible components that the upper picture is quasi-free knock-out and the lower picture is nucleon emission after excitation of a resonance state. One way of describing the pion-induced single nucleon knock-out interactions is through the use of a formula derived by Chant and Roos [Ch-77, Re-82], which produces good agreement with the exclusive coincidence data taken at high E_x(target) and back angles as already described in section 1.4. According to them, the triple differential cross section for the reaction A$(\pi, \pi'$ N)B resulting from the knock-out of a bound nucleon with quantum numbers (n, ℓ, j) leading to a specific final state in nucleus B can be expressed as

$$\frac{\mathrm{d}^3\sigma^{\ell j}}{\mathrm{d}\Omega_{\pi'}\mathrm{d}\Omega_N\mathrm{d}E_{\pi'}} = \frac{2\pi}{\hbar v_\pi}\,\omega_B\,C^2\,S_{\ell j}\,|\langle\bar{t}\rangle|^2\sum_{\Lambda}|T_{BA}^{\alpha\ell\Lambda}|^2\,, \qquad (44)$$

Fig. 4–3: (Top) $(\pi, \pi' \mathrm{N})$ reaction due to knock-out process. (Bottom) $(\pi, \pi' \mathrm{N})$ reaction due to inelastic scattering to a resonance state.

neglecting spin-orbit terms in the emitted nucleon-core potential. v_π is the relative velocity of the incident pion and the target nucleus, ω_B is the energy density of final states, C^2 is an isospin Clebsh-Gordan coefficient, and $S_{\ell j}$ is the single nucleon spectroscopic factor coming from the overlap of the initial and final nuclear states. (Note $C^2S_{\ell j}$ here is Cohen and Kurath's spectroscopic factor [Co-67]). $|\langle\bar{t}\rangle|^2$ is the half-off-the-energy shell π–N scattering matrix (t matrix). This t matrix is summed and averaged over the initial and final nucleon spins evaluated for the asymptotic momenta. $T_{BA}^{\alpha\ell\Lambda}$ is a distorted-wave matrix element that can be written as

$$T_{BA}^{\alpha\ell\Lambda} = \frac{1}{\sqrt{2\ell+1}} \int \chi_{\pi' B}^{(-)^*}(\vec{K}_{\pi' B}, \vec{r}) \chi_{NB}^{(-)^*}(\vec{K}_{NB}, \vec{r}) \chi_{\pi A}^{(+)}(\vec{K}_{\pi A}, \gamma\vec{r}) \phi_{n\ell\lambda}^{\alpha}(\vec{r})\, \mathrm{d}^3 r \ . \quad (45)$$

χs are the distorted waves for the incoming pion due to the target ($\chi_{\pi A}$), outgoing pion due to the residual nucleus ($\chi_{\pi' B}$), and knock-out nucleon due to the residual nucleus (χ_{NB}), respectively. $\vec{K}_{\pi A}$, $\vec{K}_{NB}$, $\vec{K}_{\pi' B}$, are the relative momenta that can be formulated as

$$\begin{aligned} \vec{K}_{\pi A} &= \frac{M_A}{M_A + m_\pi} \vec{K}_\pi \\ \vec{K}_{\pi' B} &= \vec{K}_{\pi'} - \frac{m_\pi}{m_\pi + m_N + M_B} \vec{K}_\pi \ , \end{aligned}$$

and,

$$\vec{K}_{NB} = \vec{K}_N - \frac{m_N}{m_\pi + m_N + M_B} \vec{K}_\pi$$

where $\vec{K}_\pi$, $\vec{K}_{\pi'}$, $\vec{K}_N$ and $\vec{K}_B$ are the momenta in the lab system. These momenta are generated relativistically in THREEDEE calculations. γ is defined as $\gamma = \frac{M_B}{M_A}$, and $\phi_{n\ell\lambda}^{\alpha}$ is the bound single nucleon wave function with principal quantum

number n, orbital angular momentum ℓ, and z component of orbital angular momentum λ.

The factorized DWIA formula Eq. (44) can be written fully relativistically with the density of states expressed in detail as,

$$\begin{aligned}\frac{d^3\sigma^{\ell j}}{d\Omega_{\pi'}d\Omega_N dE_{\pi'}} &= C^2\, S_{\ell j} \sum_{\lambda} |T_{BA}^{\alpha\ell\Lambda}|^2 \left\{ \frac{E_\pi E_{\pi'} E_N}{(2\pi)^5(\hbar c)^6} \frac{\vec{K}_{\pi'}\vec{K}_N\, c}{\vec{K}_\pi} \right. \\ &\left. \times \frac{1}{1+\left[\frac{E_N}{E_B}\right]\left[1-\frac{\vec{K}_\pi}{\vec{K}_N}\cos\theta_N + \frac{\vec{K}_{\pi'}}{\vec{K}_N}\cos(\theta_{\pi'}+\theta_N)\right]} \right\} \\ &= C^2\, S_{\ell j}\, K \left[\frac{\mathrm{d}\sigma}{\mathrm{d}\Omega}\right]_{\pi+N} \sum_{\lambda} |T_{BA}^{\alpha\ell\Lambda}|^2 \,, \end{aligned} \tag{46}$$

where K is the kinematic factors necessary to convert $|\langle\bar{t}\rangle|^2$ to $\left[\frac{\mathrm{d}\sigma}{\mathrm{d}\Omega}\right]_{\pi+N}$, the two-body π–N half-shell cross section.

The following is a summary of approximations made by the authors in formulating Eq. (46) for the factorized DWIA knock-out process:

(1) the impulse approximation is made in replacing the exact operator t_{BA} by the two-body free π + N scattering t matrix.

(2) it is also assumed that the t matrix varies slowly enough that its arguments may be replaced by their asymptotic values.

(3) a non-static approximation is made to decouple the wave equation for the exciting particles.

(4) the assumptions (2) and (3) make the factorization possible so that the matrix elements of t may be taken outside the integration in

T_{BA}.

(5) in evaluating the $|\langle\bar{t}\rangle|^2$, the fact that the struck N is off the mass shell is neglected. Rather, a nearby on-shell point using an interpolation of available differential cross sections for free π + N elastic scattering is adopted.

4.2.2 DWIA Calculations (THREEDEE)

(1) Generating the Pion Distorted Waves

In order to generate proper pion distorted waves in Eq. (45), a comparison of experimental [Mo-88] and calculated angular distributions for π-^{12}C elastic scattering cross-sections was made. The calculation of the pion distorted waves was performed using the pion optical model code DAMIT [Hu-73], a subroutine of the code THREEDEE. The code DAMIT solves a modified Klein-Gordon equation [Au-67],

$$(-\nabla^2+\mu^2)\chi_\pi = (E_\pi^2 - E_\pi V_{C\pi} - U_\pi)\chi_\pi \ , \tag{47}$$

which contains a Kisslinger type optical potential [Ki-55],

$$U_\pi = -Ab_0P_\pi^2\rho(r) + Ab_1\vec{\nabla}\cdot(\rho(r)\vec{\nabla}) \ , \tag{48}$$

where

$V_{C\pi}$ $\equiv$ the Coulomb potential

$\mu \equiv \frac{m_\pi c}{\hbar}$

A $\equiv$ the number of target nucleons

b_0 = the complex s-wave coefficient

b_1 = the complex p-wave coefficient

$\rho(r)$ = the ground state matter density

P_π = the pion momentum in the pion-nucleus center of mass

E_π = the pion energy in the pion-nucleus center of mass.

For self-conjugate nuclei, the optical potential for π^- is the same as for π^+.

The optical model complex parameters, b_0 and b_1 for a π^+ and a nucleus (A,Z), are evaluated from the π–nucleon phase shift [Ro-78], using the formulae,

$$b_0 = \frac{4\pi\zeta}{P_\pi^3}\frac{1}{A}\left[(A-Z)\frac{2\alpha_{11}^0+\alpha_{31}^0}{3}+Z\alpha_{31}^0\right] \tag{49}$$

and

$$b_1 = \frac{4\pi\zeta}{P_\pi^3}\frac{1}{A}\left[(A-Z)\frac{2\alpha_{33}^1+\alpha_{31}^1+4\alpha_{13}^1+2\alpha_{11}^1}{3}+Z(2\alpha_{33}^1+\alpha_{31}^1)\right] \tag{50}$$

where

ζ = a transformation factor from the pion-nucleon center of mass to the pion-nucleus center of mass [Co-80]
= $(\epsilon_\pi^*\epsilon_N^*/\epsilon_\pi\epsilon_N)$

ϵ_π, ϵ_N the pion and nucleon energies in the pion-nucleus center of mass system.

ϵ_π^*, ϵ_N^* the pion and nucleon energies in the pion-nucleon center of mass system

$\alpha_{2T,2J}^L = e^{i\delta_{2J,2T}^L}\sin\delta_{2J,2T}^L$.

For π^- scattering, the factors Z and (A−Z) are interchanged. The parameters, b_0 and b_1, were taken from the analysis of Cottingame and Holtkamp [Co-80] for the incident pion energy, T_π = 180 MeV. The values used are:

Re b_0	Im b_0	Re b_1	Im b_1
−0.6096	0.3126	4.3055	7.6200 .

For incident energies near the $\Delta_{3,3}$ resonance the Cottingame-Holtkamp method, which utilizes free π–nucleon parameters obtained from an energy $\sim$ 30 MeV lower than the incident pion energy, improves the agreement between the calculation and $\pi^{\pm}$–elastic scattering data for nuclei from ^{9}Be to ^{208}Pb.

A modified harmonic oscillator density distribution was chosen for the ground state matter density $\rho(r)$,

$$\rho(r) = \rho_0 \left[1 + c\left(\frac{r}{a}\right)\right] \exp\left[-\left(\frac{r}{a}\right)^2\right] \tag{51}$$

with

$$\rho_0 = \frac{1}{\left(1 + \frac{3}{2}c\right)(\sqrt{\pi}a)^3} .$$

Often the parameters, a and c, are taken from electron-scattering measurement [Ja-74, Si-70]. However, electron-scattering measures the charge density distribution $\rho_{ch}(r)$, not the ground state matter density $\rho(r)$. Because of the finite charge size of the nucleons $\rho(r)$ is not equal to $\rho_{ch}(r)$. A correction must therefore be made to obtain a point density distribution in which

$$\left\langle r^2_{point} \right\rangle = \left\langle r^2_{ch} \right\rangle - \left\langle r^2_N \right\rangle .$$

Using the values of $\left\langle r^2_p \right\rangle$ and $\langle r^2_{ch} \rangle$ of the target nucleus, taken from the electron scattering data, we can get $\left\langle r^2_{point} \right\rangle$. Then, assuming $\left\langle r^2_p \right\rangle = \frac{4\pi}{Ze} \int \rho(r) r^4 dr$, parameters a and c are varied until the $\left\langle r^2_{point} \right\rangle$ value is reproduced. This method

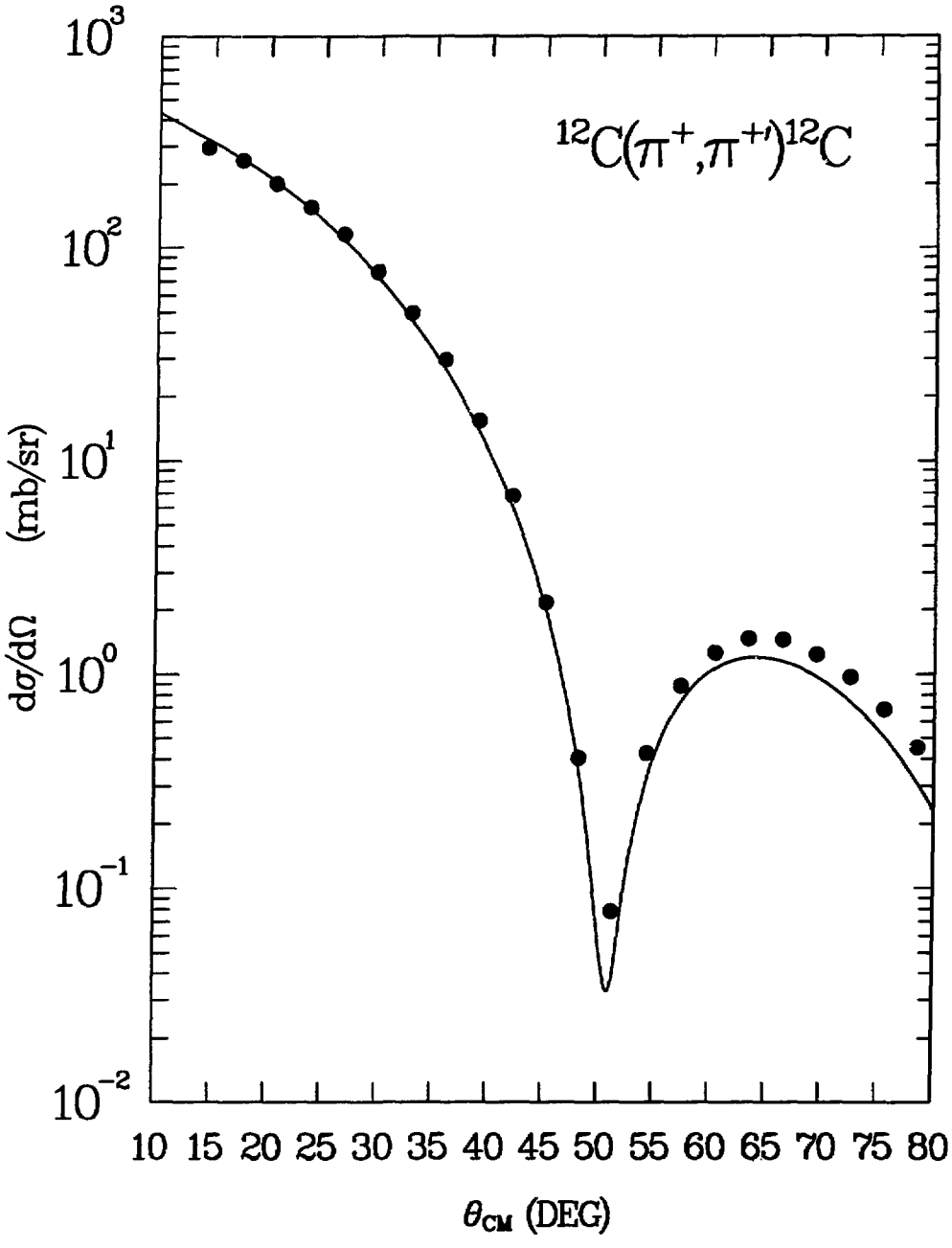

Fig. 4–4a: Points are data from π^+–^{12}C elastic scatterring at T_π = 180 MeV. Curve is the fit from THREEDEE using the parameters cited in text.

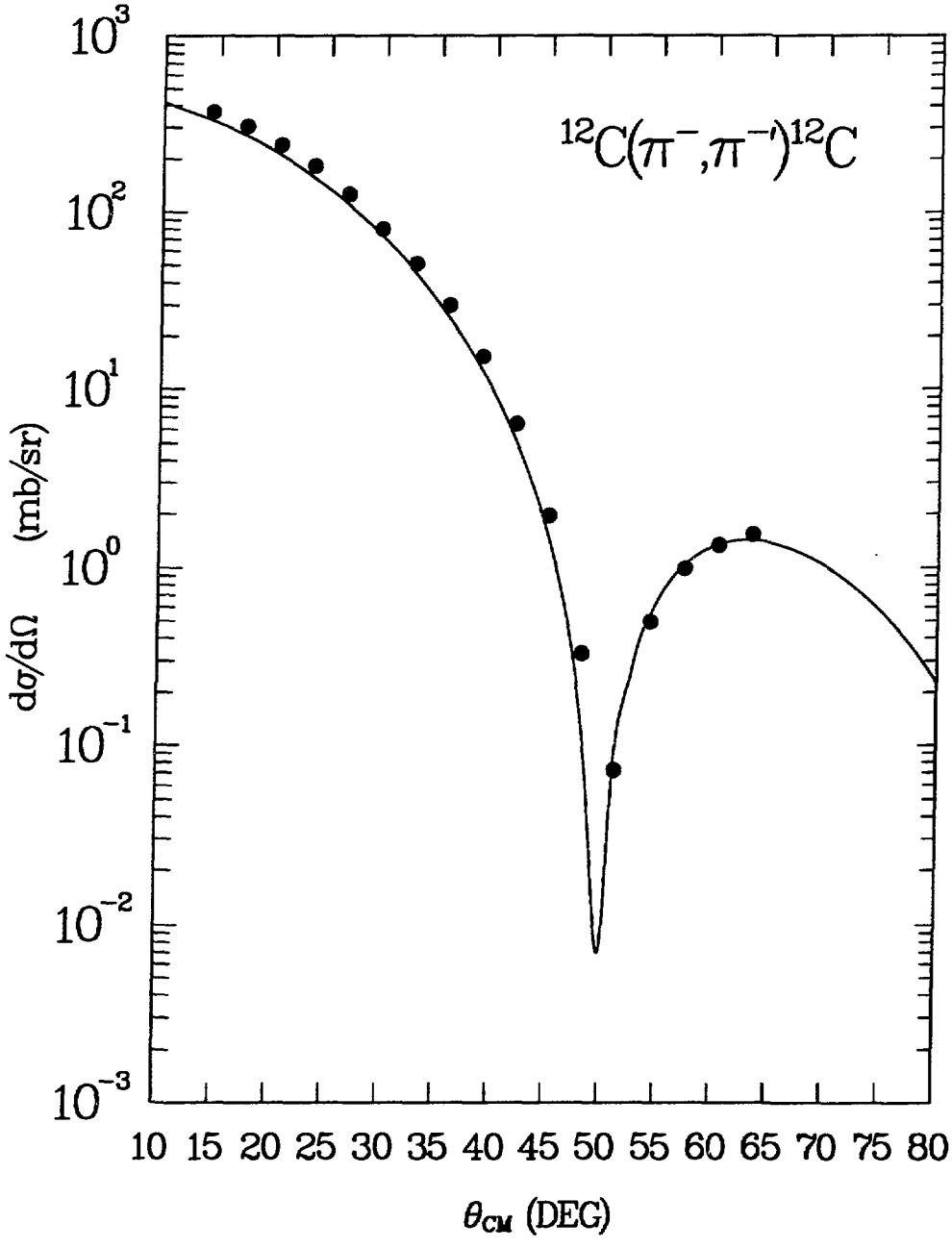

Fig. 4–4b: Points are data from π^-–^{12}C elastic scatterring at T_π = 180 MeV. Curve is the fit from THREEDEE using the parameters cited in text.

approximates a ground state point-density distribution consistent with the on-shell approximation [Co-87] used here. For the calculation of $\pi^{\pm}$ + ^{12}C elastic scattering, the point neutron, $\rho_n(r)$, and the point proton, $\rho_p(r)$, densities are assumed to be equal because of ^{12}C being a self-conjugate nucleus. The best fit of the calculation to the $\pi^{\pm}$–^{12}C elastic scattering was achieved by using the values of a = 1.514 fm and c = 1.674 taken from the work of Cottingame et al. [Co-87]. The results are shown in Fig. 4–4.

(2) The Emitted Proton Distorted Wave

The outgoing proton distorted wave was calculated using an optical potential,

$$\begin{aligned} U_p(r) &= -\frac{V}{1+\exp\left[(r-r_0A^{1/3})a^{-1}\right]} \\ &\quad - i\left(W - 4W_D\, a'\frac{d}{dr}\right)\frac{1}{1+\exp\left[(r-r_0'A^{1/3})a'^{-1}\right]} \\ &\quad + V_{Cp}\,, \end{aligned} \tag{52}$$

in a Schrödinger equation modified for relativistic effects [Na-81]. The proton optical model parameters from the analysis of proton elastic scattering by Nadasen et al. [Na-81] were used and they are:

$$\begin{aligned} r_0 &= 1.33fm \\ a &= 0.65fm \\ r_c &= 1.33fm \\ r_0' &= 1.46fm \\ a' &= 0.44fm \\ W_D &= 0 \text{ [Ch-77].} \end{aligned}$$

(3) The Proton Bound-State Wave Function

The bound single proton wave function, $\phi_{n\ell\lambda}(\vec{r})$, was obtained by solving the Schrödinger equation for a bound proton in a Woods-Saxson potential,

$$\begin{aligned} U_{bp}(\vec{r}) \;=\; & -\frac{V_c}{1+\exp\left[(r-r_0(A-1)^{1/3})a^{-1}\right]} \\ & -\left(\frac{\hbar}{m_\pi c}\right)^2 \frac{V_{sc}}{r a_s}\,\frac{\exp\left[(r-r_s(A-1)^{1/3})a_s^{-1}\right]}{\left[1+\exp\left[(r-r_s(A-1)^{1/3})a_s^{-1}\right]\right]^2}\,\vec{\ell}\cdot\vec{\sigma} \\ & -V_{Cbp}\;, \end{aligned} \tag{53}$$

with an eigenvalue equal to the separation (binding) energy. V_c and V_{sc} are the strength of the central and spin-orbit parts for a shell. V_{Cbp} is the Coulomb potential evaluated from an equivalent uniform sphere of the same r.m.s radius as the actual nucleus. The geometrical parameters (r_0, a, a_s, r_s) and spin-orbit strength of the potential, V_{sc}, were taken from the work of Elton and Swift [El-67] in which single particle binding energies and electron scattering were fitted for various nuclei. The following is the values of the parameters used in our calculation for ^{12}C.

Level	V_c	$r_0(r_s)$	V_{sc}	a(a_s)	E_{BE}
$1s_{1/2}$	60	1.36	-	0.55	34.3 MeV
$1p_{3/2}$	55	1.36	9 MeV	0.55	15.8 MeV
$1p_{1/2}$					

(4) Calculation of the Half-shell Cross-section $\left[\frac{d\sigma}{d\Omega}\right]_{\pi-p}$

An on-shell cross section approximation was made for the half-shell cross section, $\left[\frac{d\sigma}{d\Omega}\right]_{\pi-p}$, in order to compare it to the known differential cross-section measured for free π^+ + p elastic scattering, which is on-shell energy. For the calculation of the on-shell cross-section, two choices were available because of the difference in the rest energy of the pion and proton in the entrance and exit channels. The first one was the initial energy prescription (IEP) which uses a two body energy corresponding to the initial relative momentum. The second choice was the final energy prescription (FEP) that employs the two-body energy in the rest frame of the outgoing pion and proton. In both prescriptions the scattering angle is the same. The FEP prescription was chosen in this dissertation. The on-shell $\pi^{\pm}$ + p cross-sections were calculated using the phase shift analysis of Rowe, Salomon and Landau [Ro-78].

4.2.3 Discussion of the ^{12}C Data with the DWIA Calculation

Fig. 4–5 shows the pion missing-mass coincidence spectrum for $E_x(^{11}B) < 10$ MeV, already described in section 3–2. Also shown are the curves resulting from the single proton knock-out DWIA calculations for the scattering from a proton bound in the 1p-shell. A spectroscopic factor $C^2S = 3.98$, the summed 1p-shell spectroscopic factor predicted by Cohen and Kurath [Co-67], and a separation energy $S_p = 15.8$ MeV were assumed. Fig. 4–6 is the spectrum for the $E_x(^{11}B) >$ 10 MeV. The calculations in Fig. 4–6 are for scattering from a 1s-shell proton with $S_p = 34.3$ MeV and $C^2S = 2.0$, the value of the shell-model limit. The energy

levels of ^{11}B which could result from 1p- and 1s-proton single-particle knockout from ^{12}C are also shown in Fig. 4–7.

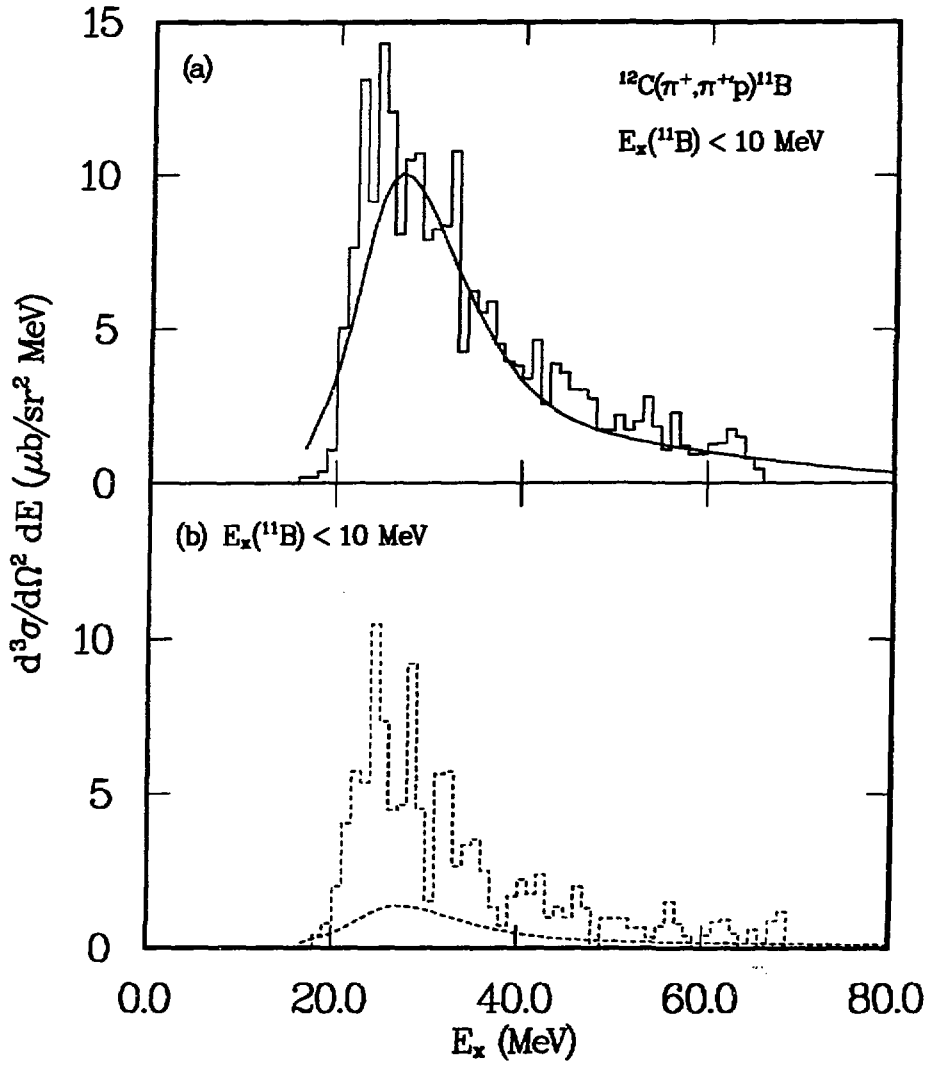

Fig. 4–5: $^{12}C(\pi^{\pm},\pi^{\pm\prime}p)$ spectra with THREEDEE calculations.

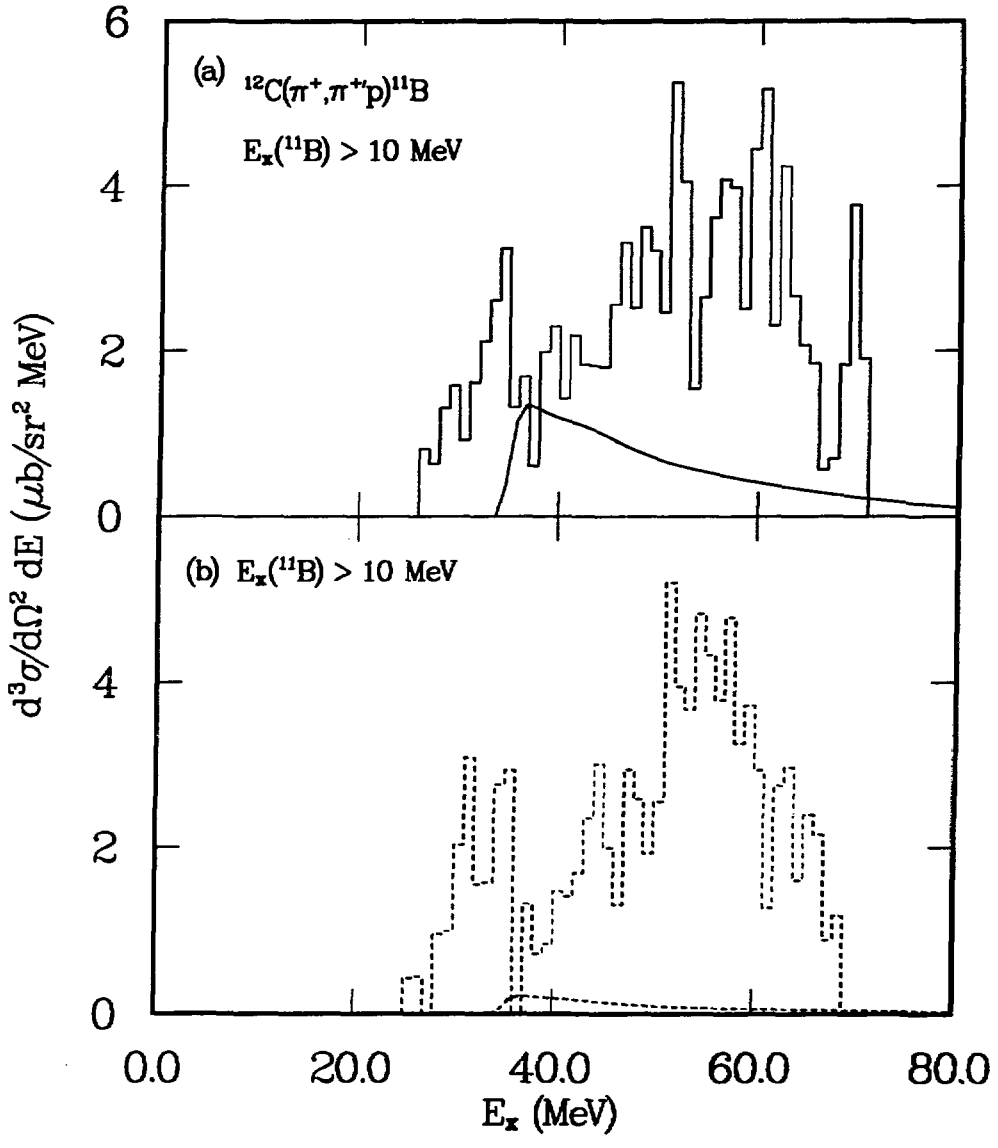

Fig. 4–6: $^{12}C(\pi^{\pm},\pi^{\pm\prime}p)$ spectra with THREEDEE calculations.

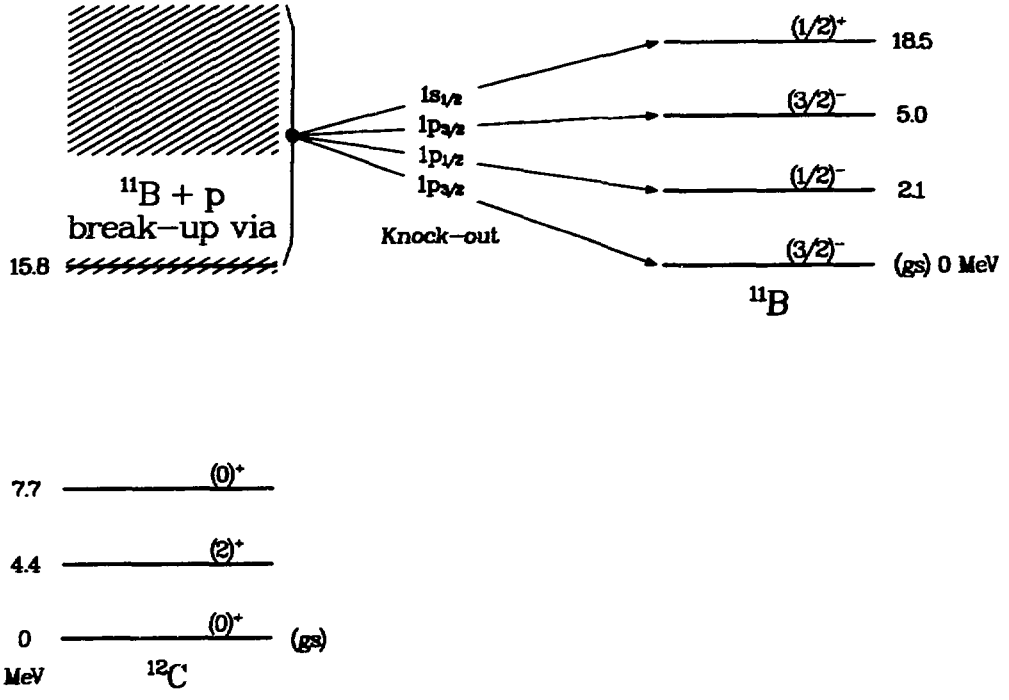

Fig. 4–7: Schematic diagram of single-proton knock-out process from ^{12}C and the resulting energy levels in ^{11}B. Energy levels are not scaled.

We expect a ratio $R = \frac{\sigma(\pi^+, \pi^{+\prime} p)}{\sigma(\pi^-, \pi^{-\prime} p)}$ close to 9 for quasi-free knock-out, the same as for π^+ and π^- scattering from free protons. Both sets of calculations performed with the code THREEDEE show π^+ scattering to be larger than π^- by nearly the free π–p ratio (for example, we calculate R $\sim$ 7.36 for 1p knock-out near the GDR of ^{12}C). However, the experimental ratio is only 1.59 on the average (Table 4–1). As seen in Fig 4–5, both shape and magnitude of the $(\pi^+, \pi^{+\prime}\mathrm{p})$ spectrum for $E_x(^{11}\mathrm{B}) < 10$ MeV are well described by the DWIA. However, the $(\pi^-, \pi^{-\prime}\mathrm{p})$ data for the same gate are much larger than the predicted values. This discrepancy would be even larger if we had used the 1p-shell spectroscopic factor of 2.9 and 1s-shell spectroscopic factor of 1.8 reported in Ref. [Ch-82]. The agreement between experiment and the DWIA prediction for $E_x(^{11}\mathrm{B}) > 10$ MeV is poor for both π^+ and π^- scattering.

The angular distributions of the emitted protons are plotted in Fig. 4–8 as a function of the outgoing proton angle in the center of mass system of the recoil ^{12}C. The angle is the average of the angles of the emitted protons in the CM frame for the given excitation energy region. The cross section for events leading to the ground state or the low lying states of ^{11}B, i.e., $E_x(^{11}\mathrm{B}) < 10$ MeV, summed over $E_x(^{12}\mathrm{C})$ from 20 to 30 MeV, is shown in top panel. Data for the higher excitation states of ^{11}B, $E_x(^{11}\mathrm{B}) \geq 10$ MeV, summed over $E_x(^{12}\mathrm{C})$ from 41 to 70 MeV are displayed in lower panel. The curves are the DWIA calculations described earlier. The $(\pi^+, \pi^{+\prime}\mathrm{p})$ data for $E_x(^{11}\mathrm{B}) < 10$ MeV are reasonably well-described by the DWIA. However, the $(\pi^-, \pi^{-\prime}\mathrm{p})$ data exhibit no clear peak in the recoil direction of the knocked-out proton in contradiction to the DWIA.

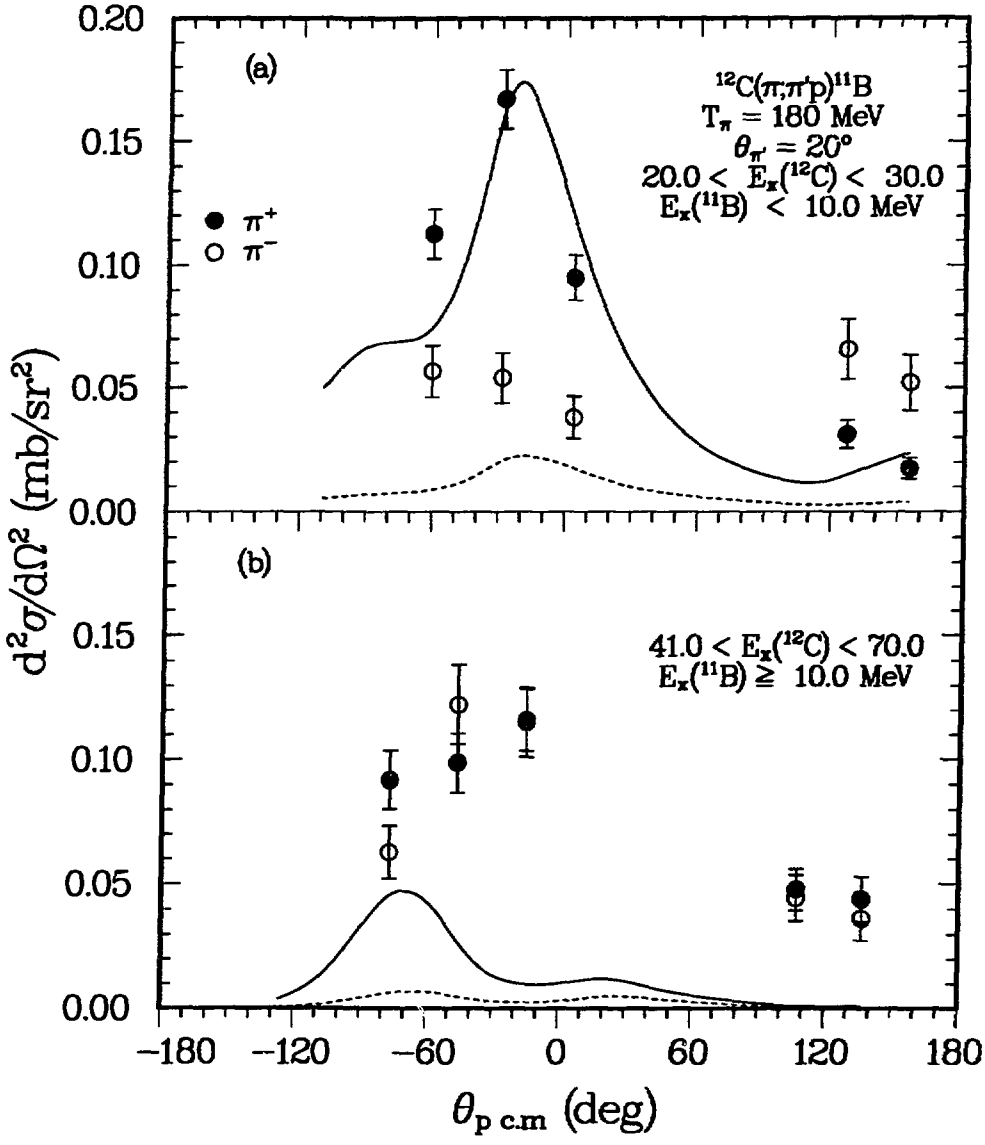

Fig. 4–8: Angular distributions of the emitted protons. Curves are THREEDEE calculations normalized by the spectroscopic factors described in text. Solid line is for π^+. Dashed line is for π^-.

Neither do the DWIA calculations for 1s-shell knock-out resemble either the $(\pi^+, \pi^{+\prime}\mathrm{p})$ or the $(\pi^-, \pi^{-\prime}\mathrm{p})$ data for $E_x(^{11}B) > 10$ MeV. In table 4–1 we present the ratio R of the data leading to $E_x(^{11}B) < 10$ MeV and the DWIA predictions for 1p-shell knock-out summed from 20 to 30 MeV of $E_x(^{12}C)$. The experimental value of R varies from a maximum of $R = 3.09 \pm 0.62$ near the quasi-free-knockout direction to a minimum of $R = 0.33 \pm 0.11$ in the opposite direction. However, the calculations predict large values of R at all angles, in sharp contrast with the data.

Table 4–1: The ratios $R = \sigma(\pi^+, \pi^+ p)/\sigma(\pi^-, \pi^- p)$ for each proton detector and the ratio of summed cross sections. The $\sigma(\pi^{\pm}, \pi^{\pm\prime}\mathrm{p})$ data were obtained by summing cross sections from 20 to 30 MeV in $E_x(^{12}C)$ with the $E_x(^{11}B) < 10$ MeV gate, at $T_\pi = 180$ MeV and $\theta_{lab} = 20°$.

θ_{pCM}	R(DWIA)	R (Experiment)
−60.3°	8.59	1.99 ± 0.41
−28.5°	7.89	3.09 ± 0.62
3.9°	6.75	2.50 ± 0.61
127.3°	5.29	0.47 ± 0.12
155.5°	6.02	0.33 ± 0.11
R of summed σ	7.36	1.59 ± 0.16

The calculations discussed so far include only the quasi-free knock-out process. Another process that can contribute to this $(\pi^{\pm}, \pi^{\pm\prime}\mathrm{p})$ reaction in the GR region is a semi-direct one in which the pion excites a state in the GR region that subsequently decays through emission of a proton. If the state in ^{12}C has good isospin and if the difference between the neutron and proton penetrabilities

is neglected, R must be equal to one at all emitted proton angles. In this case the decay of the state is governed by branching ratios and these are independent of the manner in which the state was created. Furthermore, the angular distribution should be symmetric about 90°. The data for $20 \leq E_x(^{12}\mathrm{C}) \leq 30$ MeV and $E_x(^{11}\mathrm{B}) < 10$ MeV could be qualitatively explained by a mixture of these two processes—direct (due to quasi-free knock-out) and semi-direct (due to inelastic scattering to states of good isospin). The angular distributions of the decay protons indicate that the $(\pi^+, \pi^{+\prime}\mathrm{p})$ is dominated by the direct decay whereas the $(\pi^-, \pi^{-\prime}\mathrm{p})$ must have a strong contribution from the semi-direct process. This process must, of course, also contribute to $(\pi^+, \pi^{+\prime}\mathrm{p})$, although the good agreement between absolute experimental cross sections and THREEDEE predictions suggest a predominance of the quasi-free process. We propose that the observed strong angle dependence of R is probably due to an interference between the amplitudes for these two processes.

In order to describe a situation which lies between the limits of quasi-free knock-out and the excitation and decay of states of good isospin, one may use a form of doorway model [Fe-67]. In this model, the interaction of the pion probe with the nucleus leads to proton particle-hole and neutron particle-hole states in the continuum with amplitudes approximately in the ratio of the free pion-nucleon couplings. These continuum states couple either to the GR states with width Γ_R, or they decay directly into a potential scattering state with width Γ_D (the quasi-free process). The decay of the GR states would lead to equal amplitudes for proton and neutron emission, i.e., R = 1, but the inteference with the quasifree

process causes π^+/π^- asymmetries. The enhancement of proton decay observed in the current $(\pi^-, \pi^{-\prime}\mathrm{p})$ data above the DWIA calculations indicates that Γ_R and Γ_D must be comparable in size for the continuum near the GR region of ^{12}C. This interference would be less important for $(\pi^+, \pi^{+\prime}\mathrm{p})$ because the direct amplitude is three times larger than for $(\pi^-, \pi^{-\prime}\mathrm{p})$. Therefore, the decay of the continuum in the region of the GR is largely governed by how it was excited. The absolute cross-sections predicted by THREEDEE depend on the choice of spectroscopic factors, but not the ratio R. Thus, our conclusions are based on the failure of simple DWIA calculations to reproduce R. We have made no attempt to include higher-order effects in the π–nucleus scattering such as those which have been predicted to arise from the Δ-hole model [Ky-84].

These observations in the region of the GDR in ^{12}C can be contrasted with the result obtained at higher excitation energies in ^{12}C (Fig. 4–6 and –8). At this high excitation region, $40 \leq \mathrm{E}_x(^{12}\mathrm{C}) \leq 70$ MeV, we find that more than half of the cross section seen in the coincidence spectrum corresponds to the data leading to $\mathrm{E}_x(^{11}\mathrm{B}) \geq 10$ MeV. For these events we observe a broad bump in Fig. 4–6 centered near 55 MeV of excitation in ^{12}C. The angular distribution of protons associated with this bump also appears to peak near the recoil direction of $^{12}\mathrm{C}^*$ but the ratio R (Fig. 4–8b) is near unity at all angles (Table 1 in Appendix III). The near equality of the $(\pi^+, \pi^{+\prime}\mathrm{p})$ and $(\pi^-, \pi^{-\prime}\mathrm{p})$ cross sections suggests that protons and neutrons are involved equally in the reaction. However, we do not believe that, for $\mathrm{E}_x(^{12}\mathrm{C}) \geq 40$ MeV, states of good isospin would play a major role except for possible double resonances [Mo-88b]. It is more likely that direct two, three, and

four nucleon removal are important here. This could be understood if we consider the mean free path of the pion in $\Delta_{3,3}$ region (Fig. 4–2). At lower excitation energies in ^{12}C it could be thought that the pion does not penetrate deep inside the nucleus, i.e. a surface reaction occurs. Thus, the impulse approximation holds well. For π^+, this surface reaction is dominated by quasi-free knock-out process whereas, for π^-, it also contributes to the excitation of the GR via inelastic scattering process. However, the observation that the DWIA calculation do not agree with both π^+ and π^- data in the high excitation region of ^{12}C implies that the pion has indeed penetrated deeply inside the nucleus, and the pion's short mean free lengh ($l \sim 0.5$ fm) near the $\Delta_{3,3}$ causes multi-particle collisions. The thresholds for two, three, and four nucleon removal are at 27, 34, and 36 Mev, respectively. Lourie et al. [Lo-86] also observed considerable strength in this region of excitation energy in the ^{12}(e,e'p) reaction. They interpreted this strength as due to multinucleon reaction mechanisms. The failure of the one-nucleon-knock-out calculations with THREEDEE to reproduce the magnitude and the near equality of the π^+ and π^- data suggests the importance of such processes also for $(\pi, \pi' \mathrm{p})$.

4.3 Theoretical Analysis of the ^{208}Pb($\pi^{\pm}, \pi^{\pm\prime}$N) Data

The THREEDEE calculations for ^{208}Pb($\pi^{\pm}, \pi^{\pm\prime}$N) reaction were made in the same way as those for ^{12}C, except for the nucleon ground state densities. Instead of Harmonic Oscaillator distribution, a two-parameter Fermi function, $\rho(r) = \rho_0 \frac{1}{1 + e^{(r-c)/z}}$, with c = 6.51 fm and $z = 0.55$ was used in order to be consistent

with the analysis of the π inelastic scattering data from ^{208}Pb, which will be introduced in a later section.

4.3.1 Discussion of the ^{208}Pb($\pi^{\pm}, \pi^{\pm\prime}$N) Data

In Fig. 4–9 the pion missing mass spectra from the ^{208}Pb($\pi^{\pm}, \pi^{\pm\prime}$p)Tl reaction, already described in Chapter 3, are shown along with the calculations of single proton knock-out using the first four energy levels of ^{207}Tl (Fig. 4–10). The calculations for the scattering from a proton bound in the $3s_{1/2}$-, $2d_{3/2}$-, $1h_{11/2}$-, and $2d_{5/2}$-shell are represented by dotted, chaindotted, chaindashed, and dashed line, respectively. The solid curve is the sum of the results from all four levels. The values of the shell-model limit were used for the spectroscopic factors for each level. These values are not much different from those obtained from ^{208}Pb(d,^{3}He)^{207}Tl reaction in the work of Grabmayr et al. [Gr-87]. A proton separation energy, S_p = 8.01 MeV [Nu-86], was assumed.

Due to the Coulomb barrier, direct decay in the giant resonance region [$E_x(^{208}\text{Pb}) \sim 10$ MeV] is strongly inhibited as shown in both data and calculations. The emitted protons begin to penetrate the barrier around 13 MeV in the data and 16 MeV for the DWIA calculations. The single proton-knockout calculations underestimate the experimental cross-sections for both ($\pi^+, \pi^{+\prime}$p) and ($\pi^-, \pi^{-\prime}$p) reactions, but are in better agreement with the π^+ data than the π^-. This indicates that processes other than quasi-free scattering (such as semi-direct and multiparticle knock-out) contribute to this region. To investigate this further, the angular distributions of the decay protons were measured.

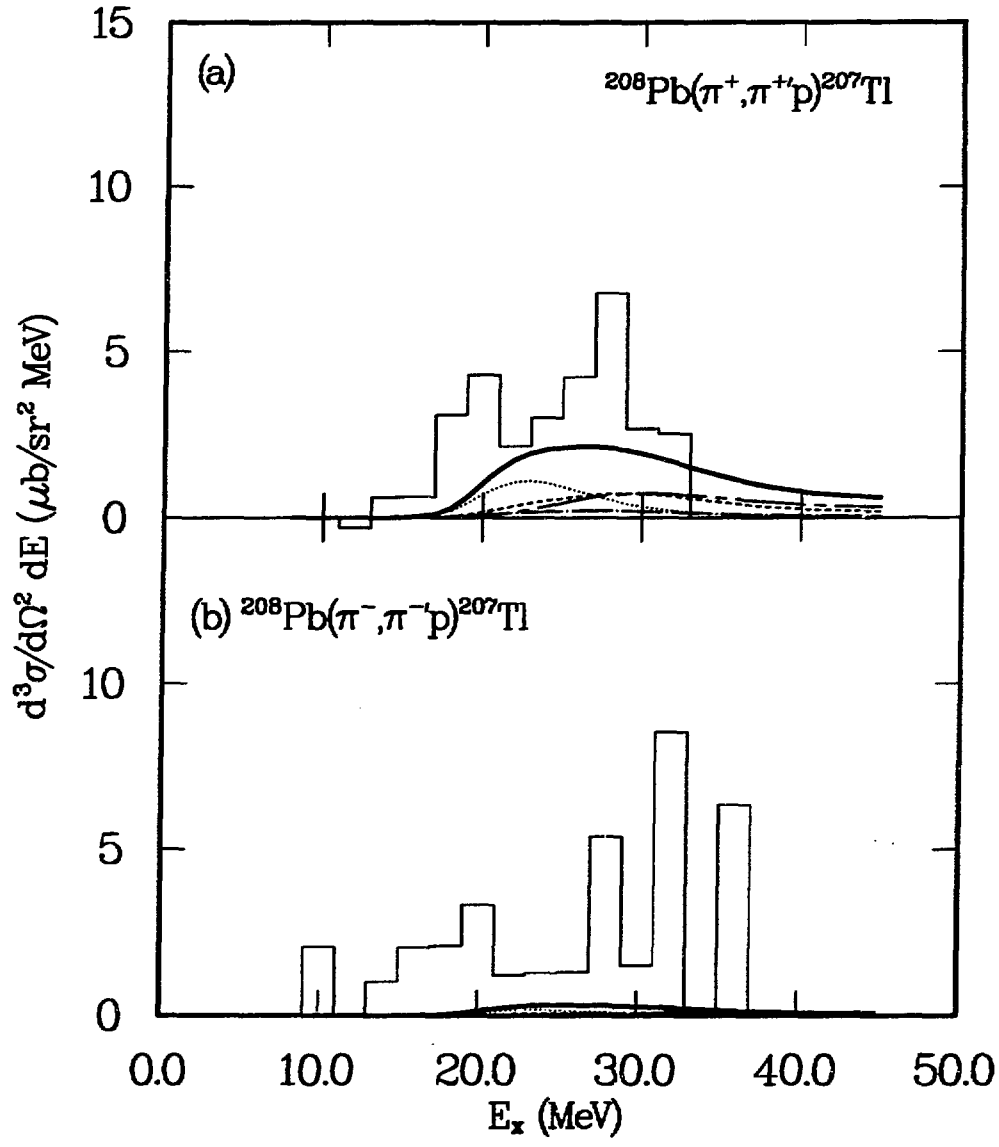

Fig. 4–9: ^{208}Pb($\pi^{\pm}$, $\pi^{\pm\prime}$p) spectra. Curves are THREEDEE calculations normalized by the spectroscopic factors of the Shell-model limit.

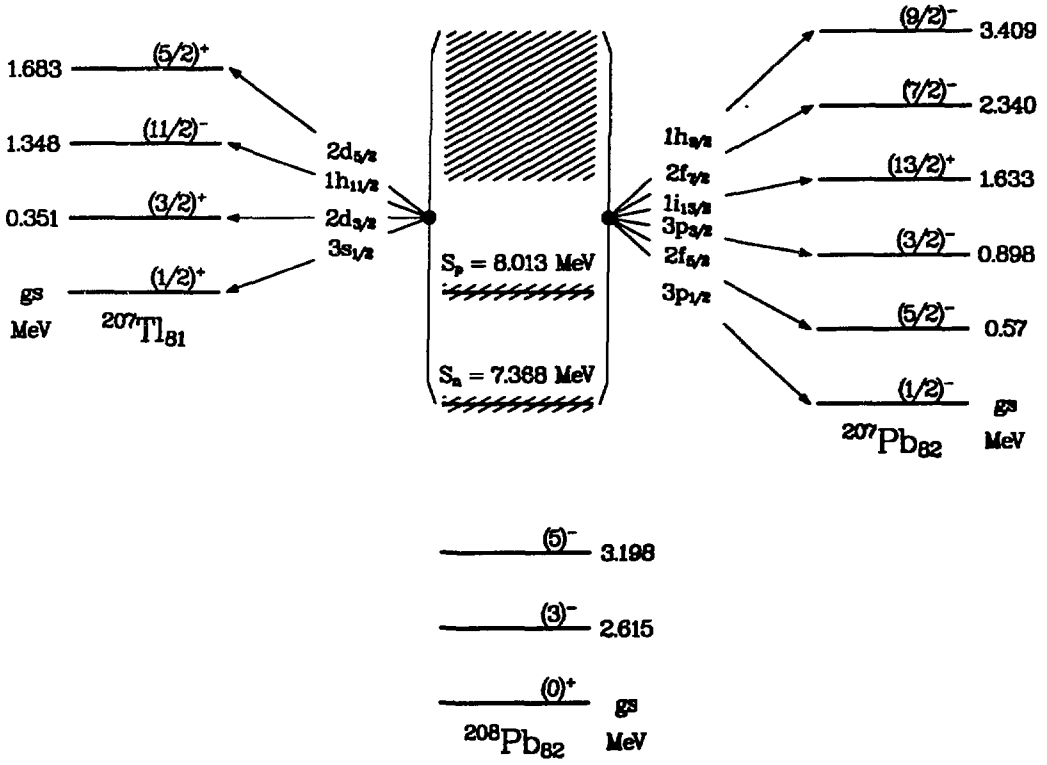

Fig. 4–10: Schematic representation of single-nucleon knock-out process from ^{208}Pb and resulting energy levels in ^{207}Pb and ^{207}Tl. Energy levels are not scaled.

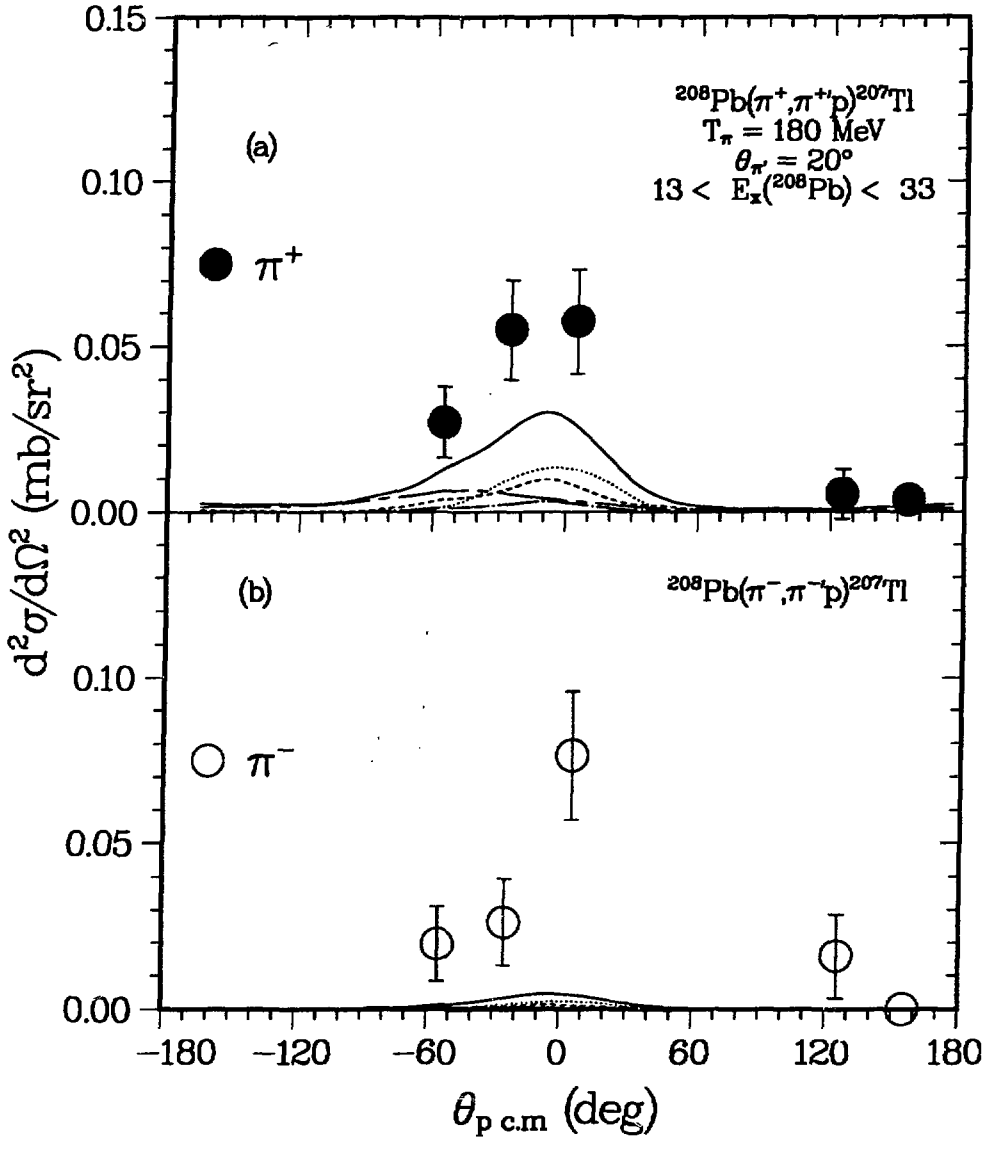

Fig. 4–11: Angular distributions of the emitted protons. Curves are THREE-DEE calculations normalized by the spectroscopic factors described in text.

Fig. 4–11 shows the angular distributions of the protons for both $(\pi^+, \pi^{+\prime}\mathrm{p})$ and $(\pi^-, \pi^{-\prime}\mathrm{p})$ reactions, summed over excitation energies in ^{208}Pb from 13 to 33 MeV. The results of the DWIA calculations are also presented. The shape of the data is similar to that of the $(\pi^+, \pi^{+\prime}\mathrm{p})$ to high $E_x(^{12}\mathrm{C})$ for $E_x(^{11}\mathrm{B}) > 10$ MeV, seen in Fig. 4–8. Here, too, the averaged ratio, $\mathrm{R} = \frac{\sigma(\pi^+,\, \pi^{+\prime}\mathrm{p})}{\sigma(\pi^-,\, \pi^{-\prime}\mathrm{p})}$, is near one (Table 2 in Appendix III), and the peak is around the recoil direction of the ^{208}Pb* (i.e., $\theta_{CM_p} = 0°$). As we have already suggested in ^{12}C case, multi-particle break-up may contribute to this region. However, unlike to the ^{12}C case, the DWIA calculations for $(\pi^+, \pi^{+\prime}\mathrm{p})$ describes the shape of the π^+ data relatively well, though the calculation accounts for only about half of the total $(\pi^+, \pi^{+\prime}\mathrm{p})$ cross-section. The shape predicted for π^- is also in agreement with that of π^- data, but the magnitude is severely underestimated. All these observations suggest that there exist contributions from direct single proton knock-out as well as direct multiparticle break-ups in the nuclear continuum region above GR in ^{208}Pb. Single knock-out appears to be stronger in $(\pi^+, \pi^{+\prime}\mathrm{p})$ reaction while multiparticle knock-out looks more dominant in $(\pi^-, \pi^{-\prime}\mathrm{p})$ reaction. Statistical decay, which should have an isotropic angular distribution [Se-76], does not seem to contribute much for either $(\pi^+, \pi^{+\prime}\mathrm{p})$ or $(\pi^-, \pi^{-\prime}\mathrm{p})$.

The exclusive pion missing mass spectra for $^{208}\mathrm{Pb}(\pi^\pm, \pi^{\pm\prime}\mathrm{n})$ reaction, summed over all five neutron detectors, are shown in Fig. 4–12 along with the results of DWIA single neutron knock-out calculations. The data, as mentioned in Chapter 3, have not been corrected for neutron detection efficiency. The first six energy levels of ^{207}Pb were used for the calculations [see Fig. 4–10]. They are

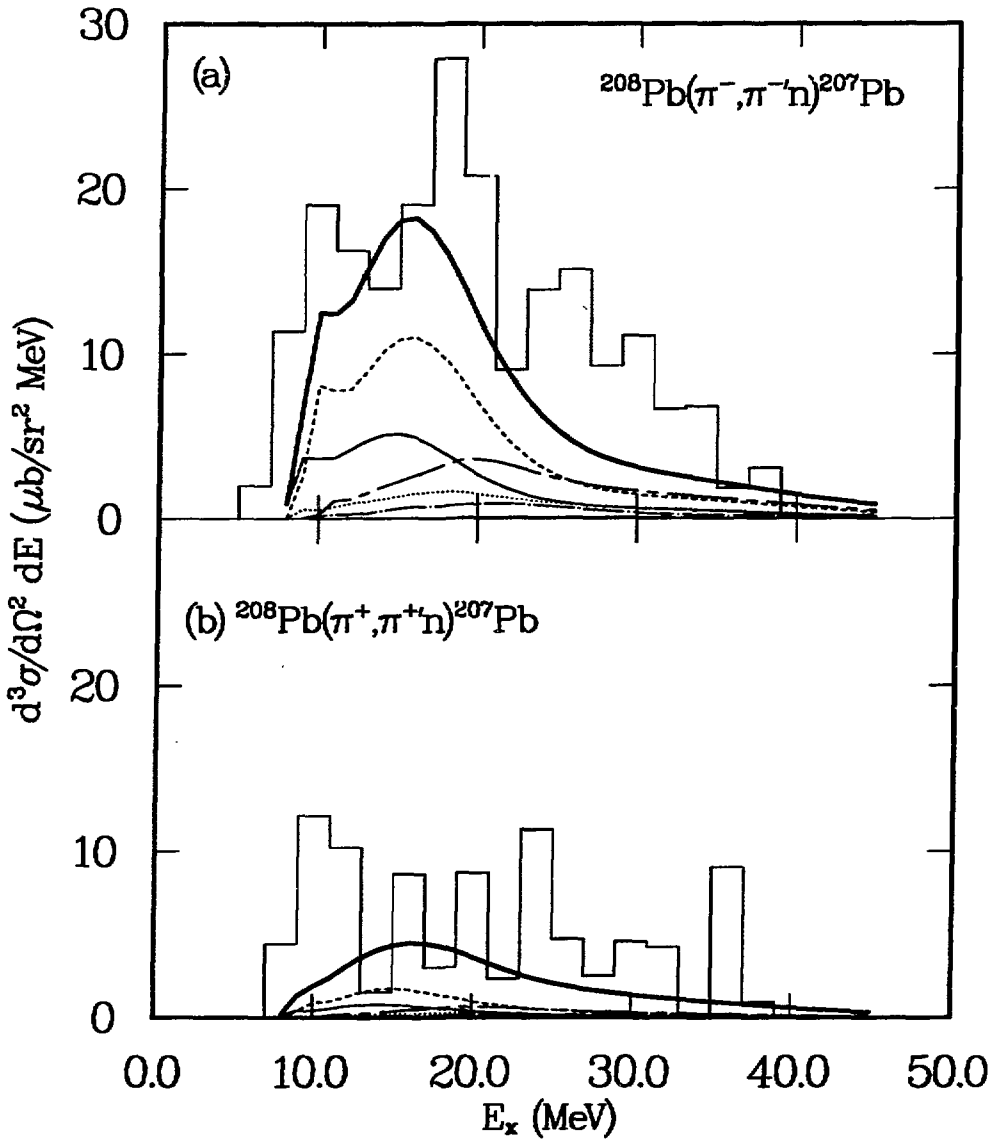

Fig. 4–12: ^{208}Pb($\pi^{\pm}$,$\pi^{\pm\prime}$n) spectra. Curves are THREEDEE calculations as explained in text. The data has not been corrected for neutron detection efficiency.

$3p_{1/2}$ (solid), $2f_{5/2}$ (dot), $3p_{3/2}$ (dash), $1i_{13/2}$ (chaindot), $2f_{7/2}$ (chaindash), and $1h_{9/2}$ (solid). The $1h_{9/2}$ calculation is too small to appear. The $1i_{13/2}$ contribution to $(\pi^+, \pi^{+\prime}n)$ is also very small. The thick solid curves are the summation of the results including all six levels. For the $3p_{1/2}$-, $2f_{5/2}$-, $3p_{3/2}$-, $1i_{13/2}$-, $2f_{7/2}$-, and $1h_{9/2}$-shell, the spectroscopic factors (C^2S) of 2.0, 4.82, 3.87, 7.67, 4.98, and 4.5 were used, respectively. These values are the averaged C^2S from the ^{208}Pb(p,d)^{207}Pb reaction in the work of Dickey, Kraushaar and Rumore [Di-82]. The single neutron separation energy assumed in the calculation was 7.38 MeV [Tr-88].

The calculations reproduce the shape of the data very well. However, since the data have not been corrected for neutron detection efficiency ($\sim$ 10%), the calculations enormously underestimate the magnitude of the cross-section. This huge discrepancy is in contrast to the $(\pi^{\pm}, \pi^{\pm\prime}p)$ case.

The cross-sections for emitted neutrons, summed over excitation energies in ^{208}Pb from 16 to 40 MeV, are plotted in Fig. 4–13 as a function of the outgoing neutron angle in the center of mass system of the recoil ^{208}Pb*. The shapes of the angular distributions for the $(\pi^{\pm}, \pi^{\pm\prime}n)$ are different from those of the $(\pi^{\pm}, \pi^{\pm\prime}p)$ in the similar ^{208}Pb-excitation energy range (Fig. 4–11). These angular distributions of neutrons have not been corrected for the neutron detection efficiency, since we do not know the neutron energy distributions for the emitted neutrons, nor do we know the neutron efficiency as a function of energy. Nevertheless, the shapes are expected to be consistent with the $(\pi^+, \pi^{+\prime}p)$ results, even if the ratio $R = \frac{\sigma(\pi^+, \pi^{+\prime}n)}{\sigma(\pi^-, \pi^{-\prime}n)}$ is not expected to be near unity since N > Z. Here, instead of

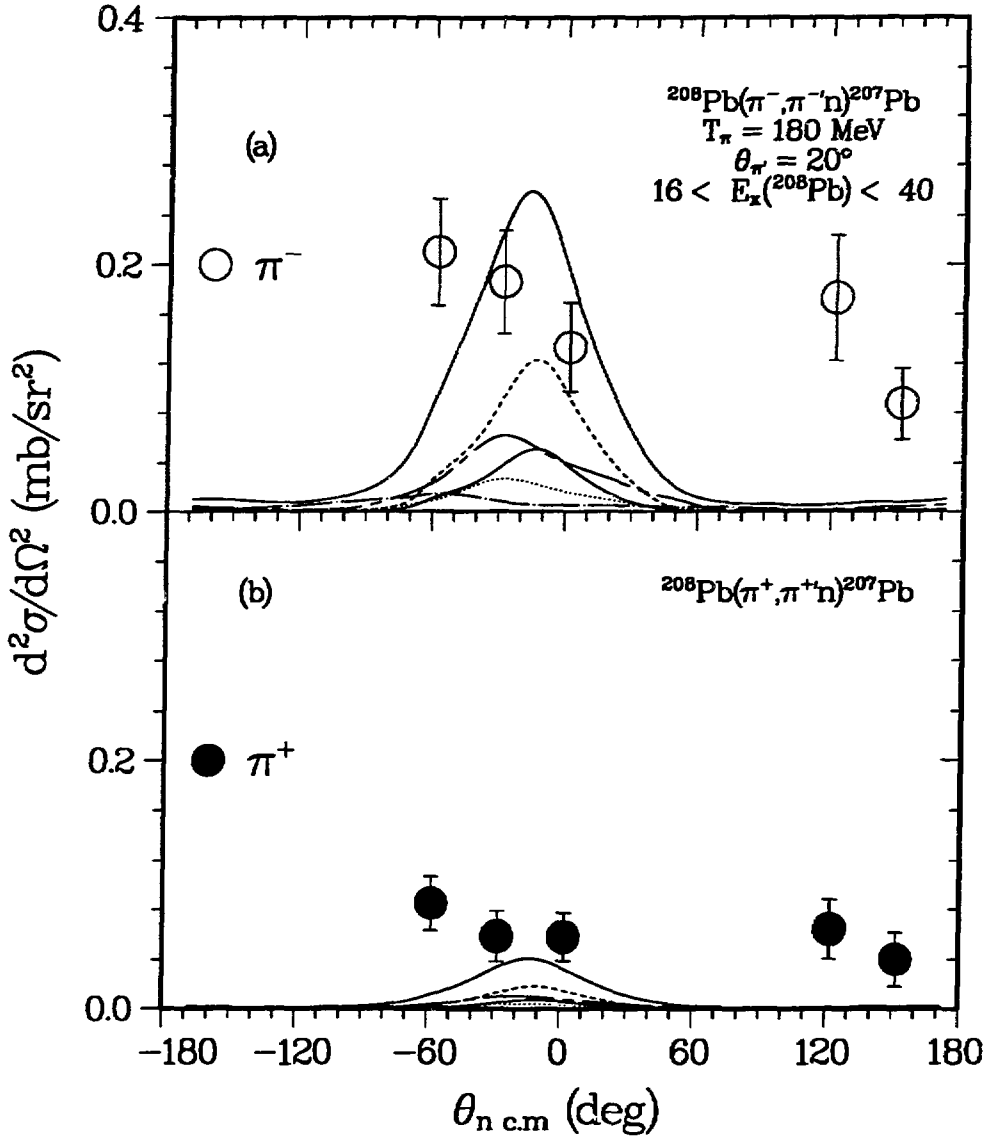

Fig. 4–13: Angular distributions of neutrons from $(\pi^{\pm}, \pi^{\pm\prime}n)$ reaction. The curves are THREEDEE calculations described in text. The correction for neutron detection efficiency has not been made.

having indications of multiparticle break-ups, both $(\pi^+, \pi^{+\prime}\mathrm{n})$ and $(\pi^-, \pi^{-\prime}\mathrm{n})$ data show a signiture of the dominance of decay due to semi-direct process (that is, relatively isotropic angular distribution and symmetry about 90°). The predictions of the DWIA are not in good agreement with the data in both shape and magnitude. The averaged ratio R is about 2.6 while the DWIA calculation predicts R $\sim$ 6.4 (Table 3 in Appendix III). This ratio of 2.6 is consistent with the ratio, $r = \frac{\sigma(\pi^-)}{\sigma(\pi^+)}$, of the (π,π') data (Chapter3). The deviation from R $\sim$ 1, which is the ratio expected in the dominance of semi-direct process, may be caused by N > Z and small components of the quasi-free scattering amplitude along with other possible processes.

In Fig. 4–14 angular distributions of the neutrons, summed over excitation energies in ^{208}Pb from 8 to 15 MeV (including the GQR), are shown for both the $(\pi^+, \pi^{+\prime}\mathrm{n})$ and $(\pi^-, \pi^{-\prime}\mathrm{n})$ reactions. The angular distribution appears to be different for the two reactions. In the $(\pi^-, \pi^{-\prime}\mathrm{n})$ reaction, the neutron distribution appears to have a peak in near the quasi-free single-neutron knock-out direction ($\sim -18°$) as indicated by the DWIA calculation, but the peak near the knock-out direction is not observed in $(\pi^+, \pi^{+\prime}\mathrm{n})$. We have constructed a ratio of the sum of the three forward angle points to the sum of the two large angle points for both π^- and π^+. The ratio is larger for π^- (1.38 $\pm$ 0.48) than for π^+ (0.76 $\pm$ 0.29). Our ability to say that the π^+ and π^- distributions are different is estimated by the statistical accuracy of the data. A forward-peaked shape for the $(\pi^-, \pi^{-\prime}\mathrm{n})$ angular distribution is consistent with the assumption that the dominant decay mode of the GR is direct decay from a neutron–neutron hole doorway. The rela-

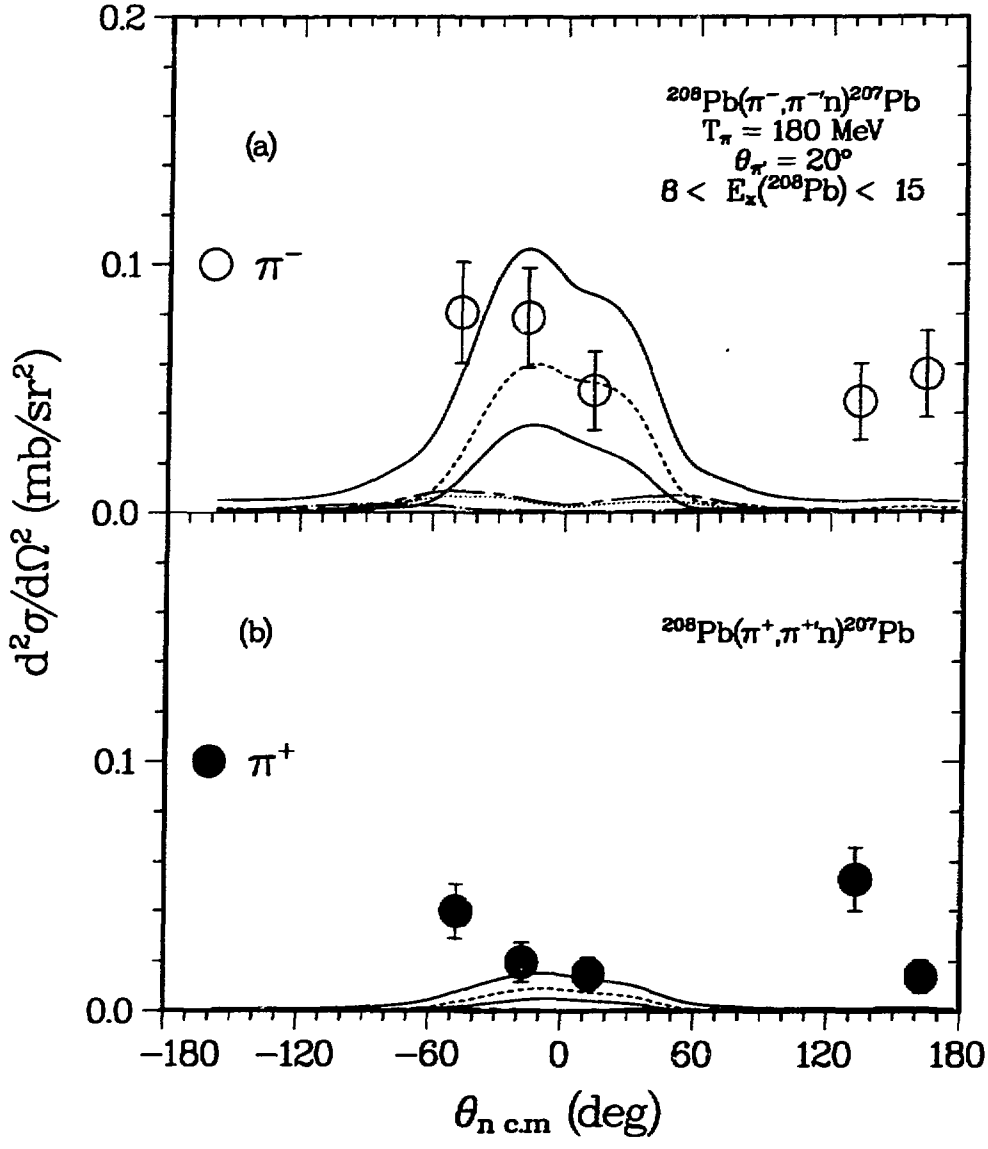

Fig. 4–14: Angular distributions of neutrons for the $(\pi^{\pm}, \pi^{\pm\prime}n)$ reactions near GR. Curves are THREEDEE calculations described in text. The correction for neutron detection efficiency has not been made.

tively flat ($\pi^+, \pi^{+\prime}$n) angular distribution implies that the neutrons arise from statistical decay (thermal evaporation). This flat angular distribution could be understood as follows. The (π^+,$\pi^{+\prime}$) reaction excites proton-proton hole states preferentially by a factor of 9 (assuming no distortion). Thus there is very little population of the neutron-neutron hole doorway states (necessary for direct neutron decay). In addition, the Coulomb barrier inhibits direct decay of protons from the proton-proton hole doorway. This barrier for the proton results in further inter nucleon collisions that eventually spit out a neutron or a proton. One consequence of this proposition is that the ratio of cross-sections for inelastic scattering to the GR region may have to be written in terms of an incoherent sum of cross-sections to neutron and proton doorway states, since different final states of the residual nucleus are populated in these two processes. That is, the neutron-neutron hole states that are more strongly excited by π^-, predominantly directly decay to single-hole low-lying states of the residual nucleus ^{207}Pb whereas the proton-proton hole states that are more favorably excited by π^+ randomly populates the levels in ^{207}Pb via statistical decay.

A schematic model that does not include distortions and assumes dominance of the $\Delta_{3,3}$ resonance in the π–N interaction can be used to estimate the size of this effect. This incoherent sum gives,

$$r = \frac{\sigma(\pi^-, \pi^{-\prime})}{\sigma(\pi^+, \pi^{+\prime})} \cong \frac{9M_n^2 + M_p^2}{9M_p^2 + M_n^2} \tag{54}$$

instead of the usual coherent sum,

$$r = \frac{\sigma(\pi^-, \pi^{-\prime})}{\sigma(\pi^+, \pi^{+\prime})} \cong \frac{(3M_n + M_p)^2}{(3M_p + M_n)^2} \tag{55}$$

where M_n and M_p are neutron and proton matrix elements, respectively. The cross-section ratio predicted for the same value of M_n/M_p from these two models is very different. Using R = 1.54 (= N/Z) expected from the HD model, we find that equation (54) gives r = 1.96 whereas r = 1.52 results from equation (55).

The better agreement of Eq. (54) with our experiment ratio r led us to reexamine the effect of the supposition above more quantitably by using the GQR state in ^{208}Pb. In order to do this, used the previously obtained ^{208}Pb(π,π') data [Se-86] were used, since our data for π^+ and π^- were measured at $\theta = 20°$; At this angle the angular distribution for the GQR in ^{208}Pb is not at its maximum either for π^+ or π^-. Our giant quadrupole resonace cross section may therefore contain the contributions from other than $\ell = 2$ partial waves. To illustrate this point further, the angular distributions extracted for the giant quadrupole resonance at $T_\pi = 162$ MeV [Se-86] is shown in Fig. 4–15. The figure also includes the fit from the DWIA calculations performed with the code NDWPI, which will be explained in the next section. As noticed, the angle that gives the maximum in angular distribution for π^+ is different from the one for π^-, i.e., 18° for π^+ and 16° for π^-. The different impact parameters due to different Coulomb effects between π^+–nucleus and π^-–nucleus interactions, and the different bound radius of neutron and proton due to N $\gg$ Z in a heavy nucleus are the main reasons for the difference in the angles [Mo-89]. The previous data provides the angular distribution and fit. From the fit, it is possible to extract pure GQR cross section for π^+ and π^-, respectively. In next sections, the brief description of the π–inelastic scattering formula based on the impulse approximation will be presented, followed by the

reexamination of $\frac{M_n}{M_p}$ in the pure GQR region of ^{208}Pb.

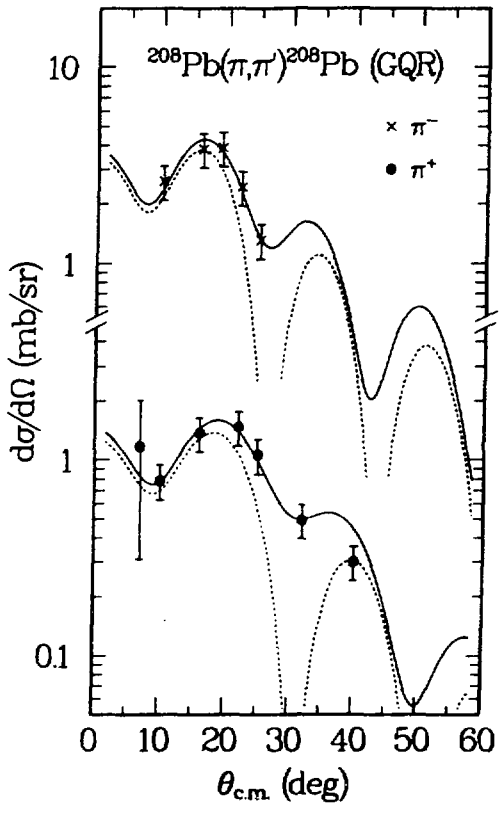

Fig. 4–15: Angular distributions for the GQR measured at $T_\pi = 162$ MeV. Circles are for π^+ and crosses for π^-. The solid curves are the E2 + E4 calculations and the dashed curves are the pure E2 calculations [Se-86].

4.4 Theoretical Reanalysis of ^{208}Pb(π,π') Data

4.4.1 Macroscopic Pion Inelastic Scattering Formula

Following is the description given in the program DWPI written by Eisenstein and Miller [Ei-76b]. According to them, when the target has arbitrary spin, the π–nucleus inelastic scattering differential cross section for the excitation of a discrete excited state can be expressed as

$$\left[\frac{d\sigma}{d\Omega}\right]_{inel} = \frac{\pi^2}{k_i^2(2I+1)} \sum_L \sigma_L P_L(\cos\theta) \,, \tag{56}$$

where

$$\begin{aligned}
\sigma_L &= \sum (2J+1)(2J_1+1)(2L+1)\sqrt{2\ell+1}\sqrt{2\ell'+1} \\
&\quad \times T^{J^*}_{\ell I,\ell' I'} T^{J_1}_{\ell_1 I,\ell'_1 I'} \langle \ell 0 L 0 | \ell_1 0 \rangle \langle \ell' 0 L 0 | \ell'_1 0 \rangle \\
&\quad \times W(\ell L I J_1; \ell_1 J) W(\ell' L I' J_1; \ell'_1 J)
\end{aligned}$$

$k_i \equiv$ the center of mass momentum of the incoming pion

$I \equiv$ the ground state angular momentum of the target

$\ell \equiv$ the angular momentum of the pion

$I' \equiv$ the angular momentum of the excited state

$T^J_{\ell I,\ell' I'} \equiv$ the transition matrix element for states of total angular momentum J

$W(\ell L I J_1; \ell_1 J) \equiv$ the Wigner symbol .

If the standard DWIA treatment is used, (1) the elastic scattering is included to all orders by using distorted waves, and (2) the inelastic transition is treated to

first order only. Then, the T-matrix element between the initial and final states in the nucleus becomes

$$T^J_{\ell I,\ell' I'} = \sum_{mMm'M'} \langle \ell' m' I' M' | Jq \rangle \langle \ell m I M | Jq \rangle \times \left\langle \psi^-_{\ell m} \Phi_{IM} | H' | \psi^+_{\ell' m'} \Phi_{I'M'} \right\rangle \quad (57)$$

where the π wave functions are $\psi^{\pm}_{\ell m}(r) = i^{\ell} \frac{U^{\pm}_{\ell}(r)}{r} Y_{\ell m}(\hat{r})$. Typically there are two approaches to handle the T-matrix element: microscopic and macroscopic. In the microscopic model, shell model wave functions are used for the initial and final states. Therefore, the microscopic approach is most appropriate for states of single-particle character. In the macroscopic approach, the collective model is used for the description of nuclear excitation. The nucleus is allowed to vibrate or rotate by changing the radius R as a function of a angle, $R(\theta, \phi) = R_0 [1 + \beta_\ell Y_{\ell m}(\theta, \phi)]$. The transition to discrete nuclear excited states is viewed as the excitation caused by the collective surface vibration or rotation of the nucleus. The microscopic model can also describe the collective modes of the nucleus as a coherent superposition of many single particle-hole excitations. However, it would require the very bulky calculations. The computer program DWPI uses the macroscopic collective model for the treatment of the π–nucleus inelastic scattering.

In order to obtain the T-matrix elements based on the macroscopic model, a ground state nuclear density $\rho(r)$ is chosen so that

$$\int \rho(r, c, a) d^3r = 1 \, . \quad (58)$$

The radius parameter c is written with an explicit angular dependence as

$$c = c_0[1 + \sum_{\lambda\mu} \alpha_{\lambda\mu} Y_{\lambda\mu}(\hat{r})] \, . \tag{59}$$

This characterizes dynamical couplings between the ground state and the vibrational (or rotational) levels. The collective amplitude $\alpha_{\lambda\mu}$ for vibrational excitation is a linear combination of the nuclear-vibrational-excitation (phonon) creation and annihilation operators $b^+_{\lambda\mu}$ and $b_{\lambda\mu}$, i.e.,

$$\alpha_{\lambda\mu} = \frac{\beta_\lambda}{\sqrt{2\lambda+1}}[b_{\lambda\mu} + (-1)^\mu b^+_{\lambda-\mu}] \tag{60}$$

where

λ = the orbital angular momentum of a mode

μ = the orbital angular momentum projection

β_λ = the static deformation parameter in the rotational model

the r.m.s amplitude of vibration in the vibrational model.

For rotational excitation, the $\alpha_{\lambda\mu}$ is the β_λ of the ground state.

Now a given $\rho(r, c)$ can be expanded about c_0 to first order in $(c - c_0)$ using Eq. (59). Then,

$$\begin{aligned} \rho(r, c) &= \rho(r, c_0) + \delta\rho \\ &= \rho(r, c_0) + \sum_{\lambda\mu} \alpha_{\lambda\mu} F_\lambda(r) Y_{\lambda\mu}(\hat{r}) \end{aligned} \tag{61}$$

where the transition density $F_\lambda(r)$ is given by

$$F_\lambda(r) = c \left.\frac{\partial\rho}{\partial c}\right|_{c=c_0} = - c \left.\frac{\partial\rho}{\partial r}\right|_{c=c_0} \, . \tag{62}$$

After factorizing the first order multiple scattering theory [Ki-55 and references in Ei-76b], the full coordinate space optical potential is given by

$$V_n(r) = At_{\pi N}\rho(r,c) \tag{63}$$

where

$$\begin{aligned} t_{\pi N} &= \text{the } \pi - \text{nucleon t-matrix (in general non local)} \\ A &= \text{the number of nucleons in the target nucleus .} \end{aligned}$$

The optical potential that generate the nuclear excitation is from the deformed part of density $\delta\rho$ in Eq. (61) and can be written as

$$\begin{aligned} < \Phi_{I'M'}|H|\Phi_{IM} > &= < I'M'|At_{\pi N}\delta\rho|IM > \\ &= At_{\pi N}\sum_{\lambda\mu} F_\lambda(r)Y_{\lambda\mu}(\hat{r}) < I'M'|\alpha_{\lambda\mu}|IM > \end{aligned} \tag{64}$$

Thus, by inserting Eq. (64) into Eq. (57) the T-matrix is finally obtained, where $T^J_{\ell I,\ell' I'}$ is directly proportional to β_λ, i.e., $T^J_{\ell I,\ell' I'} \propto \beta_\lambda$.

For the analysis of the ^{208}Pb(π,π') data, the more generalized form of the elastic-scattering optical potential than Eq. (48) in section 4.2.2 was used to accomodate the separation of the neutron and proton density distributions. The optical potential, following the potential form of Eq. (43) and using Eq. (48), can be expressed as

$$\begin{aligned} V_n^{\pm}(r) &= -[Zb^{\pm}_{p0}P_\pi^2\rho_p(r) + Nb^{\pm}_{n0}P_\pi^2\rho_n(r)] \\ &\quad + Zb^{\pm}_{p1}\vec{\nabla}\rho_p(r)\cdot\vec{\nabla} + Nb^{\pm}_{n1}\vec{\nabla}\rho_n(r)\cdot\vec{\nabla} \end{aligned} \tag{65}$$

where $\rho_p(r)$ and $\rho_n(r)$ have the form of Eq. (61),

$$
\begin{aligned}
b_{p0}^{+} &= \frac{4\pi\zeta}{P_\pi^3}\,\alpha_{31}^{0} = b_{n0}^{-} \\
b_{p0}^{-} &= \frac{4\pi\zeta}{P_\pi^3}\,\frac{\alpha_{31}^{0}+2\alpha_{11}^{0}}{3} = b_{n0}^{+} \\
b_{p1}^{+} &= \frac{4\pi\zeta}{P_\pi^3}\,(2\alpha_{33}^{1}+\alpha_{31}^{1}) = b_{n1}^{-} \\
b_{p1}^{-} &= \frac{4\pi\zeta}{P_\pi^3}\,\frac{2\alpha_{33}^{1}+\alpha_{31}^{1}+4\alpha_{13}^{1}+2\alpha_{11}^{1}}{3} = b_{n1}^{+}\ ,
\end{aligned}
$$

with the notation adopted in section 4.2.2, and the superscript $(\pm)$ stands for the different optical potential for π^+ and π^-, respectively. Since the optical potential above, Eq. (65), is not available as one of the options in the program DWPI, the modified code NDWPI with the option was employed for the separation of proton and neutron deformation parameters, β_p and β_n, which eventually make the extraction of $\frac{M_n}{M_p}$ possible.

4.4.2 Sum Rules and Hydrodynamical Predictions of $\frac{M_n}{M_p}$

The sum rule states that the transition strength to an excited state cannot be greater than the sum of the oscillator (nucleon) strength, i.e., it is the upper bound of the strength. Following Bohr and Mottelson [Bo-75], the sum of the oscillator strength can be written as

$$
\begin{aligned}
S(\lambda) &\equiv \sum_n (E_\eta - E_0)|\langle\eta|F|0\rangle|^2 \\
&= \frac{1}{2}\langle 0|[F,[H,F]]|0\rangle \qquad (66)
\end{aligned}
$$

where λ is the angular momentum transferred, F is a real (Hermitian) transition operator, and η represents the complete set of excited states. If the effects of

velocity dependent interactions are neglected, Eq. (66) can be further expressed as the expectation value of one body operator after evaluating the commutator. The fact that the sum can be described as an expectation value of a one-body operator and is, thus, insensitive to the details in the initial state is the significance of the linear energy weighted sum rule (EWSR) [Bo-75]. Ignoring the center of mass correction (order of $ZA^{-\lambda}$ or less), we obtain the classical sum rule for the isoscalar ($\Delta T = 0$) and isovector ($\Delta T = 1$) electric multipole ($\lambda \geq 2$):

$$\begin{aligned} S(\Delta T = 0, E_\lambda) &= S(\Delta T = 1, E\lambda) \\ &= \left[\frac{\hbar^2}{8\pi M}\right] A\lambda(2\lambda+1)^2 e^2 \left\langle r^{2\lambda-2}\right\rangle , \end{aligned} \tag{67}$$

where A is the mass number of the target nucleus and M is the nucleon mass.

The strength of the transition to a giant resonance state can be expressed as the fraction of the energy weighted sum rule:

$$\text{Fraction} = \frac{E_x \cdot B(\lambda; J_i \rightarrow J_f)}{S(\lambda; J_i \rightarrow J_f)} \tag{68}$$

where E_x is the excitation energy to reach the final state from the ground state, and $B(\lambda)$ is the reduced transition probability with the unit of e^2 $(\text{fm})^{2\lambda}$. The reduced transition probability, $B(\lambda; J_i \rightarrow J_f)$, is given by:

$$\begin{aligned} B(\lambda; J_i \rightarrow J_f) &\equiv B(\lambda \uparrow) \\ &= \frac{1}{(2J_i+1)} \mid (J_f || T_\lambda || J_i) \mid^2 . \end{aligned} \tag{69}$$

Here $< J_f || T_\lambda || J_i >$ is the reduced transition matrix element and T_λ is the transition operator [Bo-69]. The inverse transition probability, $B(\lambda \downarrow)$, is related

to B($\lambda\uparrow$) by the reciprocity theorem, i.e.,

$$B(\lambda; J_f \rightarrow J_i) = \frac{2J_i+1}{2J_f+1}\, B(\lambda; J_i \rightarrow J_f)\,. \tag{70}$$

The reduced transition matrix element for an electric transition can be expressed in terms of the deformation parameter β and the radial part of the transition density $F(\vec{r})$ in the collective model. Then, the multipole transition matrix can be defined as

$$M(E\lambda) = \frac{< J_f||T_\lambda||J_i >}{\sqrt{2J_i+1}} = \frac{Ze\beta}{\sqrt{2J_i+1}} \int F_\lambda(\vec{r}) r^{\lambda+2}\, \mathrm{d}r \tag{71}$$

For a transition in the nucleus, the neutron part may be different from the proton part. Therefore, we define the neutron and proton multipole matrix elements as below:

$$M_p(E\lambda) = \frac{Ze\beta_p}{\sqrt{2J_i+1}} \int F_\lambda^{(p)}(\vec{r}) r^{\lambda+2}\, \mathrm{d}r \tag{72}$$

and

$$M_n(N\lambda) = \frac{Ne\beta_n}{\sqrt{2J_i+1}} \int F_\lambda^{(n)}(\vec{r}) r^{\lambda+2}\, \mathrm{d}r\,, \tag{73}$$

$F_\lambda^{(p)}(r)$ and $F_\lambda^{(n)}(r)$ being the proton and neutron transition density, respectively.

The reduced transition probabilities B($E\uparrow$) and B($N\uparrow$) [Eq. (69) and (71)] are obtained from the relations,

$$B(E\lambda\uparrow) = |M_p|^2 \tag{74}$$

and

$$B(N\lambda\uparrow) = |M_n|^2\,. \tag{75}$$

The isoscalar and isovector transition rates are given by the usual expression:

$$B(\Delta T = 0) = |M_n + M_p|^2 \tag{76}$$

and

$$B(\Delta T = 1) = |M_n - M_p|^2 \ . \tag{77}$$

In Eq. (67), we have expressed the isoscalar and isovector sum rules for transitions of multipolarity $\lambda \geq 2$. If the proton and neutron transition densities are assumed to have same shape, then, the neutron and proton sum rules $S_n(N\lambda)$ and $S_p(E\lambda)$ are related to the isoscalar or isovector sum rule by factors of $\frac{N}{A}$ and $\frac{Z}{A}$, respectively. That is,

$$S_p(E\lambda) = \left[\frac{\hbar^2}{8\pi M_p}\right] Ze^2\lambda(2\lambda+1)^2 < r^{2\lambda-2} > \tag{78}$$

and

$$S_n(N\lambda) = \left[\frac{\hbar^2}{8\pi M_n}\right] Ne^2\lambda(2\lambda+1)^2 < r^{2\lambda-2} > \ . \tag{79}$$

From Eq. (68), we can obtain the expression for the fraction of the isoscalar, isovector, proton and neutron EWSR as below:

$$\text{Fraction(IS)} = \frac{E_x \cdot B(\Delta T = 0)}{S(\Delta T = 0, E\lambda)} = \frac{E_x |M_n + M_p|^2}{S(\Delta T = 0, E\lambda)} \tag{80}$$

$$\text{Fraction(IV)} = \frac{E_x \cdot B(\Delta T = 1)}{S(\Delta T = 1, E\lambda)} = \frac{E_x |M_n - M_p|^2}{S(\Delta T = 1, E\lambda)} \tag{81}$$

$$\text{Fraction(p)} = \frac{E_x \cdot B(E\lambda \uparrow)}{S_p(E\lambda)} = \frac{E_x |M_p|^2}{S_p(E\lambda)} \tag{82}$$

$$\text{Fraction(n)} = \frac{E_x \cdot B(N\lambda \uparrow)}{S_n(N\lambda)} = \frac{E_x |M_n|^2}{S_p(N\lambda)} \ . \tag{83}$$

In the hydrodynamical model, the collective excitation states of heavy nuclei are well described [Sa-83] with

$$E(\lambda) = \hbar \, (C_\lambda / B_\lambda)^{1/2}$$

$$M_p^2 = \hbar\left(\lambda+\frac{1}{2}\right)\frac{Z^2e^2}{(2J_i+1)}(B_\lambda C_\lambda)_p^{-1/2} \times \left|\int F_\lambda^{(p)} r^{\lambda+2}\mathrm{d}r\right|^2 , \quad (84)$$

and, similarly,

$$M_n^2 = \hbar\left(\lambda+\frac{1}{2}\right)\frac{N^2e^2}{(2J_i+1)}(B_\lambda C_\lambda)_n^{-1/2} \times \left|\int F_\lambda^{(n)} r^{\lambda+2}\mathrm{d}r\right|^2 , \quad (85)$$

where the parameter B_λ is related to the mass transport associated with the transition, and C_λ is related to the restoring force due to the effective surface transition. If we consider a small region of N and Z, then $B_\lambda C_\lambda$ and $F_\lambda(\vec{r})$ are expected to be constant for protons and neutrons. Thus, the hydrodynamical model predicts $\frac{M_n}{M_p} = \frac{N}{Z}$ from Eq. (84) and (85). In the following section we examine the value $\frac{M_n}{M_p}$ from our new suggestion, and present the various EWSR fractions along with previous results.

4.4.3 Analysis and Discussion

As already mentioned in section 4.3, Fig. 4–15 presents the angular distributions for the GQR and the normalized curve from the distorted wave impulse approximation calculations using the code NDWPI. The program employs the Klein-Gordon equation Eq. (47) with the non-local π–nucleus elastic scattering optical potential Eq. (65). The wave equation is solved with appropriate boundary conditions to generate pion distorted waves for the incident and exit channel. The boundary matching between the internal and external logarithmic derivatives is

made at a match point, which produces the phase shift. The pion-nucleon phase shifts were evaluated at an energy 28 MeV below the pion-nucleon center of mass energy following the Cottingame-Holtkamp description [Co-80]. A two parameter Fermi function, $\rho(r) = \rho_0 \frac{1}{1+e^{(r-c)/z}}$, was used for the neutron and proton ground state densities. Half density radius c = 6.51 fm and diffusivity z = 0.55 were used and $\langle r^2 \rangle^{1/2} = 5.43$ fm was produced. The transition density was obtained from the collective model. The Coulomb interaction was not included in solving the Klein-Gordon equation due to the unreliable results of NDWPI when the Coulomb potential is included. It is reported that around the energy T_π = 162 MeV, the effect of the Coulomb excitation on the peak of differential cross section is about 10 ~20% for the π^+ and 5 ~ 10% for the π^- in the ^{208}Pb(π,π') interaction [Oa-89]. The complex coefficients, $b^{\pm}_{p0}, b^{\pm}_{p1}, b^{\pm}_{n0}$ and $b^{\pm}_{n1}$, are tabulated below for each incoming and outgoing $\pi^{\pm}$.

	$b^+_{p0}(b^-_{n0})$	$b^+_{p1}(b^-_{n1})$
incident $\pi^+(\pi^-)$	$-1.765 \pm i0.336$	$9.067 \pm i0.899$
outgoing $\pi^+(\pi^-)$	$-1.922 \pm i0.341$	$10.061 \pm i7.630$
	$b^+_{n0}(b^-_{p0})$	$b^+_{n1}(b^-_{p1})$
incident $\pi^+(\pi^-)$	$0.526 \pm i0.312$	$2.595 \pm i3.007$
outgoing $\pi^+(\pi^-)$	$0.634 \pm i0.338$	$2.872 \pm i2.554$.

In order to extract $\frac{M_n}{M_p}$ (Eq. 54), the following relations are firstly used:

$$\sigma_{data}(\pi^+) = \beta_p^2 \sigma_{ND}^{+p}(\pi^+, \beta_n = 0, \beta_p = 1) + \beta_n^2 \sigma_{ND}^{+n}(\pi^+, \beta_n = 1, \beta_p = 0) \quad (86)$$

$$\sigma_{data}(\pi^-) = \beta_p^2 \sigma_{ND}^{-p}(\pi^-, \beta_n = 0, \beta_p = 1) + \beta_n^2 \sigma_{ND}^{-n}(\pi^-, \beta_n = 1, \beta_p = 0) \quad (87)$$

where ND stands for the NDWPI calculation. The values,

$$\sigma_{data}(\pi^+) = 1.390 \pm 0.139 \text{ mb/sr}$$

and

$$\sigma_{data}(\pi^-) = 3.782 \pm 0.567 \text{ mb/sr} ,$$

were obtained by normalizing the GQR-angular distribution peak values of π^+ and π^- (Fig. 4-15) from the NDWPI calculations to the data. The values of $\sigma_{ND}^{+p}, \sigma_{ND}^{+n}, \sigma_{ND}^{-p}$ and σ_{ND}^{-n} also resulted from the NDWPI by using the given input information as shown in each parenthesis. After solving Eq. (86) and Eq. (87) for β_p^2 and β_n^2, and using the relation,

$$|M_i|^2 = \beta_i^2 |M_i(\beta_i = 1, \beta_j = 0)|^2 \text{ with } i,j = p,n , \tag{88}$$

we obtained

$$\begin{aligned}
M_n &= (1.30 \pm 0.10)\times 10^2 \text{ e } fm^2 \\
M_p &= (6.12 \pm 0.52)\times 10^1 \text{ e } fm^2 \\
\mathcal{R} &= \frac{M_n}{M_p} = 2.12 \pm 0.24 \\
B(E2\uparrow) &= M_p^2 = (3.74 \pm 0.45)\times 10^3 \text{ e}^2 \ fm^4 \\
B(N2\uparrow) &= M_n^2 = (1.70 \pm 0.19)\times 10^4 \text{ e}^2 \ fm^4
\end{aligned}$$

while the previous analysis based on the coherent addition of the neutron and proton transition amplitudes as in Eq. (55) yields

$$\begin{aligned}
\mathcal{R} &= \frac{M_n}{M_p} = 3.8 \\
B(E2\uparrow) &= (1.01 \pm 0.60)\times 10^3 \text{ e}^2 \ fm^4 \\
B(N2\uparrow) &= (1.45 \pm 0.36)\times 10^4 \text{ e}^2 \ fm^4 .
\end{aligned}$$

The ratio of the neutron-to-proton transition amplitude $\mathcal{R} = 2.1$ from the current analysis is much closer to the value of $\mathcal{R}$ predicted by both the HD model, 1.54, or by the recent RPA calculation of Auerbach, Klein and Siciliano [Au-85], 1.6, than the result from the previous analysis, $\mathcal{R}$ =3.8. The difference between our result and the HD result may be attributed to the fact that we did not consider the Δ propagation effects, the Pauli blocking effects and the Coulomb interaction, which all may end up with approximately 20% correction. Considering these effects, our value R is in good agreement with the theoretical value.

The proton and neutron EWSR fractions were also evaluated using the Eq. (82) and (83). The results are:

$$\begin{aligned} \text{proton EWSR fraction} &= 20 \pm 2\% \\ \text{neutron EWSR fraction} &= 58 \pm 7\% , \end{aligned}$$

compared to the value of

$$\begin{aligned} \text{proton EWSR fraction} &= 5 \pm 3\% \\ \text{neutron EWSR fraction} &= 50 \pm 12\% , \end{aligned}$$

obtained from the previous analysis. Our analysis indicates that more neutrons are involved in the transition to the GQR of the heavy ^{208}Pb nucleus. However, the proton strength is not as weak as the previous analysis indicates. Our increased proton strength is consistent with many (e,e′) and (e,e′x) experiments where the proton strength is measured, although Kühner et al. [Kü-81] reported about 5% of the proton fraction in the ^{208}Pb(e,e′) experiment.

If the dominant decay mode in the GR region is direct decay there may not be an enough time to develope a good isospin state, and therefore, there may not be distinctive isoscalar or isovector states. If our assumption holds, the isoscalar and isovector fractions of the EWSR for the GR states may not be useful quantities, but for the purpose of the comparison with other probes, the values of our analysis are also presented here:

$$\text{isoscalar EWSR fraction} = 76 \pm 9\%$$

$$\text{isovector EWSR fraction} = 10 \pm 3\% .$$

These values are in good agreement with the results from ^{208}Pb(e,e') experiments [Bu-72, Pi-74, Si-75], and a recent measurements of the γ decay of the GQR in ^{208}Pb [Be-84]. Our values are also comparable to the values predicted from the RPA calculations done by Speth et al. [Ri-74], 51% of the isoscalar and 12% of the isovector EWSR.

As a conclusion, the current analysis based on our supposition in Eq. (54) seems to explain better the large π^-/π^+ cross section ratios observed in heavy nuclei with N > Z. The surprising feature of this observation is that it suggests a much different picture of the giant resonances than is currently accepted. Rather than a coherent oscillation of neutrons in phase with protons, it appears as an incoherent sum of a proton and a neutron oscillation.

Chapter 5. Summary

[1] $^{12}C(\pi^{\pm}, \pi^{\pm\prime}p)^{11}B$ Reaction

Measurements were made at $T_\pi = 180$ MeV and $\theta^{lab}_{scatt} = 20°$ with five BGO phoswich detectors, each at $-120°, -90°, -60°, 60°$ and $90°$ in the scattering plane, i.e., $\phi = 0°$.

For the giant dipole ($20 \leq E_x(^{12}C) \leq 30$ MeV) region with the $E_x(^{11}B) <$ 10 MeV gate, both the shape and magnitude of the angular distributions of the emitted protons from the $(\pi^+, \pi^{+\prime}p)$ reaction are relatively well described by the factorized DWIA single nucleon knock-out calculation. However, the $(\pi^-, \pi^{-\prime}p)$ data show much enhanced cross sections and no clear peak in the recoil direction, in contrast to the DWIA predictions. The overall ratio, $R = \frac{\sigma(\pi^+, \pi^{+\prime}p)}{(\pi^-, \pi^{-\prime}p)}$, was 1.6. Neither the DWIA calculations (r = 9), which assume a quasi-free knock-out process, nor the assumption that the reaction is dominated by states of good isospin near the GDR in ^{12}C (r = 1) can explain the observed ratio. This leads to the speculation that inelastic scattering to the GDR region in ^{12}C contains two components, one of which is direct (quasi-free), the other being semi-direct (resonance). The angular distribution of the decay proton indicates that the $(\pi^+, \pi^{+\prime}p)$ is dominated by the direct decay whereas, at least, the $(\pi^-, \pi^{-\prime}p)$ must have a strong contribution from the semi-direct process. A strong angle dependence of R is observed, and this is interpreted as as an interference between the amplitudes for these two processes. The interference sould be less important for $(\pi^+, \pi^{+\prime}p)$ because the direct amplitude is three times larger than for

$(\pi^-, \pi^{-\prime}\mathrm{p})$. Therefore, a semi-direct amplitude comparable to the quasi-free scattering amplitude will enhance the $(\pi^-, \pi^{-\prime}\mathrm{p})$ cross section while it has much less effect on the $(\pi^+, \pi^{+\prime}\mathrm{p})$ cross section. We conclude that the decay of the continuum in the region of the GR is largely governed by how it was excited, i.e., by π^+ or π^-. The absolute cross sections predicted by THREEDEE are quite sensitive to the choice of spectroscopic factors and optical model parameters [Jo-89], but the ratio R is quite insensitive to the distortions. We base our conclusion on the failure of simple DWIA knock-out calculations to reproduce R, independent of the absolute magnitude. We have made no attempt to include higher order effects in the π–nucleus scattering such as those which have been predicted to arise from the Δ-hole model [Ky-84].

For the $40 \leq E_x(^{12}\mathrm{C}) \lesssim 70$ MeV region with the $E_x(^{11}\mathrm{B}) > 10$ MeV gate, the $(\pi^+, \pi^{+\prime}\mathrm{p})$ and $(\pi^-, \pi^{-\prime}\mathrm{p})$ cross sections are about the same at all energies. The agreement between experiment and the DWIA prediction is poor for both π^+ and π^- scattering. The angular distribution of protons in this region also appears to peak near the recoil direction but the ratio R is near unity at all angles. The DWIA calculations for 1s-shell knock-out do not resemble these data at all. The near equality of the $(\pi^+, \pi^{+\prime}\mathrm{p})$ and $(\pi^-, \pi^{-\prime}\mathrm{p})$ cross sections suggests that protons and neutrons are equally involved in the reaction. However, we do not believe that, for $E_x(^{12}\mathrm{C}) \gtrsim 40$ MeV, states of good isospin would play a major role except for possible double resonance [Mo-88b]. It is also possible that direct two, three, and four nucleon removals are important here. The failure of the one nucleon knock-out calculations with THREEDEE to reproduce the magnitude

and the near equality of the π^+ and π^- data suggests the importance of one of these process for $(\pi, \pi' \mathrm{p})$.

[2] ^{208}Pb$(\pi^{\pm}, \pi^{\pm\prime}\mathrm{n})$ Reaction and Extraction of $\frac{M_n}{M_p}$

We measured the angular distributions for ^{208}Pb$(\pi^{\pm}, \pi^{\pm\prime}\mathrm{n})$ reaction near the GR region with the same experimental condition as the ^{12}C. Here the angular distributions induced by π^+ and π^- are also different from each other. This is interpreted as a different excitation mechanism between incoming π^--nucleus (exciting neutron-neutron hole directly and decay via escape width $\Gamma^{\uparrow}$) and π^+-nucleus interaction (coupling to resonant states and decay through spreading width $\Gamma^{\downarrow}$ with possible inclusion of $\Gamma^{\uparrow\downarrow}$) in the GR region of ^{208}Pb. The interpretation led us to suggest that the ratio of cross sections for inelastic scattering to the GR region may have to be written in terms of an incoherent, instead of coherent, sum of amplitudes to neutron and proton particle-hole doorway states, since different final states of the residual nucleus are populated in these two processes. A reanalysis of the previous inelastic scattering data, assuming an incoherent addition of neutron and proton amplitudes gives $\mathcal{R} = \frac{M_n}{M_p} = 2.12$ compared to 3.8 from the previous analysis. This new value is in better agreement with the expectation based on the HD or RPA model, which suggests the giant resonance as an incoherent oscillation of a proton and a neutron rather than a coherent one.

[3] Future Direction

We concluded that, in the GR region of ^{12}C, ^{208}Pb, and ^{4}He [Jo-89], the angular distributions of $(\pi^+, \pi^{+\prime}\mathrm{N})$ are quite different from those of $(\pi^-, \pi^{-\prime}\mathrm{N})$. We inter-

preted these results as a different excitation mechanism between π^+–nucleus and π^-–nucleus scattering in the giant resonance region. For further study of pion coincidence experiments that could help in developing a theory of the nuclear continuum, the future studies can include $(\pi^{\pm}, \pi^{\pm\prime}\mathrm{p})$ near $\Delta_{3,3}$ and above $\Delta_{3,3}$, region for light nuclei, and $(\pi^{\pm}, \pi^{\pm\prime}\mathrm{n})$ for heavy nuclei.

Near $\Delta_{3,3}$ region measurements on light nuclei should be made in an attempt to separate reaction dynamics from nuclear structure. The dramatic differences in the ratio R of the $^{12}\mathrm{C}(\pi^{\pm}, \pi^{\pm\prime}\mathrm{p})$ in this dissertation and the earlier $^{4}\mathrm{He}(\pi^{\pm}, \pi^{\pm\prime}\mathrm{p})$ data [Jo-89] may be due to differences in the structure of the continuum, since quasi-free scattering should be relatively independent of the atomic number A [La-88]. For this purpose, we should select a group of very light nuclei such as $^{2}\mathrm{D}$ and $^{3}\mathrm{He}$ in which the quasi-free process should dominate because of the absence of giant resonances in these nuclei. Another group must come from the nuclei near $^{12}\mathrm{C}$ such as $^{16}\mathrm{O}$ and $^{18}\mathrm{O}$ targets where the continuum is dominated by giant resonances, one with N = Z and one with N > Z. Also in order to provide more information on decay process, more angles should be covered in both angles (θ, ϕ).

We must also extend the examination of this different reaction mechanism between π^+ and π^- to energies above $\Delta_{3,3}$ resonance. At these energies, distortion effects of the incident pion waves due to $\Delta_{3,3}$ resonance will be reduced as Fig. 1–1 displays the relatively flat and much smaller π–N total cross sections in the 300 – 500 MeV region. Another noticeable phenomenon in this region is that the ratio of $\sigma(\pi^+)/\sigma(\pi^-)$ gradually reduces, becomes unity, and is inverted to 1:2 in

the region around 550 MeV where isospin $\frac{1}{2}$ resonance becomes important. Along with the reduced distortion effects, the inversion of the ratio and the dominance of (T = 1/2) resonance are a strong incentive to pursue the $(\pi^{\pm}, \pi^{\pm\prime}\mathrm{p})$ coincidence measurements at these higher energies.

Finally, if we develop a more sophiscated method for neutron detection with the BGO phoswich detector covering more angles (θ, ϕ), then the $(\pi^{\pm}, \pi^{\pm\prime}\mathrm{n})$ reactions on heavy nuclei will also provide useful information for the study of the nuclear continuum.

Appendix I.

A. Chamber Calibration Procedure [Bo-88a]

1. Experimental Parameter Setup:
   This can be done by quasi-elastic scattering and illuminating whole chambers uniformly.

2. Timing Checks:
   Delay-line times should be within TDC limit.

3. Drift Time Checks:
   Center time distributions should be in channel = 17.0

4. Drift Position Calibration:
   This produces lookup table of drift time (channel number vs. position).

5. Delay-line Calibration:
   This produces 3rd order polynomial expansion of time vs. position and adjusts offsets to center calculated positions and angles.

6. Offset Plane Adjustments:
   This adjusts offsets after truncation to split spacing of adjoining planes.

7. Left-Right Ambiguity Adjustment:
   This sets software switches for adding (subtracting) drift times.

B. Polynomial Optimization [Bo-88b]

Systems of magnets at EPICS may be viewed as the box in Fig. I–1, where the position, x_2, can be expressed as

$$\begin{aligned} x_2 &= \mathrm{F}(x_1, \theta_1, y_1, \phi_1, \delta) \\ &= \left(\frac{dx_2}{dx_1}\right) x_1 + \left(\frac{dx_2}{d\theta_1}\right) \theta_1 + \left(\frac{dx_2}{\delta}\right) \delta + \\ &\quad \left(\frac{d^2x_2}{dx_1^2}\right) x_1^2 + \left(\frac{d^2x_2}{dx_1 d\theta_1}\right) x_1\theta_1 + \left(\frac{d^2x_2}{d\theta_1^2}\right) \theta_1^2 + \\ &\quad \left(\frac{d^2x_2}{dx_1 d\delta}\right) x_1\delta + \left(\frac{d^2x_2}{d\theta_1 d\delta}\right) \theta_1\delta + \left(\frac{d^2x_2}{d\delta^2}\right) \delta^2 + \end{aligned}$$

$$\left(\frac{d^2x_2}{dy_1^2}\right) y_1^2 + \left(\frac{d^2x_2}{dy_1 d\phi_1}\right) y_1\phi_1 + \left(\frac{d^2x_2}{d\phi_1^2}\right) \phi_1^2$$
$$+ \quad \text{Higher Order Terms .}$$

Optimized quantities are $(x, \theta, y, \phi)_{tgt}$, $\delta = \frac{\Delta P}{P}$, $(\theta, \phi)_{check}$ and TOF. Table I–1 shows the calibrated quantities with the relationships between their units and channel numbers.

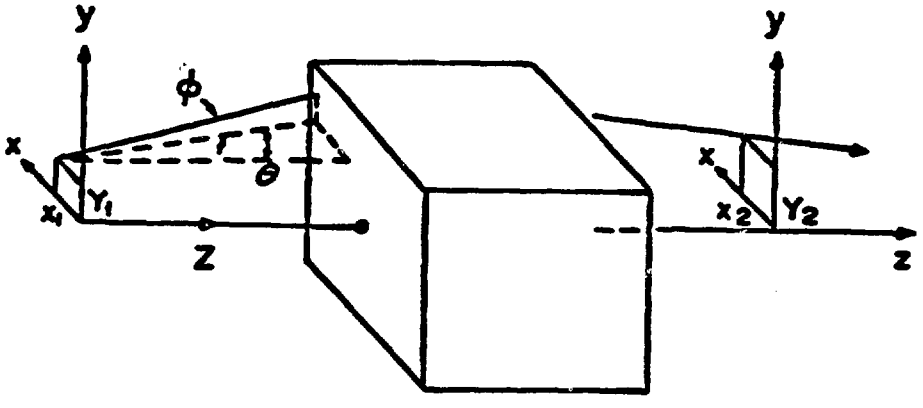

Fig. I–1 Input and output coordinates.

The following is the procedure of polynomial optimization called "Ray Writing".

1. Set experimental parameters such as magnet settings (elastic, quasi-elastic $\cdots$) and selecting position of rod target.
2. Maximize background rejection such as muon rejection.
3. For each "Good Events" write "Ray" to disk file that includes measured and calculated quantities $x, \theta, y, \phi, \delta, \cdots$.
4. Vary magnet parameters.
5. Again write "Rays" to disk file.
6. Append ray files so that system is overdetermined.
7. Solve linear least square problem.

The effect of optimization can be seen by comparing the two pictures Fig. I–2. Fig. I–2(a) displays the XTGT histogram obtained from assuming $X_{tgt} = -1.0x_f$, whereas Fig. I–2(b) is obtained after the optimization of the coefficients in

$$X_{tgt} = \sum_{n=1}^{N_{coeff}} \mathrm{a}_n x_n \ . \tag{1}$$

These optimized coefficients are stored in a file called POL.DAT (Table I–1).

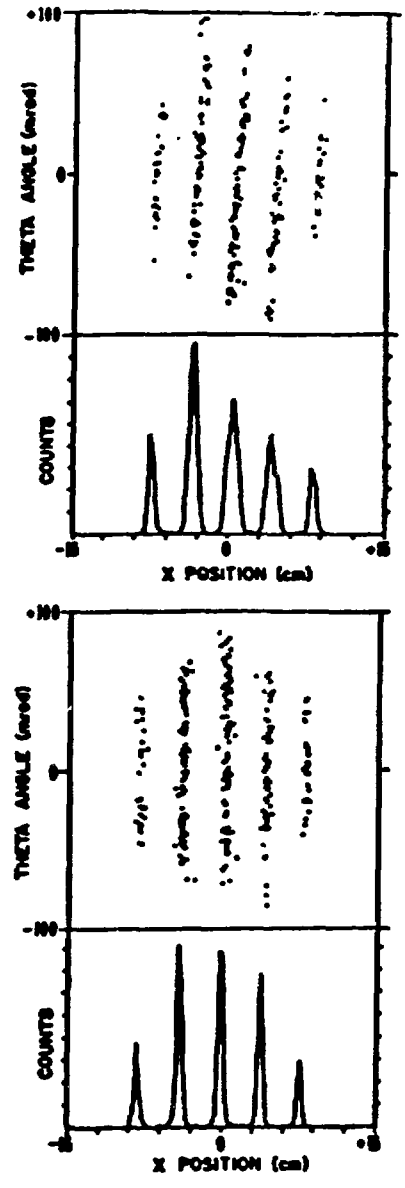

Fig. I–2 (a): X-target histograms with $X_{tgt} = -1.0x_f$ and

(b): $X_{tgt} = \sum_{n=1}^{N_{coeff}} a_n x_n$.

Table I–1: Sample POL.DAT file used in this experiment.

233,	18,	X	Target	Quasi Elastic	
0,	0,	0,	0,	0.584757E+00,	
221,	0,	0,	0,	−0.982240E+00,	x_f
222,	0,	0,	0,	−0.391352E-03,	θ_f
221,	243,	0,	0,	−0.268082E-02,	$x_f\delta$
222,	243,	0,	0,	−0.315390E-02,	$\theta_f\delta$
222,	223,	0,	0,	0.688819E-04,	$\theta_f y_f$
222,	224,	0,	0,	0.246027E-04,	$\theta_f\phi_f$
221,	243,	243,	0,	0.308315E-03,	$x_f\delta^2$
222,	243,	243,	0,	−0.546073E-04,	$\theta_f\delta^2$
221,	223,	223,	0,	−0.143031E-03,	$x_f y_f^2$
221,	223,	224,	0,	0.514629E-04,	$x_f y_f\phi_f$
221,	224,	224,	0,	−0.147752E-04,	$x_f\phi_f^2$
221,	221,	221,	0,	−0.736998E-04,	x_f^3
221,	221,	222,	0,	0.714513E-04,	$x_f^2\theta_f$
222,	222,	222,	0,	0.464615E-06,	θ_f^3
222,	223,	223,	0,	0.353595E-03,	$\theta_f y_f^2$
222,	223,	224,	0,	−0.125571E-03,	$\theta_f y_f\phi_f$
222,	224,	224,	0,	0.117272E-04,	$\theta_f\phi_f^2$

Appendix II.

Table II–1: Portion of the Sample .HST file used in this experiment.

```
Xtgt/xp:233:-1500:1500:5/TE:91
Thttgt/xp:234:-2000:2000:10/TE:91
Ytgt/xp:235:-1000:1000:10/TE:91
Phitgt/xp:236:-1000:1000:10/TE:91
Thtchk/xp:237:-500:500:20/TE:92
Phichk/xp:238:-500:500:20/TE:92
;
MM/TE:93/XP:246:-500:5000:10
MMskip/XP:246:-500:5000:2/TE:111
MMkeep/XP:246:-500:5000:2/TE:112
MMFC /XP:246:-500:5000:2/TE:113
FC /XP:84:-3000:3000:20/TE:0/BL:1
```

Table II–2: Portion of the Sample .TST file used in this experiment.

```
; Left right tests
2,IGATE,11    ;2    ;C1XL-R
3,IGATE,12    ;3    ;C2XL-R
;Fast Clear
14,GAT,3,2,32001    ;14    ;fast clear (1/10)
;PID
15,IBOX,1,    ;15    ;BOX 1 ==> PID
16,IOR,1,-1,    ;16    ;Loop1 counter
;
BLOCK,2,
90,AND,39,46,65,66,67,68,
;
101,GATE,86,330,355        ;time bgo1
102,GATE,87,324,349        ;time bgo2
103,GATE,88,324,349        ;time bgo3
104,GATE,89,330,355        ;time bgo4
105,GATE,90,313,338        ;time bgo5
```

Appendix III.

Table III–1 The ratio $R_p = \sigma(\pi^+, \pi^+ p)/\sigma(\pi^-, \pi^- p)$ for $40 \leq E_x(^{12}C) \leq 70$ MeV, at $T_\pi = 180$ MeV and $\theta_{lab} = 20°$. Data were obtained with the $E_x(^{11}B) \geq 10$ MeV gate.

θ_{pCM}	R(DWIA)	R(Experiment)
−77.0°	7.3	1.5 ± 0.3
−46.4°	5.8	0.8 ± 0.1
−15.4°	4.2	1.0 ± 0.2
107.2°	2.4	1.1 ± 0.3
136.6°	3.5	1.2 ± 0.4
R of summed σ	6.1	1.0 ± 0.1

Table III–2 The ratio $R_n = \sigma(\pi^-, \pi^- n)/\sigma(\pi^+, \pi^+ n)$ for $16 \leq E_x(^{208}Pb) \leq 40$ MeV, at $T_\pi = 180$ MeV and $\theta_{lab} = 20°$.

θ_{nCM}	R(DWIA)	R(Experiment)
−58.3°	8.1	2.5 ± 0.8
−28.3°	6.7	3.2 ± 1.3
1.8°	5.8	2.3 ± 1.0
121.9°	4.2	2.7 ± 1.3
151.9°	3.7	2.2 ± 1.4
R of summed σ	6.4	2.6 ± 0.5

Table III–3 The ratio $R_p = \sigma(\pi^+, \pi^+ p)/\sigma(\pi^-, \pi^- p)$ for $13 \leq E_x(^{208}Pb) \leq 33$ MeV, at $T_\pi = 180$ MeV and $\theta_{lab} = 20°$.

θ_{pCM}	R(DWIA)	R(Experiment)
−55.1°	9.9	1.4 ± 1.0
−25.0°	7.2	2.1 ± 1.2
5.1°	6.0	0.8 ± 0.3
125.2°	7.6	0.3 ± 0.5
155.1°	7.1	—
R of summed σ	7.0	1.1 ± 0.3

Table III–4 The ratio $R_n = \sigma(\pi^-, \pi^- n)/\sigma(\pi^+, \pi^+ n)$ for $8 \leq E_x(^{208}Pb) \leq 15$ MeV, at $T_\pi = 180$ MeV and $\theta_{lab} = 20°$.

θ_{nCM}	R(DWIA)	R(Experiment)
−47.6°	7.3	2.0 ± 0.8
−17.5°	7.2	4.0 ± 1.9
12.7°	6.7	3.3 ± 1.8
132.8°	3.9	0.9 ± 0.4
162.7°	3.6	4.0 ± 2.3
R of summed σ	6.4	2.2 ± 0.4

References

[Am-79] J. F. Amann, R. L. Boudrie; H. A. Thiessen, C. L. Morris, and L. E. Smith, IEEE Transactions in Nuclear Science NS-26, 4389 (1979).

[Am-64] U. Amaldi, Jr., et al., Phys. Rev. Lett. 13 341 (1964).

[At-81] L. G. Atencio, J. F. Amann, R. L. Boudrie, C. L. Morris, Nucl. Inst. Meth. 187, 381 (1981).

[Au-67] E. H. Auerbach, D. M. Fleming, and M. M. Sternheim, Phys. Rev. 162, 1683 (1967).

[Au-85] N. Auerbach, A. Klein, and E. R. Siciliano, Phys. Rev. C31 682 (1985).

[Ba-68] P. Bareyre, C. Bricman, and G. Villet, Phys. Rev., 165, 1730 (1968).

[Be-76] F. E. Bertrand, Ann. Rev. Nucl. Sci. 26 457 (1976).

[Bl-84] L. C. Bland, Ph.D Dissertation, University of Pennsylvania (1984); Los Alamos Report LA-9960-T (1984).

[Bo-69] A. Bohr and B. R. Mottelson, "Nuclear Structure", Vol. 1, W. A. Benjamin, inc. (1969).

[Bo-75] A. Bohr and B. R. Mottelson, "Nuclear Structure", Vol. 2, W. A. Benjamin, inc. (1975).

[Bo-79] R. L. Boudrie, J. F. Amann, C. L. Morris, H. A. Thiessen and L. E. Smith, IEEE Trans. Nucl. Sci. NS-26, 4588 (1979).

[Bo-88] G. O. Bolme, et al., Phys. Rev. Lett. 61, 1081 (1988).

[Br-64] G. E. Brown, Nucl. Phys. 57 339 (1964).

[Br-77] P. J. Brussard and P. W. M. Glaudemans, "Shell-Model Applications in Nuclear Spectroscopy", (North-Holland, New York, 1977).

[Bu-86] G. R. Burleson at al., Nuc. Instr. Meth. A247, 327 (1986).

[Ch-77] N. S. Chant and P. G. Roos, Phys. Rev. C15, 57 (1977).

[Ch-79] C. C. Chang, Giant Multipole Resonances, ed. F. E. Bertrand, (Harwood-Academic, Chur, Switzerland, 1979), p. 191.

[Ch-82a] N. S. Chant, L. Rees, and P. G. Roos, Phys. Rev. Lett. 48, 1784 (1982).

[Ch-82b] N. S. Chant, code "THREEDEE", unpublished, and L. Rees, N. S. Chant, and P. G. Roos, Phys. Rev. C26, 1580 (1982).

[Cl-65] C. F. Clement, A. M. Lane, and J. A. Rook, Nucl. Phys. 66, 273 (1965).

[Co-67] S. Cohen and D. Kurath, Nucl. Phys. A101, 1 (1967).

[Co-80] W. B. Cottingame and D. B. Holtkamp, Phys. Rev. Lett., 45 1828 (1980).

[Co-87] W. B. Cottinggame et al., Phys. Rev. C36, 230 (1987).

[Di-82] S. A. Dickey, J. J. Kraushaar and M. A. Rumore, Nucl. Phys. A391, 413 (1982).

[Di-86] H. Dias, N. Teruya, and E. Wolynec, Phys. Rev. C33 1955 (1986).

[Ei-75] J. M. Eisenberg and W. Greiner, "Nuclear Theory", Vol. 1, North-Holland Publishing Company. (1975).

[Ei-76a] J. M. Eisenberg and W. Greiner, "Nuclear Theory", Vol. 2, North-Holland Publishing Company. (1976).

[Ei-76b] R. A. Eisenstein and G. A. Miller, Comp. Phys. Comm. 11, 95 (1976).

[Ei-80] J. Eisenberg and D. Koltun, "Theory of Meson Interactions with Nuclei", (John Wiley and Sons, New York, 1980).

[El-67] L. R. B. Elton and A. Swift, Nucl. Phys. A94, 52 (1967).

[Ey-84] W. Eyrich et al., Phys. Rev. C29 418 (1984).

[Fe-67] H. Feshbach, A. K. Kerman, and R. H. Lemmer, Ann. Rev. of Phys. 41 230 (1967).

[Fr-74] H. Frauenfelder and E. M. Henley, "Subatomic Physics", Prentice-Hall, Inc., (1974).

[Fr-87] B. Frois and C. N. Papanicolas, Ann. Rev. Nucl. and Part. Sci., 37, 133 (1987).

[Gr-87] P. Grabmayr, et al., Nucl. Phys. A469 285 (1987).

[Go-64] M. L. Goldberger and K. M. Watson, "Collision Theory", Wiley, New York, (1964).

[Ha-79] S. S. Hanna, in Giant Multipole Resonances, edited by F. E. Bertrand (Harwood-Academic, Chur, Switzerland, 1979), pp. 1.

[Ha] Harshaw/Filtrol Report, "BGO", unpublished.

[Hu-73] E. V. Hungerford, Nucl. Instr. Meth. 111, 509 (1973).

[Hu-87] J. R. Hurd et al., Nucl. Phys. A462, 605 (1987).

[Ja-74] C. W. de Jager, H. de Vries, and C. de Vries, Atom. Dat. Nucl. Dat. Tab., 14, 479 (1974).

[Jo-89] M. K. Jones, Ph.D Dissertation, University of Minnesota (1989).

[Ki-55] L. S. Kisslinger, Phys. Rev. 98, 761 (1955).

[Kn-88] Karl-Tasso Knöpfle, Giant Resonances—Excitation and Decay—Comparison of Electromagnetic and Hadronic Probes, ed. O. P. Sushkov, (World Scientific Publishing Co. Singapore, 1988), p. 595.

[Ko-86] J. H. Koch, in New Vistas in Nuclear Dynamics, ed. P. J. Brussard and J. H. Koch, Plenum Press, p. 191 (1986).

[Kü-81] G. Kühner et al., Phys. Lett. 104B, 189 (1981).

[Ky-84] G. S. Kyle, Phys. Rev. Lett. 52 974 (1984).

[La-80] "LAMPF Users Handbook", Los Alamos Scientific Laboratory Report MP-DO-1-UHB, (1980).

[La-87] "lampf", Los Alamos Scientific Laboratory Report LA-UR-87-327, (1987).

[La-88] LAMPF Research Proposal No. 1105 (1988), unpublished.

[Lo-70] W. O. Lock and D. F. Measday, "Intermediate Energy Nuclear Physics", Barnes and Noble, (1970).

[Lo-86] R. W. Lourie et al., Phys. Rev. Lett. 56, 2364 (1986).

[Lu-65] A. A. Lushnikov and D. F. Zaretsky, Nucl. Phys. 66 35 (1965).

[Me-62] Messiah, QM (1962).

[Mi-75] D. J. Millener and D. Kurath, Nucl. Phys. A255, 315 (1975).

[Mo] C. L. Morris, Program Newfit.

[Mo-78] C. Morris, H. Thiessen, and G. Hoffmann, IEEE Trans. Nucl. Sci., Vol. NS-25, 141 (1978).

[Mo-82] C. Morris, Nucl. Instr. Meth., 196 263 (1982).

[Mo-85] C. L. Morris et al., Nucl. Inst. Meth., A238, 94 (1985).

[Mo-88a] C. L. Morris, (private communication).

[Mo-88b] S. Mordechai et al., Phys. Rev. Lett. 61, 531 (1988).

[Mo-89] C. L. Morris, private communication.

[Na-81] A. Nadasen et al., Phys. Rev. C23, 1023 (1981).

[Nu-87] Nuclear Data Sheets, 47 (1986).

[Oa-89] D. S. Oakley et al., preprint.

[Ok-82] K. Okada et al., Phys. Rev. Lett. 48 1382 (1982).

[Pi-81] E. Piasetzky et al., Phys. Rev. Lett. C46, 1271 (1981).

[Pi-82] E. Piasetzky et al., Phys. Rev. C25, 2687 (1982).

[Pl-86] M. Plum, LAMPF Toutorial (1986), unpublished.

[Pr-75] M. A. Preston and R. K. Bhaduri, "Structure of the Nucleus", Addison-Wesley Publishing Company, Inc., (1975).

[Re-82] L. Rees, N. S. Chant, and P. G. Roos, Phys. Rev. C26, 1580 (1982).

[Ri-74] P. Ring and J. Speth, Nucl. Phys. A235, 315 (1974).

[Ro-65] L. D. Roper, R. M. Wright, and B. T. Feld, Phys. Rev., 138B, 190 (1965).

[Ro-78] G. Rowe, M. Salomon, and R. H. Landau, Phys. Rev. C18, 584 (1978).

[Sa-80] G. R. Satchler, Introduction to Nuclear Reactions, (Halsted Press, NY, 1980).

[Sa-83] A. Saha et al., Phys. Lett. 132B, 51 (1983).

[Se-77] Emilio Segrè, Nuclei and Particles, (W. A. Benjamin, Inc. Reading, Massachusetts, 1977).

[Se-81] S. J. Seestrom-Morris, Ph.D Dissertation, University of Minnesota (1981); Los Alamos National Laboratory, Report No. LA-8916-T.

[Se-85] P. A. Seidl, Ph.D Dissertation, The University of Texas at Austin (1984); Los Alamos National Laboratory Report No. LA-10338-T (1985).

[Se-86] S. J. Seestrom-Morris et al., Phys. Rev. C33 1847 (1986).

[Si-70] I. Sick and J. S. McCarthy, Nucl. Phys. A150, 631 (1970).

[Th-70] H. A. Thiessen and S. Sobottka,Los Alamos National Laboratory Report No. LA-4534-MS (1970).

[Th-77] H. A. Thiessen et al., Los Alamos National Laboratory Report No. LA-6663-MS (1977).

[Tr-88] B. True, private communication.

[Üb-79] H. Überall, "Electron Scattering from Complex Nuclei" (Academic, New York, 1979), Vol. B, pp. 729.

[Ye-88] Y. F. Yen, Private Communication.

[Zi-79] H. J. Ziock et al., Phys. Rev. Lett. 43 1919 (1979).

[Zi-81] H. J. Ziock et al., Phys. Rev. C24, 2674 (1981).

*U.S. GOVERNMENT PRINTING OFFICE: 1990-0-773-034/20033